

# Scanning Tunneling Microscopy and Spectroscopy of Functional Molecules on Metal Surfaces

Dissertation  
zur Erlangung des Doktorgrades  
der Mathematisch-Naturwissenschaftlichen Fakultät  
der Christian-Albrechts-Universität  
zu Kiel

vorgelegt von  
Xin Ge  
Kiel  
2006

Referent: Prof. Dr. Richard Berndt

Korreferent: Prof. Dr. Lutz Kipp

Tag der mündlichen Prüfung:

Zum Druck genehmigt: Kiel

# Abstract

This thesis is committed to the study of functional molecules adsorbed on metal surfaces by means of Low Temperature Scanning Tunneling Microscopy. It includes two main parts.

In the first part the adsorption geometry of lander molecule ( $C_{90}H_{98}$ ) on different metal surfaces is discussed. Three conformations as well as chiral structures of lander molecules on the terrace of Cu(100) are observed by STM. Electron scattering quantum chemical calculated results are compared with our experimental data. Lander molecules adsorb at the step edge of Cu(100) with its conducting board parallel to the step, thus preventing good electronic contact between the molecule and the step. The same geometry is found for lander molecules adsorbed at the step of  $Cu_3Au(100)$  although this substrate yields steps whose height perfectly matches the molecular wire height on terraces. Lander molecules assemble into molecular wires about 10~50 nm long on Cu(111) at low coverage. Lander molecules adsorbed at step of Au(788) with specific sites are observed by STM.

A further study concentrates on scanning tunneling spectroscopy of lander adsorbed on different substrates. A shift to higher energy for lander empty state peaks on  $Cu_3Au(100)$ , Ag(111), Cu(111) and Au(111) has been found and is due to the fact of work function differences between these substrates. Wider HOMO (highest occupied molecular orbital)-LUMO (lowest unoccupied molecular orbital) gaps in the spectra of lander molecule on noble (111) substrates compared with  $Cu_3Au(100)$  are also observed in the spectra data. This is explained as the result of increasing charging energy due to the screening behavior for lander on noble (111) substrates.

The second part contains the investigation of Cobalt Phthalocyanine molecule

on Cu(111). Coverage dependent supramolecular structures of adsorbed CoPc on Cu(111) has been found by STM. It is due to the delicate balance between local molecule-molecule interaction and molecule-substrate interaction.  $\alpha(\times)$ -type stacking of CoPc is determined with the help of submolecularly resolved STM images. Evident adsorption-site-dependent STM images of individual CoPc molecule on CoPc monolayer have been found. This could be explained as to the electronic coupling change between the molecule and substrate. And experimentally measured scanning tunneling spectroscopy results of CoPc on Cu(111) are assigned to the molecular orbitals of CoPc.

# Contents

Abbreviations and Common Symbols	v
<b>1 Introduction</b>	<b>1</b>
<b>2 Theory</b>	<b>5</b>
2.1 The Tunneling Current . . . . .	5
2.2 Topographic Imaging by STM . . . . .	9
2.3 Scanning Tunneling Spectroscopy . . . . .	11
2.3.1 $dI/dV$ spectroscopy . . . . .	11
2.3.2 Surface states . . . . .	12
2.3.3 $I(z)$ curve . . . . .	15
2.3.4 $dI/dV$ map . . . . .	16
2.3.5 Molecular adsorbates spectroscopy . . . . .	16
<b>3 Experimental Setup</b>	<b>21</b>
3.1 Overview . . . . .	21
3.1.1 Preparation chamber . . . . .	23
3.1.2 STM chamber . . . . .	23
3.2 Modification of the Heating Stage . . . . .	24
3.3 Sample Preparation . . . . .	26
3.3.1 Preparation of atomically clean substrates . . . . .	26
3.3.2 Molecule deposition . . . . .	26

<b>4</b>	<b>A Molecular Wire on Metal Surfaces</b>	<b>29</b>
4.1	Lander on Cu(100) . . . . .	32
4.1.1	Conformations of lander on Cu(100) . . . . .	32
4.1.2	Chiral structures of lander on Cu(100) . . . . .	38
4.1.3	Lander on films of NaCl on Cu(100) . . . . .	44
4.2	Lander on Other Substrates . . . . .	45
4.2.1	Lander on Cu <sub>3</sub> Au(100) . . . . .	45
4.2.2	Lander on Cu(111) . . . . .	48
4.2.3	Lander on Au(788) . . . . .	50
4.3	STS of Lander on Different Metal Substrates . . . . .	52
4.3.1	STS of lander on Cu <sub>3</sub> Au(100) . . . . .	53
4.3.2	Comparison of lander STS on different metal surfaces . . . . .	54
<b>5</b>	<b>Cobalt Phthalocyanine on Cu(111)</b>	<b>59</b>
5.1	Coverage Dependent Supramolecular Structures of CoPc . . . . .	62
5.1.1	Low coverage . . . . .	62
5.1.2	High coverage . . . . .	64
5.1.3	Coverage > 1 ML . . . . .	68
5.2	Stacking Pattern of CoPc . . . . .	69
5.3	Adsorption-site Dependent STM Images . . . . .	72
5.4	STS of CoPc on Cu(111) . . . . .	77
<b>6</b>	<b>Conclusion</b>	<b>81</b>
	<b>Bibliography</b>	<b>83</b>
	<b>Acknowledgments</b>	<b>95</b>
	<b>Curriculum Vitae</b>	<b>97</b>

# Abbreviations and Common Symbols

AFM	Atomic Force Microscopy
CCI	Constant Current Imaging
CHI	Constant Height Imaging
DFT	Density Functional Treatment
ESQC	Electron Scattering Quantum Chemical
FWHM	Full Width Half Maximum
fcc	face centered cubic
hcp	hexagonal close packed
LEED	Low Energy Electron Diffraction
IETS	Inelastic Electronic Tunneling Spectroscopy
HOMO	Highest Occupied Molecular Orbital
LUMO	Lowest Unoccupied Molecular Orbital
LDOS	Local Density of States
LTSTM	Low Temperature Scanning Tunneling Microscopy
ML	Monolayer
MO	Molecular Orbital
PES	Photo-electron Spectroscopy
SCF	Self-consistent Field
STM	Scanning Tunneling Microscopy
STS	Scanning Tunneling Spectroscopy
UHV	Ultra High Vacuum





# Chapter 1

## Introduction

One of the principal driving forces behind the information technology has been miniaturization, motivated by a large device density per chip and high operational speeds. In 1965, G. E. Moore predicted that every three years device size would reduce by 33% [1]. This prediction has been fulfilled so far. State-of-art transistors in industry are currently at the 90 nm node, while transistors with gate length of 50 nm [2] have been demonstrated.

However, modern computer technology, which relies on silicon-based chips, is rapidly approaching the limits of its physical capabilities (tens of nanometers). Quantum tunneling, gate oxide reliability, and excessive power dissipation, among other factors, start hampering the performance of such devices. Some of these issues can be handled by improving device design, packaging, processing, and channel mobilities in principal, but this will lead to an increase in fabrication cost [3]. “*There is plenty of room at the bottom*” as R. P. Feynman stated in a famous talk to the American Physical Society in 1959 [4], to proceed towards further miniaturization, science and technology will have to explore entirely new paradigms, such as architecture and new channel materials.

One promising strategy towards technology on the nanometer scale is replacing the “top-down” lithographic approach with a “bottom-up” synthetic chemical approach of assembling nanostructures and circuits directly from their molecular constituents.

Molecules are naturally small, stable, and their abilities of selective recognition

and binding can lead to cheap fabrication using self-assembly. Remarkable progress in this field has been made in the last few years, as researchers have developed ways of growing, addressing, and measuring small groups of molecules on metal and semi-conducting surfaces. Several prototype devices such as conducting wires, insulating linkages, rectifiers, switches, and transistors have been demonstrated [5]. Thus, the knowledge of the electronic and geometric structure of adsorbed molecules is important in surface science and related fields.

In the last 20 years, the most exciting technique related with nanotechnology may be the invention of Scanning Tunneling Microscope (STM) by G. Binnig, H. Rohrer, C. Gerber and E. Weibel [6,7]. The power of STM lies in its ability to spatially observe the electronic states with atomic resolution and energetically observe the electronic states which lie within a few electron-volts on either side of the Fermi level with an energy resolution of a few  $k_B T$ . The development of STM with other scanning technique like Atomic Force Microscope (AFM) has been crucial to the rapid progress in the understanding and engineering of nanosized structures. This new powerful technique has become an increasingly valuable tool for studying electron transport through molecules. The ability, using Scanning Tunneling Spectroscopy (STS) [8] with STM, opens the path to probe the local electronic structure of molecule. Inelastic Electronic Tunneling Spectroscopy (IETS) of single molecule [9] extends the possibility of chemical adsorbates identification.

Experiments involving the adsorption of molecules on substrates and analysis using an STM tip to probe these systems can be found in Refs. [10–16]. Although STM can provide the surface scientists with the highest resolution images of molecular adsorbates on a surface, the interpretation of STM images of molecules is not straight forward, since the internal structure of an STM image reflects the local electronic structure of the combined adsorbate-substrate system rather than the positions of atomic nuclei on a solid surface. The adsorption site and geometry also affect the STM image [17,18], since the electronic structure of the surface and adsorbate may mix depending upon the adsorption geometry.

To the first approximation, STM measures the electronic structure of the sample

---

near the Fermi level. When a finite potential bias is applied between the tip and substrate, the tip and substrate electrochemical potentials separate and the molecular orbitals located in the window of energy between the two electrochemical potentials, mediating electron flow between the tip and substrate. In this way, current-voltage characteristics may give clues of the electronic structure of the molecule.

Since a molecule may interact strongly with the tip and substrate, one should not think of the molecule as being isolated part of the system. In a more complete analysis, interference of tunneling through different tunneling channels must be considered. Electron flow depends on the details of the tip and molecule-substrate coupling [19–22]. In experiments on planar or near-planar molecules [23–27], sub-molecularly/atomically resolved STM images show how current flow through a molecule is dependent the lateral position of the STM tip above the molecule and the details of molecule-substrate configuration.

In this thesis, the adsorption of a functional molecular wire [“lander” molecule ( $C_{90}H_{98}$ )] and Cobalt-Phthalocyanine (CoPc) molecule served as molecular docking units for further molecular switch on different metal substrates are investigated by low temperature scanning tunneling microscopy (LTSTM) operated at 4.7 K (liquid Helium) in ultra high vacuum (UHV).

The thesis is organized as follows:

An introduction to the theory of scanning tunneling microscopy and spectroscopy is presented in chapter 2.

Chapter 3 will describe the experimental setup of the low temperature STM system and procedures of sample preparation. As part of the work in this thesis, a new designed heating stage will also be described.

In chapter 4, the adsorption of lander molecule on different metal substrates will be discussed in particular the conformations of lander and chiral structures of lander on Cu(100) and Cu(111). Calculated STM image will be compared to the data of measured topography of lander molecule and the STS results on lander on different metal surfaces for getting the electronic structure of the molecule will be presented.

STM studies of the adsorption geometry and electronic structure of CoPc on

Cu(111) are reported in chapter 5. Different adsorption phases of CoPc on Cu(111) with a range of coverages from submonolayers to more than 1 monolayer (ML) are found. Calculated molecular orbital images are compared with measured data of isolated CoPc molecules on CoPc monolayer. Highly resolved STM images of double layers CoPc reveals the stacking pattern of CoPc on Cu(111). With manipulation technique, we find a remarkable change of images for the molecules on different adsorption sites. On the hollow site, the molecule of the second layer shows finer submolecular structure than that on the top site. Experimentally measured STS data of CoPc on Cu(111) will be related to molecular orbitals (MOs) of CoPc.

Finally a conclusion of this thesis will be given in chapter 6.

# Chapter 2

## Theory

In principle, STM is very simple and beautiful, because essentially it just consists of an electric circuit. There are two electrodes, one is the tip, the other one is the sample under investigation. Between the two electrodes is a tunable resistance, the tunneling resistance, which is determined by the thickness of the vacuum-gap (or gas, liquid). A bias voltage is applied between the two electrodes. After bringing tip and sample close enough, in general a few Ångström [1 Ångström (Å) = 0.1 nanometer (nm) =  $10^{-10}$  m], a measurable tunneling current can flow through the gap due to the quantum mechanical tunneling effect, even though “mechanical point contact” between tip and sample is not reached. The amplitude of the tunneling current depends strongly (exponentially) on the separation between the two electrodes. Due to this sensitivity on the tip-sample distance, STM can achieve a highly spatially resolved information of the surface by scanning the tip and measuring the tunneling current flow.

### 2.1 The Tunneling Current

The tunneling effect is an important mechanism which is exploited in several condensed-matter physics experiments and can only be understood in terms of quantum theory.

As classical physics predict, a microscopic particle, e.g. an electron, will never be able to traverse a potential energy barrier with a higher energy than the particle.

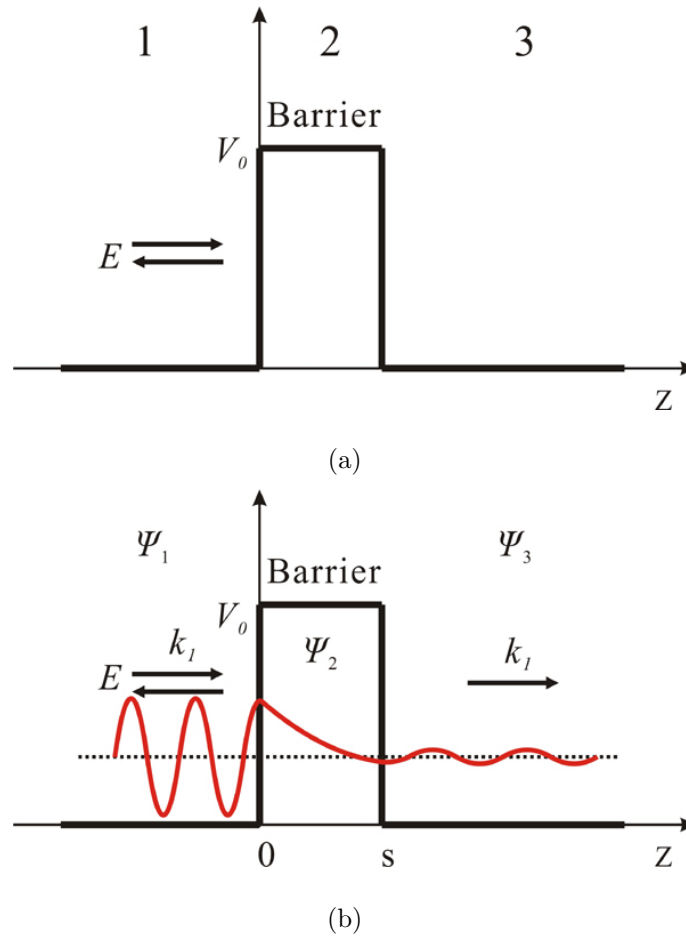


**Figure 2.1:** The difference between classical theory and quantum theory. (a) The classical theory: The electron can not traverse the barrier, when its energy  $E$  is lower than the potential barrier height  $V_0$ . (b) The quantum theory: The electron is allowed to pass the barrier since there is a non-vanishing wave function defined inside the barrier even if the energy of the electron is lower than the barrier height.

However, in quantum theory, the wave-particle dualism (de Broglie, 1923) may in fact allow this electron to traverse the barrier. This difference is illustrated in Figure 2.1.

In the classical physics picture, as shown in Figure 2.1(a), the electron will hit the barrier and reflect when its energy  $E$  is lower than the barrier height  $V_0$ . In the picture of quantum mechanics, by solving the time-independent Schrödinger equations for an electron with energy  $E$  and mass  $m$  impinging upon an one-dimensional rectangular potential barrier, as depicted in Figure 2.1(b), one obtains the wave functions  $\Psi_j$  for the three regions ( $j = 1, 2, 3$ ) [28] (here the electron is impinging onto the barrier

from the left side):

$$\Psi_1 = e^{ikz} + Ae^{-ikz} \quad (2.1a)$$

$$\Psi_2 = Be^{-\kappa z} + Ce^{\kappa z} \quad (2.1b)$$

$$\Psi_3 = De^{ikz} \quad (2.1c)$$

$$\text{with } k^2 = 2mE/\hbar^2 \text{ and } \kappa^2 = 2m(V_0 - E)/\hbar^2$$

where  $\hbar$  is Planck's constant divided by  $2\pi$ . By matching the  $\Psi_j$  and their first derivatives  $d\Psi_j/dz$  at the discontinuities of the potential  $V(z)$  at  $z = 0$  and  $z = s$ , one gets the transmission coefficient  $T$  which is the ratio of the transmitted current density  $j_t$  and the incident current density  $j_i$ :

$$j_t = \frac{-i\hbar}{2m} \left[ \Psi_3^*(z) \frac{d\Psi_3}{dz} - \Psi_3(z) \frac{d\Psi_3^*}{dz} \right] = \frac{\hbar k}{m} |D|^2 \quad (2.2a)$$

$$j_i = \frac{\hbar k}{m} \quad (2.2b)$$

$$T = \frac{j_t}{j_i} = |D|^2 = \frac{1}{1 + (k^2 + \kappa^2)^2 / (4k^2\kappa^2) \sinh^2(\kappa s)} \quad (2.2c)$$

If we consider the limit of a reasonable thick barrier ( $\kappa s \gg 1$ ), the transmitted current density  $j$  is given by

$$j \propto T \approx \frac{16k^2\kappa^2}{(k^2 + \kappa^2)^2} \cdot e^{-2\kappa s} \quad (2.3)$$

with the decay rate

$$\kappa = \frac{\sqrt{2m(V_0 - E)}}{\hbar}$$

The tunneling current depends strongly exponentially on the barrier width  $s$  and the square root of the effective barrier height  $(V_0 - E)^{1/2}$ . Assuming a barrier width of  $5 \text{ \AA}$  and an effective barrier height of  $4 \text{ eV}$  in an experiment, we get a value of about  $10^{-5}$  for the exponential factor, and  $\kappa \approx 1 \text{ \AA}^{-1}$  which means changing the barrier width by  $1 \text{ \AA}$  will lead to a change of current by about one order of magnitude. The extreme sensitivity of the tunneling current to the barrier width provides the extremely high spatial resolution of STM.

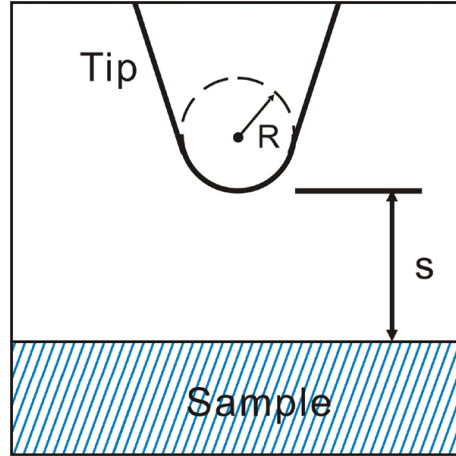


**Figure 2.2:** Schematic picture of tunneling geometry in the Tersoff-Hamann model. The tip is assumed to be locally spherical with radius of curvature  $R$ , where it approaches nearest the surface (hatched). The nearest distance is  $s$ . After J. Tersoff [29].

A more detailed analysis of the tunneling current used by Tersoff-Hamann [29, 30] based on the Bardeen approximation [31] gives the the tunneling current  $I$  for low applied voltage ( $V$ ) which is commonly used during the experiments [32–35]:

$$I \propto \int_{-\infty}^{\infty} \rho_s(E) \rho_t(E - eV) T(E, eV, s) [f(E - eV, \tau) - f(E, \tau)] dE \quad (2.4)$$

where  $\rho_s(E)$  and  $\rho_t(E)$  are the density of states (DOS) of the sample and the tip at the energy  $E$  ( $E$  is measured with respect to their Fermi levels), respectively.  $f(E, \tau)$  is the Fermi function with the temperature  $\tau$ . The transmission probability [28, 29, 35] is given by:

$$T(E, eV, s) = \exp \left\{ -2(s + R) \sqrt{\frac{2m}{\hbar^2} \left( \frac{\phi_s + \phi_t}{2} + \frac{eV}{2} - E \right)} \right\} \quad (2.5)$$

where  $m$  is the electron mass,  $\phi_s$  and  $\phi_t$  are the work functions of the sample and the tip respectively,  $s$  is the tip-sample distance and  $R$  is the tip radius. The schematic picture of the tunneling geometry is shown in Figure 2.2.

At low temperatures,  $k_B T \ll eV$  ( $k_B$  is the Boltzmann's constant), the Fermi function in Equation 2.4 can be approximated by a step function, thus the current



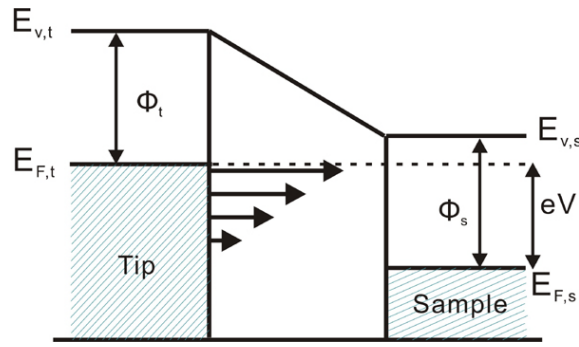


**Figure 2.3:** Schematic energy diagram of the tunneling junction. The energy bands of tip (left) and the sample (right) are filled with electrons up to the Fermi energies  $E_{F,t}$  and  $E_{F,s}$  (hatched), respectively. The difference between the vacuum energy levels ( $E_{v,t}$  and  $E_{v,s}$ ) and the Fermi levels are the work functions  $\Phi_t$  and  $\Phi_s$ . With positive bias  $V$  on the sample, current indicated by arrows is tunneling from occupied states of the tip to unoccupied states of the sample.

becomes

$$I \propto \int_0^{eV} \rho_s(E) \rho_t(E - eV) T(E, eV, s) dE \quad (2.6)$$

Figure 2.3 shows an energy diagram that graphically illustrates the tunneling process. On the left side the LDOS of an electronically featureless tip is shown. On the right side the LDOS of a metallic sample is plotted. The energy bands of tip and sample are filled with electrons up to the Fermi level  $E_{F,t}$  and  $E_{F,s}$ , respectively. The tunneling current originates from electrons crossing the barrier from occupied states of the tip to unoccupied states of the sample when a positive sample bias ( $V > 0$ ) is applied. Therefore the current is proportional to the sum of the density of unoccupied states of the surface, weighted by the transmission coefficient.

## 2.2 Topographic Imaging by STM

The combination of tunneling and scanning capability was successfully achieved with the invention of STM in the early 1980s. Various modes can be operated in STM to get information from the studied system.

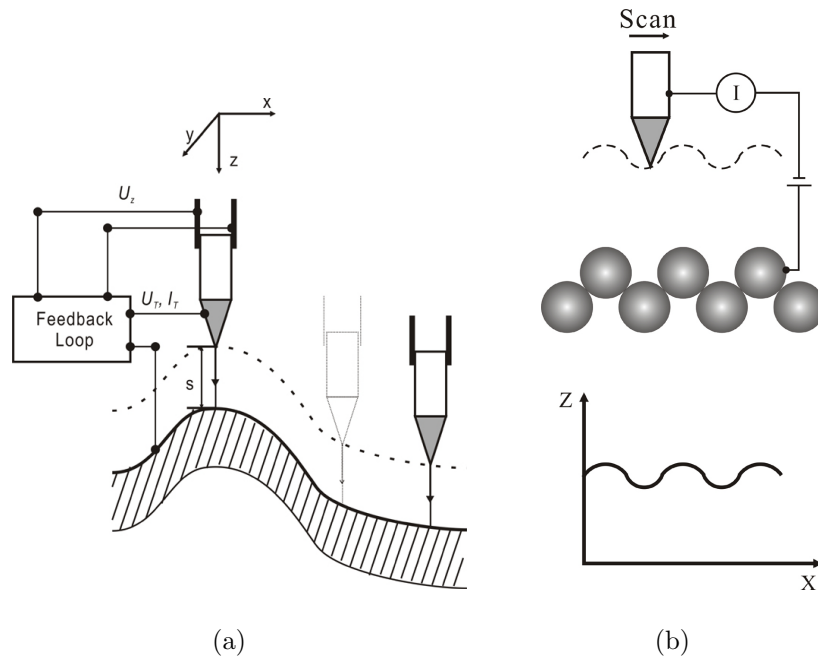


**Figure 2.4:** Schematic illustration of the constant current mode of STM operation (see text). After R. Wiesendanger [28].

Figure 2.4 shows the basic principle of the first and most widely used mode of STM operation, namely constant current imaging (CCI) mode. The sharp metal tip which can move in the  $x$ -,  $y$ - and  $z$ - directions is positioned over the surface. During scanning a feedback loop adjusts the height of the tip so that the tunneling current flowing between tip and sample is kept constant. The height ( $z$ ) adjustment is performed by applying an appropriate voltage  $U_z$  to the  $z$  piezoelectric ceramic while the lateral tip position ( $x, y$ ) is determined by the corresponding voltages  $U_x$  and  $U_y$  applied to the  $x$  and  $y$  piezoelectric ceramics. (Piezoelectric material reacts to an applied electric field by extending in the direction perpendicular to the field. Typical length change rate of a piezoelectric tube is a few  $10 \text{ \AA}/\text{V}$  [36].) Therefore, the recorded signal  $U_z(U_x, U_y)$  can be translated into the “topography”  $z(x, y)$ .

Although the contour map  $z(x, y)$  is often referred to as the topographic image of the sample surface, it is generally not solely the arrangement of atoms on a surface which determines  $z(x, y)$ . The contour map  $z(x, y)$  reflects a constant current surface according to the experimental measurement procedure.

According to the Tersoff-Hamann approach Equation 2.4, the STM images ob-

tained in the constant current mode can be represented as the contour maps of LDOS at  $E_F$  evaluated at the center of curvature of the effective tip (see Figure 2.2).

A significant drawback of the CCI mode lies in the finite response time of the feedback loop which limits the scan speed and data acquisition time considerably. An alternative way is to use so called constant height imaging (CHI) mode which switches off the feedback completely during scanning. In this mode, the modulation of the tunneling current with the sensitivity of the exponential dependence of the current of tip-surface distance reflects the atomic-scale “topography”. The application of the CHI mode is limited to surfaces that are nearly atomically flat over the imaged surface where the amplitudes of topographic features with high spatial frequencies have to be smaller than the tip-surface distance itself. A significant drawback of the CHI mode compared with the CCI mode lies in the lack of vertical height ( $z$  direction) information [37, 38].

Usually, topographic STM data on a large scale are collected using the CCI mode, while the CHI mode is used after “zooming” to selected smaller surface areas of sufficient flatness.

## 2.3 Scanning Tunneling Spectroscopy

### 2.3.1 $dI/dV$ spectroscopy

Differentiating Equation 2.6 with respect of  $V$  leads to the differential conductance:

$$\frac{dI}{dV} \propto \rho_s(eV)\rho_t(0)T(eV, eV, s) + \dots \quad (2.7)$$

plus three terms proportional to  $d\rho_t/dV$ ,  $dT/dV$  and  $dT/ds \cdot ds/dV$ . These are usually neglected provided that the LDOS of the tip  $\rho_t$  is constant and the transmission probability  $T$  varies smoothly in the range of the applied voltages, and the tip is held at constant height  $s$ . Thus the differential conductance reduces to:

$$\frac{dI}{dV} \propto \rho_s(eV)T(eV, eV, s) \quad (2.8)$$

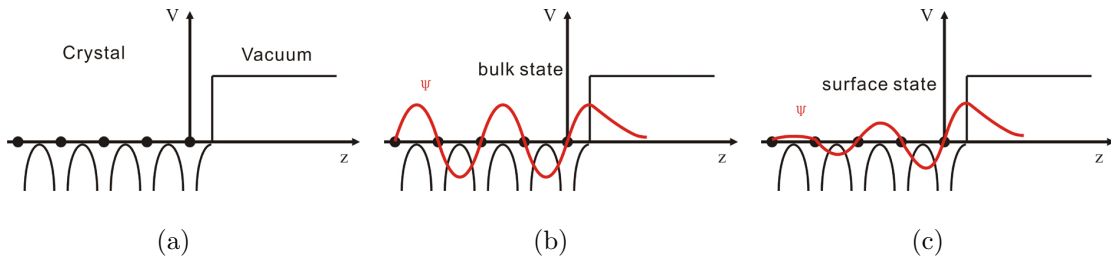


**Figure 2.5:** (a) Schematic diagram of the potential which an electron is exposed to near the crystal surface (left crystal, right vacuum). Two types of wave functions of a semi-infinite crystal can be distinguished: (b) bulk states and (c) surface states (red line).

the differential conductance is proportional to the surface LDOS multiplied by the transmission probability. This is the basic assumption for interpreting STS measurements.

### 2.3.2 Surface states

The solution of the Schrödinger equation for the periodic potential associated with an infinite crystalline lattice is known to reproduce successive bands of allowed energies, which are always separated by forbidden energy gaps. The situation is different when the presence of a surface breaks the periodicity and, hence, alters the boundary condition for the Schrödinger equation [Figure 2.5(a)]. Due to this, two types of solution are available.

- The first type of solution [Figure 2.5(b)] corresponds to *bulk states* with wave functions extended into the bulk and decaying exponentially into the vacuum.
- The second type of solution [Figure 2.5(c)] corresponds to *surface states* whose wave functions exist in the band gaps but are localized in the surface region, decaying exponentially both into the bulk and vacuum.

In particular the noble metal (Cu, Ag, Au) (111) surfaces host so-called Shockley surface states [39] which have been extensively studied by photo-electron spectroscopy (PES) [40–43]. The electrons in these surface states move freely parallel to the surface and form a quasi two-dimensional free electron gas which exhibit a constant density

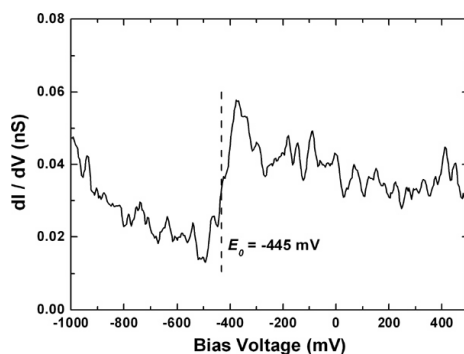


**Figure 2.6:**  $dI/dV$  spectra on Cu(111) surface at 4.7 K.  $E_0$  indicates the onset of the surface states (FILE: 2J18S024.IV).

of states [44]. These surface states can be measured by means of STS. If the current  $I$  is monitored while the voltage  $V$  is swept with open feedback loop, the energy of the electrons  $eV$  is swept from below the onset of the surface state band  $E_0$  across the onset, an increased differential conductance is noticed. Figure 2.6 shows the surface state of a clean terrace of Cu(111) by measuring  $dI/dV$  spectra. The principle feature of the spectra is that at -445 mV sample bias, there is a clear edge. This edge indicates that at 445 meV below the Fermi-level is the onset of the surface state of Cu(111) [45, 46].

Since the wave vector of surface states electrons is parallel with the surface, the tunneling transmission probability in Equation 2.5 needs to be modified as shown in Equation 2.9 [47]:

$$T(E, V, s) = \exp \left\{ -2(s + R) \sqrt{\frac{2m}{\hbar^2} \left( \frac{\phi_s + \phi_t}{2} + \frac{eV}{2} - (E - E_{\parallel}) \right)} \right\} \quad (2.9)$$

where  $E_{\parallel} = E - E_0 = \hbar^2 k_{\parallel}^2 / 2m^*$ ,  $k_{\parallel}$  is the surface electrons wave vector, and  $m^*$  is the effective electron mass.

Figure 2.7 shows a simulation of tunneling current  $I$  and  $dI/dV$  spectra on Cu(111) surface. We assume that the tip-surface distance is held at a constant height 5 Å ( $s + R$ ), the work function of the tip is assumed to be 5.40 eV (tungsten tip) and the sample work function is set to 4.94 eV [Cu(111)] [48], the bias voltage is ramped from -1 V to +1 V. In Figure 2.7(a), we assume that the surface LDOS below the onset of surface states (-445 meV) is 1, above the onset of surface states, this value

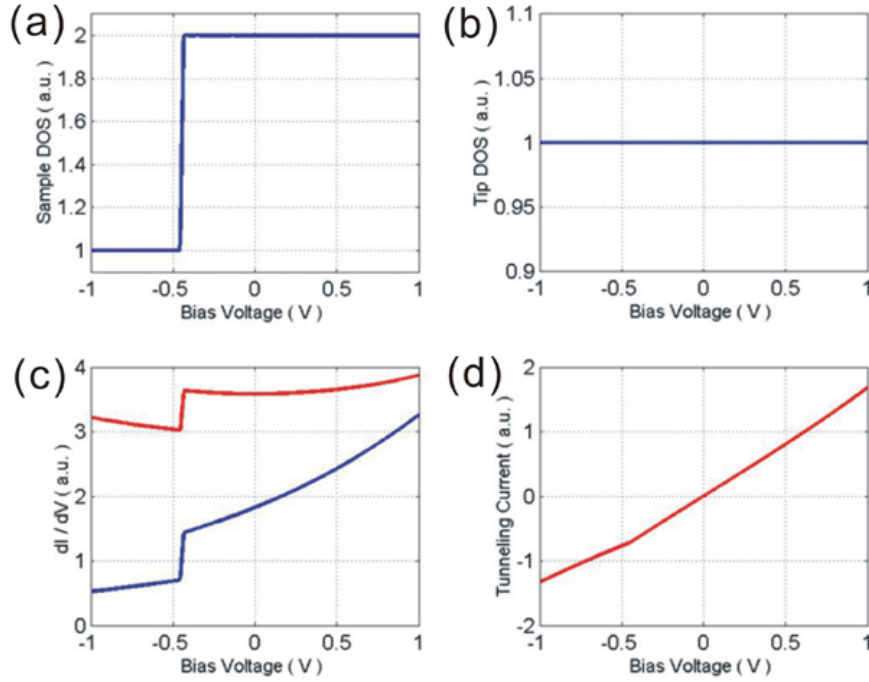


**Figure 2.7:**  $dI/dV$  simulations on Cu(111). (a) Modeled sample LDOS. (b) Modeled tip LDOS. (c) Simulated  $dI/dV$  spectra (blue curve: using Equation 2.8. red curve: using Equation 2.6, the spectrum is offset by 2 a.u. vertically for clarity.). (d) Simulated current using Equation 2.6.

linearly increases to 2 within a 20 meV energy region. The tip density of state is constant, assumed to be 1, as shown in Figure 2.7(b). The simulated differential conductance  $dI/dV$  using Equations 2.8 and 2.9 is presented in the blue curve in Figure 2.7(c). The main feature of Figure 2.7(c) is that there is a clear sharp increase of differential conductance at the surface states onset energy. To compare the  $dI/dV$  spectra to the numeric results, we also calculate the tunneling current shown in Figure 2.7(d) using Equations 2.6 and 2.9, and then numerically differentiate the current to get  $dI/dV$  which is presented in the red curve in Figure 2.7(c). Near the onset energy preset, both  $dI/dV$  spectra exhibit almost the same feature as the model surface LDOS does. However below and above the onset, the red curve is almost flat while the blue curve increases almost lineally with  $V$ . This difference is due to the fact that the tunneling transmission probability  $T$  is a smooth, monotonically increasing function of the applied voltage  $V$  according to Equation 2.5. If we use Equation 2.8,

at any fixed location the voltage dependence of the tunneling transmission probability contributes a smooth background because the compensating term “ $dI/dV$ ” is neglected, and the STS information is superimposed on the background. Because the increase is smooth and monotonic, structure in  $dI/dV$  spectra can usually be assigned to the changes of density states.

The  $dI/dV$  spectra can be directly measured by means of lock-in technique [49–51].

### 2.3.3 $I(z)$ curve

Since the electron wave functions decay exponentially in the  $z$  direction normal to the surface towards the vacuum region, the tunneling current depends exponentially on the tip-sample distance ( $z = s + R$ ) as expected [29, 30]:

$$I \propto \exp(-2\kappa z) \quad (2.10)$$

where the decay rate  $\kappa = (2m\bar{\phi})^{1/2}/\hbar$ ,  $\bar{\phi} = (\phi_s + \phi_t)/2$  (called the apparent barrier height),  $\phi_s$  and  $\phi_t$  are the values of work function of sample and tip, respectively, one can obtain the information about the tunneling barrier by performing  $I$  versus  $z$  spectroscopy,  $\bar{\phi} = -\hbar^2/8m \cdot (d\ln I/dz)^2$ . Thus one can obtain:

$$\bar{\phi}(\text{eV}) = -0.95 \cdot \left[ \frac{d\ln I(\text{\AA})}{dz(\text{\AA})} \right]^2 \quad (2.11)$$

Figure 2.8(a) shows the simulation of  $I/z$  spectra with different assumed sample work functions  $\phi_s$  (4.0, 4.5 and 5.0 eV, respectively) using Equations 2.5 and 2.6. The bias voltage is assumed to be 150 mV, and  $z$  is ramped from 2 to 6 Å. The work function of tip is assumed to be 5.4 eV. Figure 2.8(b) presents the simulation of  $\ln I$  versus  $z$ , thus the apparent barrier heights are determined to be about 4.68, 4.93 and 5.18 eV, respectively, which are very close to the preset values (4.70, 4.95 and 5.20 eV, respectively).

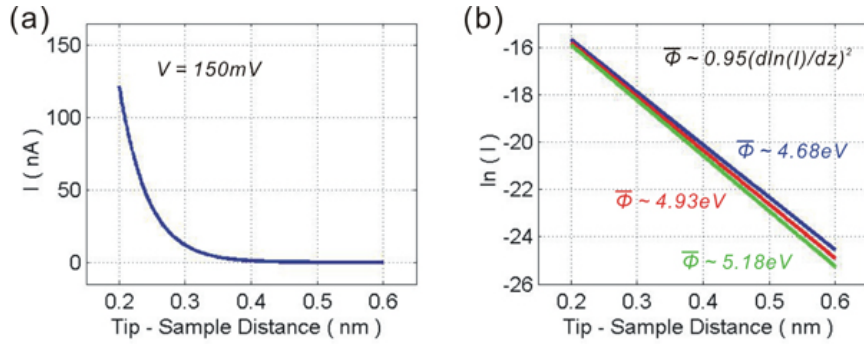


**Figure 2.8:**  $I/z$  simulations. (a) Simulated current at the distance from 2 to 6 Å with the sample work function = 5.4 eV. Bias voltage = 150 mV. (b) Simulated  $\ln I$  versus  $z$  with the sample work function = 4.0 (blue line), 4.5 (red line) and 5.0 eV (green line), respectively.

### 2.3.4 $dI/dV$ map

$dI/dV$  map is a combination of the STM topographical imaging modes (CCI or CHI mode) with  $dI/dV$  spectroscopy. In this mode, the  $dI/dV$  signal, measured with a lock-in amplifier is recorded simultaneously with the acquired constant-current or constant-height images. The  $dI/dV$  map is commonly used to unravel the spectroscopic information. However, the problem with acquiring  $dI/dV$  map in CCI mode is that the tip-sample distance changes to keep the current constant during measuring, thus changes the transmission probability  $T$  (Equation 2.5). Dividing the  $dI/dV$  map by  $\exp(-z)$  can correct this problem [52]:

$$\rho_s(x, y, eV) \propto \frac{dI}{dV}(x, y, V) \cdot \frac{1}{\exp[-z(x, y, V)]} \quad (2.12)$$

where  $z(x, y, V)$  is taken from the topography.

### 2.3.5 Molecular adsorbates spectroscopy

In the molecular tunneling process, the electron can tunnel directly from the tip to an empty molecular orbital (MO) of the molecule or from an occupied molecular orbital to the tip depending on the sample bias. This resonance-like process is important to STM because it is thought to be the principal mechanism allowing molecular imaging [53–55]. Figure 2.9 is a schematic picture for a typical molecular tunnel



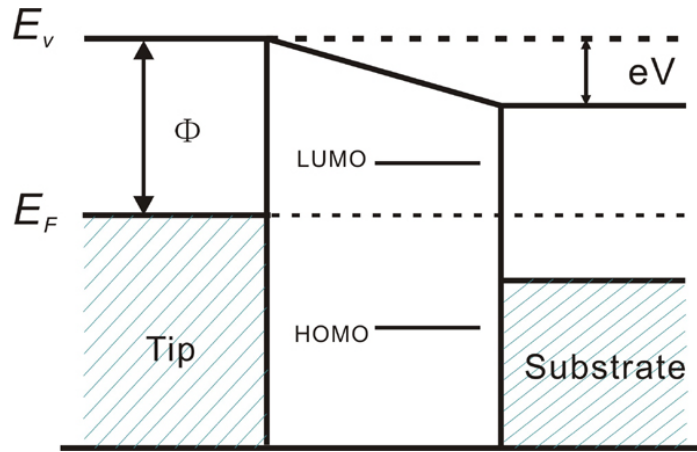


**Figure 2.9:** Energy diagram for a model molecule tunneling junction. The dashed region represents the filled states of the substrate and tip. The area in the center represents the adsorbate. The HOMO and LUMO of a molecule are shown.

junction. The electron states are filled up to  $E_F$ , and the work functions of the tip and substrate are given by  $\phi$ . The hatched regions in Figure 2.9 represent completely filled metal orbitals. The highest occupied molecular orbital (HOMO) and lowest unoccupied molecular orbital (LUMO) of a molecule are also shown in Figure 2.9. For simple calculation, the weak interactions between the tip and molecule, as well as substrate and molecule, are assumed to cause a shift in molecule's zero of energy but do not produce significant changes in its level spacing. However this assumption is not true for every molecule/metal combination.

When a small voltage  $V$  is applied to the substrate, since the molecule is closer to the substrate than to the tip, its potential almost moves with that of the substrate. At this point electron in the filled states of the tip can tunnel into the LUMO of the molecule if the LUMO is lower the  $E_F$  of the tip and electron in the HOMO of the molecule can tunnel into the empty states of the tip if the HOMO moves higher than  $E_F$  of the tip. These will result steps in the  $I(V)$  curve thus peaks in the  $dI/dV$  versus  $V$  at these critical energy levels [56].

Figure 2.10 presents a simulation of tunneling current  $I$  and differential conductance  $dI/dV$  spectra of a molecule using Equations 2.4 and 2.5. The LDOS of molecule is assumed to exhibit a gap between the HOMO and LUMO. Four Gaussian

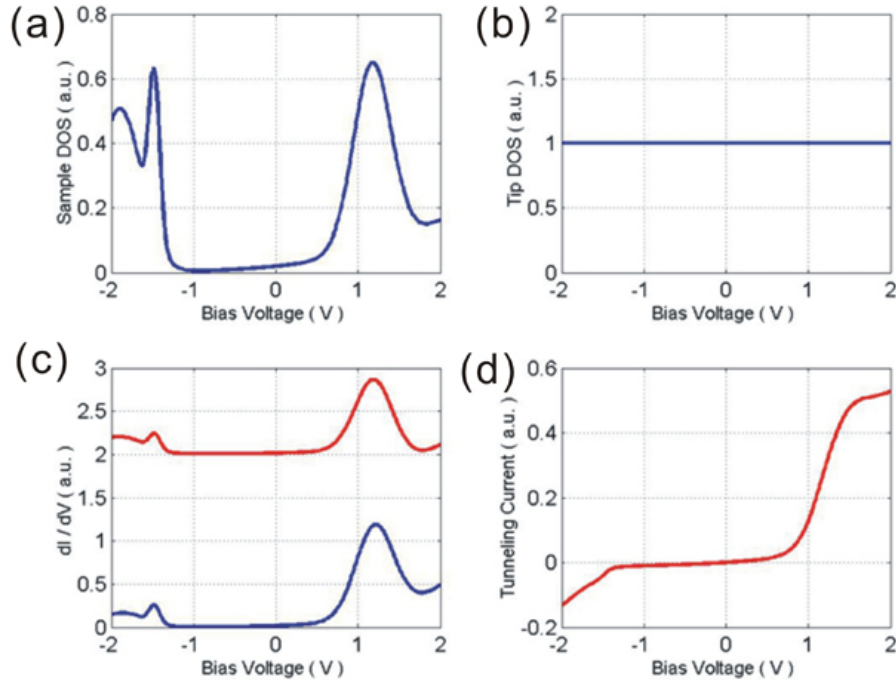


**Figure 2.10:**  $dI/dV$  simulations of molecule. (a) Modeled molecule LDOS. (b) Modeled tip LDOS. (c) Simulated  $dI/dV$  spectra (blue curve: using Equation 2.8. red curve: using Equation 2.6, the spectra is offset by 2 a.u. vertically for clarity.). (d) Simulated current using Equation 2.6.

functions are used to simulate the LDOS the molecule. The HOMO is assumed to locate at 1.48 eV below  $E_F$  [full width half maximum (FWHM): 0.13 eV], a HOMO+1 is assumed to locate at 1.90 eV below  $E_F$  with FWHM equaling 0.52 eV, and the LUMO is assumed to locate at 1.17 eV above  $E_F$  (FWHM: 0.33 eV). The constant LDOS of the tip is assumed to be 1. The bias voltage is ramped from -2 to +2 V, the tip-surface distances are held at a constant height 5 Å, the values of work functions of tip and surface are 5.40 and 4.94 eV [48], respectively (for the simplicity of calculation, the work function of the sample is assumed to be unaffected by the adsorbate).

Comparing simulated  $dI/dV$  spectra [Figure 2.10(c)] with the starting LDOS of molecule [Figure 2.10(a)] shows that they have peaks in nearly the same position. So the  $dI/dV$  technique can reveal the electronic structure of the molecule. However, the intensities of the peaks are quite different. Unoccupied states are observed much

---

more clearly and with higher intensity in the  $dI/dV$  spectra than the occupied states which is a result of the fact that most of the tunneling electrons arise from states near the Fermi energy of the negatively biased electrode. This simulation demonstrates that the intensities of the peaks observed in  $dI/dV$  spectra are not proportional to the LDOS, particularly at negative sample bias [57, 58]. And the  $dI/dV$  spectra of molecular adsorbates on the sample surface somehow deviates from this approximation also because of the molecule-surface and molecule-tip interactions which are not taken into account within our calculations.



# Chapter 3

## Experimental Setup

The work presented in this thesis was carried out with a low-temperature, UHV STM designed and built by Jörg Kliewer [45]. In this chapter, the aspects of the STM apparatus are generally described. A description of the new designed heating stage as part of the work of this thesis is also given. General procedures of sample preparation during the experiments are briefly presented.

### 3.1 Overview

A schematic drawing of the UHV system is sketched in Figure 3.1. It consists mainly of two parts, a preparation chamber for the preparation of samples and an STM chamber which contains the STM and cryostats. The two main chambers are connected through a DN40 tube on the rear side. There is also a small load lock for introducing samples, tips and evaporators into the vacuum system without breaking the vacuum. The entire system is mounted on a steel frame which is placed onto pendulum air dampers (Figure 3.1a). All three chambers are evacuated with turbo molecular drag pumps (*Pfeiffer Vacuum*, Asslar) which are back pumped by rotary vane pumps, preparation chamber has an additional titanium sublimation pump. During STM measurements all mechanical pumps are shut down and separated from the preparation and STM chambers with gate valves (*MDC*, UK), and the vacuum is maintained by two iongetter pumps (*Varian*, Italy). With this system, the pressure

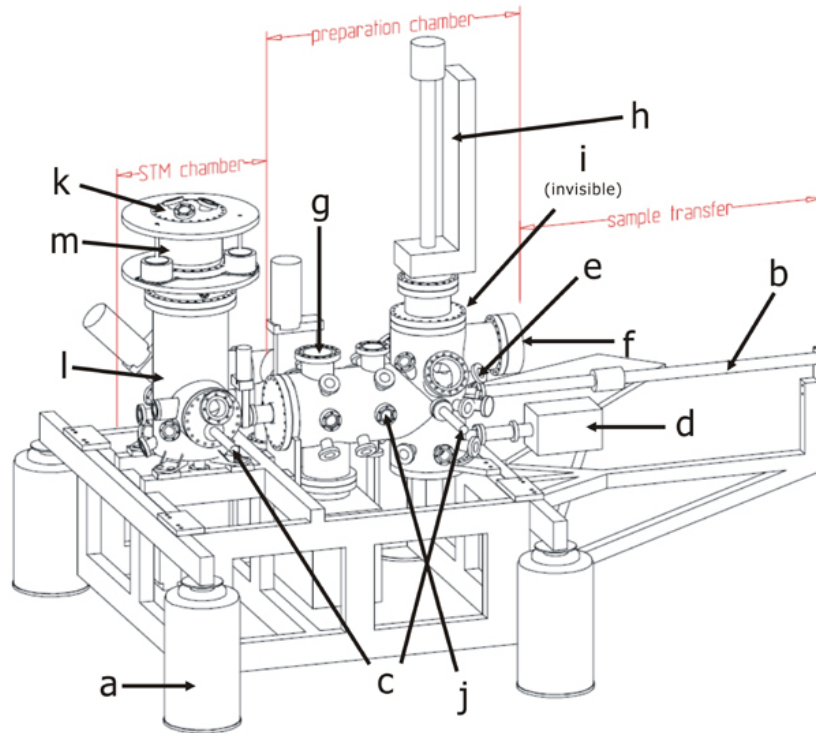


**Figure 3.1:** Schematic overview of the UHV system. The damping system (a) and the vacuum components (b = magnetic motion drive, c = wobble sticks, d = quadrupole mass spectrometer, e = quartz micro balance, f = LEED, g = AES, h = 4 axes manipulator, i = sputter gun (invisible), j = electron emitter, k = liquid Helium dewar, l = liquid Nitrogen dewar, m = membrane bellow). After J. Kliewer [45].

can easily be reached to  $10^{-10}$  mbar.

Two magnetic motion drives (Figure 3.1b, *VG Scienta*, UK) at the load lock and preparation chamber are used for moving samples and equipments between these chambers. The main tools for carrier transfer in the preparation and STM chambers are two magnetically driven wobble sticks (Figure 3.1c, *VG Scienta*, UK).

The STM is controlled by a commercial ECS digital electronics [59] and software (SPM 6.0). The current between tip and sample is amplified and converted by an I/V-converter (DLPCA-100) with a transimpedance gain ranging from  $10^3$  to  $10^9$  V/A (low noise mode) or  $10^{11}$  V/A (high speed mode). The feedback loop is completely implemented by software and runs on a DSP processor [60] hosted by a Personal Computer board.

### 3.1.1 Preparation chamber

The preparation chamber is used for preparation and storage of samples and UHV equipments such as tips and evaporators. It consists of usual vacuum science instruments: A cold cathode gauge for measuring the pressure down to  $1 \times 10^{-11}$  mbar, a quadrupole mass spectrometer (*Pfeiffer*, Germany) for residual gas analysis (Figure 3.1d), a quartz micro balance (*Intelmetrics*, UK) for evaporation monitoring and calibration (Figure 3.1e), a Low Energy Electron Diffraction (LEED, *VSI*, Germany) and an Auger Electron Spectroscopy (AES, *Staub*, Germany) for sample characterization and analysis (Figure 3.1f and g), a 4-axis manipulator for sample heating and precise positioning (Figure 3.1h), a sputter gun for sample and tip cleaning (Figure 3.1i) and an electron emitter for tips annealing (Figure 3.1j).

The samples and equipments enter the preparation chamber from the load lock and are stored at a carousel. The carousel can store eight samples, evaporators or tips.

### 3.1.2 STM chamber

The STM chamber is equipped with two cryostats: A 6-liter liquid Helium dewar (Figure 3.1k) which can hold liquid helium or liquid nitrogen mounted on the top flange, a 5-liter gold-covered liquid Nitrogen dewar (Figure 3.1l), which surrounds the liquid Helium dewar for reducing thermal radiation, allowing us performing measurements at 4.7 K for 24 hours. The top flange is vibrationally isolated from the rest of the vacuum system through a membrane bellow (Figure 3.1m) which is kept from collapsing by a second isolation stage made of simple air dampers. To get rid of the vibration due to the boiling Nitrogen, after filling liquid Nitrogen, the outer dewar is pumped with a rotary vane pump to solidify the Nitrogen during the measurement.

The details of the STM head are described in Jörg Kliewer's thesis [45]. Here we just give a brief description. The overview of STM is shown in Figure 3.2. The sample (a) is mounted on the slider (b) which is driven by coarse piezos (c). The tip (d) is mounted horizontally on the segmented tube piezo scanner (e). The screws

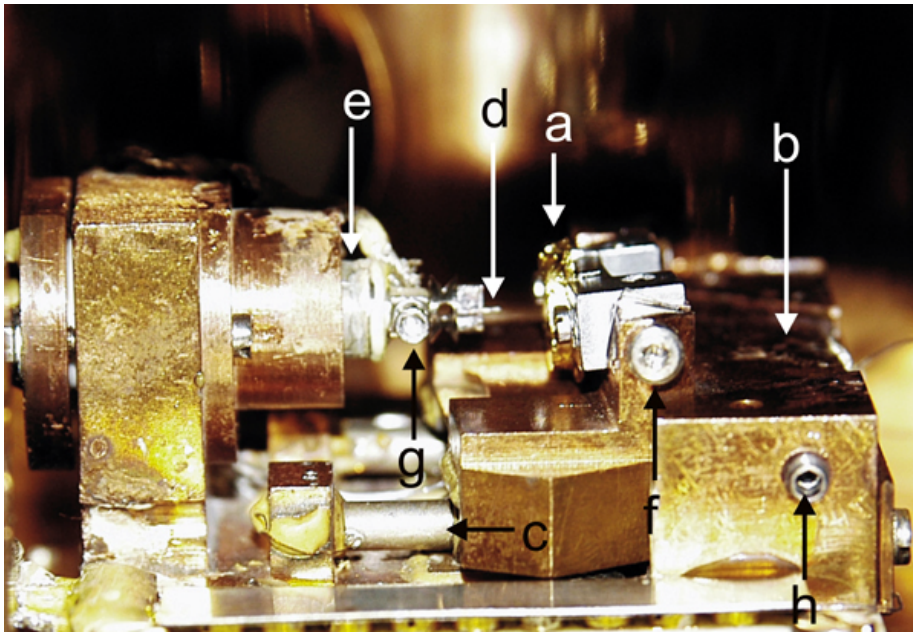


**Figure 3.2:** Overview of the STM (see text).

fixing the sample (f), the tip (g) and the slider (h) can be handled by using the screwdriver attach to the head of the wobble stick. Tip and sample can be changed in UHV with the wobble stick mounted on the STM chamber.

## 3.2 Modification of the Heating Stage

Due to the lifetime expiry and low heating efficiency of the old heating stage attaching to the manipulator, as part of the work in this thesis, we<sup>1</sup> designed and commissioned a new heating stage for sample preparation at beginning of the project.

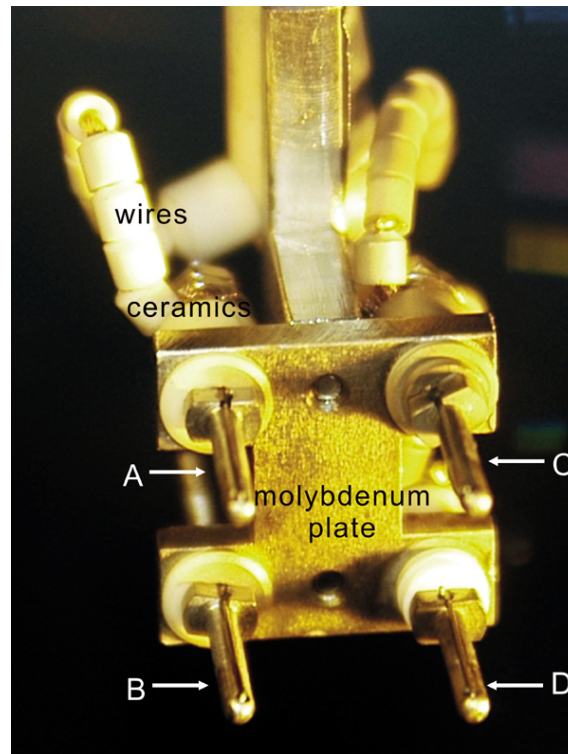
The purpose was to fabricate a heating stage on which high voltage electron bombardment can be used to anneal the sample up to more than 1000 K and current can be directly passed through the sample in case of preparing semiconducting surfaces such as silicon. Other requirements are that thermocouple should be attached to the stage in order to measure the temperature, the setup should enable exchange of the filament and the sample, as well as sputtering and annealing of the sample.

Figure 3.3 shows a photograph of the new designed heating stage. The plate, the

---

<sup>1</sup>Dr. J. Kuntze and myself





**Figure 3.3:** Photograph of new designed heating stage. Pins A, C and D are insulated from molybdenum plate by  $\text{Al}_2\text{O}_3$  ceramics. Pin B is directly attached to the plate. All the wires are protected against ground with ceramic rings (see text).

pins and all the screws are made of molybdenum to sustain high annealing temperatures. Pins A, C, and D are electronically insulated from the molybdenum plate by  $\text{Al}_2\text{O}_3$  ceramics, pin B is directly attached to the plate. The filament is attached to pins A and B, while the sample is at pins C and D. The filament is made of tungsten wire (diameter 0.2 mm) doped with 1% thorium to enhance the electron emission efficiency. Currents pass from pin A to B (ground) through the filament. High voltage (1 ~ 2 kV) is applied to the sample on the pins of C and D when electron bombardment is used. A thermocouple (type K) is attached to pin C. The heating stage can be freely rotated from  $0^\circ$  to  $270^\circ$  for sputtering and annealing conveniently, also the sample and the filament can be easily replaced.

## 3.3 Sample Preparation

Once the UHV conditions of the system are ensured, the experiments can be started with sample preparation, including preparing a clean substrate surface and evaporating molecules onto the surface.

### 3.3.1 Preparation of atomically clean substrates

Before introduction into the preparation chamber, the sample undergoes a set of cleaning treatments, such as mechanical polishing, chemical etching, rinsing in distilled water, etc. All the pre-treatments of commercial samples were mainly done by the manufactures except our Cu(111) sample<sup>2</sup>. However, all this processing constitutes rather a pretreatment stage, as the final preparation of an atomically clean surface can be conducted only *in situ* in the UHV preparation chamber.

For the metal substrates, we adopt standard ion sputtering and subsequent annealing procedure to clean the sample, namely several (3 ~ 5) strong cycles of 1 kV-Ar<sup>+</sup> sputtering for 20 minutes plus 20-minute annealing at 850 K followed by several (1 ~ 3) soft cycles of 0.6 kV-Ar<sup>+</sup> sputtering for 15 minutes plus 15-minute annealing at 700 K.

For cleaning semiconducting surfaces, currents are directly introduced through sample from pin C to D at the heating stage. By this method sample can be heated up to 1300 K so that the Si(111)-(7 × 7) reconstruction can be prepared. There is also another option to mount the sample on the wobble stick and pass currents directly through the sample using two pins which are electronically connected to a feed through outside.

### 3.3.2 Molecule deposition

For the molecules with low vapor pressure such as larder, NaCl and CoPc, thermal sublimation can be employed for molecule deposition.

---

<sup>2</sup>The Cu(111) sample was mechanically polished using fine aluminium powder and chemically etched using 3.5 % H<sub>3</sub>PO<sub>4</sub> by myself.



**Figure 3.4:** Photography of the UHV button heaters (Figure source: Online product catalog of HeatWave Labs Inc.).

Pure molecules (purity  $\geq 99\%$ , usually in powder) are introduced into a mouth which is made of tantalum foil attached onto the top of a button heater (*HeatWave Labs, Inc.*, USA, see Figure 3.4) and installed into the UHV preparation chamber on the evaporation stage. A current is passed through the button heater to heat up the molecules. While increasing the current slowly ( $\sim 0.1$  A/20 min), the evaporation rate is monitored by the quartz balance. As soon as there is a response (jump) in the quartz balance signal, currents are reduced by  $0.1 \sim 0.3$  A and kept for more than 24 hours to remove the impurities in the powder. Deposition rate is calibrated to  $\sim 0.1$  ML/min by quartz balance afterwards. The typical powers of 0.1 ML/min deposition rate for larder, NaCl and CoPc molecules are 2, 4.5 and 4 W, respectively. After all these procedures, molecules are thermally sublimated at preset evaporation rate from the evaporator onto the clean surface which is put at the position where the quartz balance was. During sublimation, the pressure of the preparation chamber will slightly increase to high  $10^{-9}$  mbar. More precise calibration of the coverage is carried out by imaging the topography with STM.



## Chapter 4

# A Molecular Wire on Metal Surfaces

The semiconductor industry has seen a remarkable miniaturization trend, driven by many scientific and technological innovations. The demand for smaller and smaller devices in microelectronics will lead to the synthesis of molecular scale devices. One possible approach to implement such circuits is the use of hybrid-molecular and mono-molecular devices [61], in which a single molecule will integrate the elementary functions and interconnections required for computation. Using single molecules as functional units (e.g. diodes) connected to metallic contacts in hybrid molecular devices has already been proposed 30 years ago [62]. Since then, molecules have been found useful as wires [63–65], switches [66, 67], even diodes or transistors [13, 68, 69].

An inherent problem of all devices where a molecule is to be interfaced to a surface is whether and how its functionality will be affected by the substrate. Largeish molecules can promote local restructuring [70] or extended faceting of the substrate [71]. Even anticipating the structure of an adsorbed molecule from its gas-phase or crystalline conformation is far from trivial since different substrates may favor different conformations, as demonstrated for CuTBPP (Cu-tetra-3,5 *di-tert-butylphenyl porphyrin*) [21]. Attaching molecules to atomic steps, e.g. to establish electronic contact between the molecule and the step, introduces additional degrees of freedom which affect the structure of the molecule.

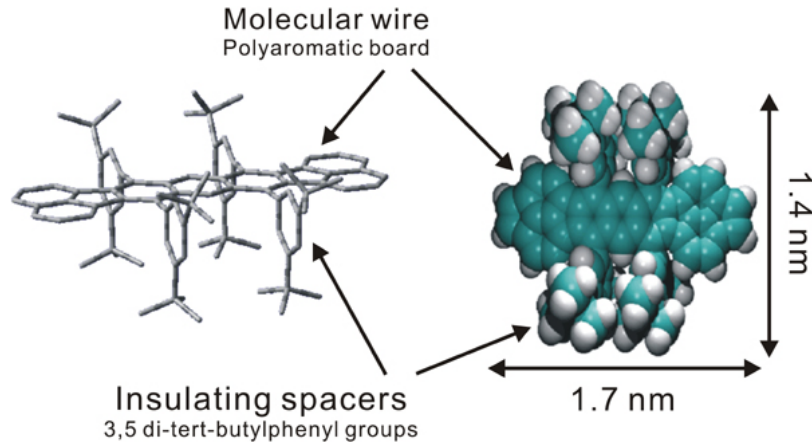


**Figure 4.1:** Three-dimensional model of the lander molecule in its gas phase conformation. The four DTP legs are oriented perpendicularly to the central molecular wire.

In this chapter, we will investigate a prototype of a short molecular wire, so-called lander molecule ( $C_{90}H_{98}$ , see Figure 4.1), adsorbed on different substrates. The lander molecule consists of a conjugated central polyaromatic board, the conducting molecular wire because of the delocalized  $\pi$  orbitals of the benzene rings. At both extremities, the wire is terminated by naphthalene groups assuring a more efficient contact point. The wire is lifted parallel above the surface by four DTP (*di-tert-butylphenyl*)-substituents acting as insulating legs, maintaining the intrinsic electronic function away from the underneath supporting surface. The molecule is suggested about 1.7 nm long and 1.4 nm wide, and has a HOMO-LUMO gap about 2.3 eV.

The initial concept was proposed by Langlais *et al.* [63]. The schematics of the experimental principle together with theoretically calculated STM profiles are shown in Figure 4.2. The end naphthalene groups are designed to be put in interaction with an atomic ordered electrode to control the electronic contact between the molecular wire and the nano-electrode at the atomic scale. And the molecular wire is electronically decoupled from the lower terrace by using four DTP legs.

Experiments were performed in an ultrahigh chamber (base pressure in the low  $10^{-10}$  mbar range and below  $10^{-11}$  mbar for the preparation and STM chamber, respectively). Sample preparation and lander molecule sublimation followed the procedure described in Section 3.3. The sample was held at room temperature during

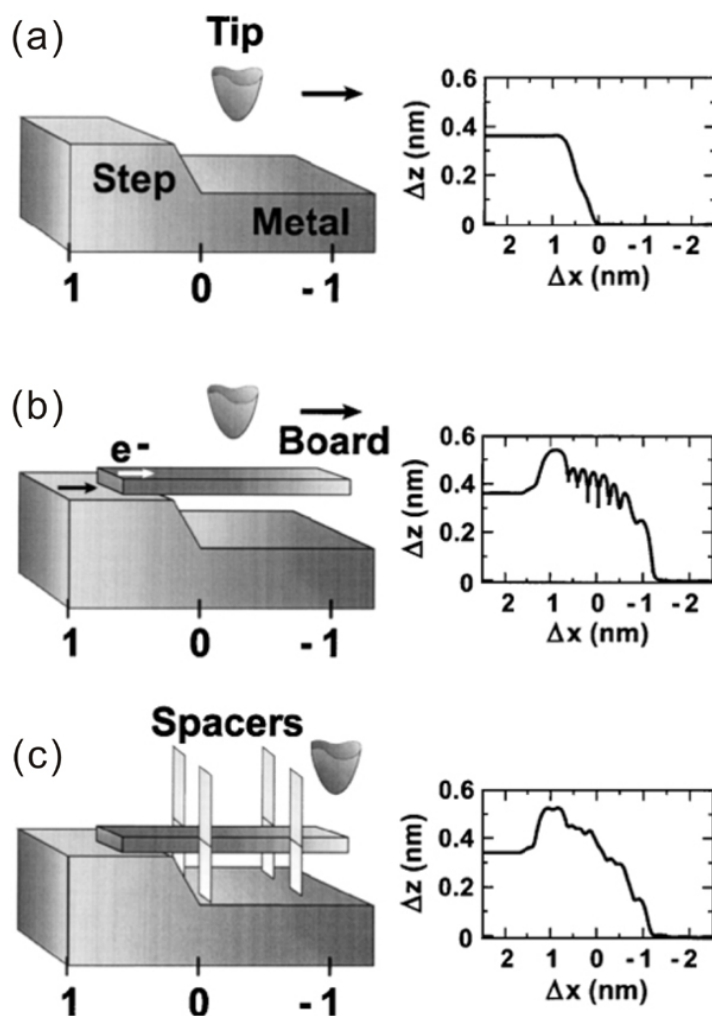


**Figure 4.2:** Schematics of the experimental principle together with theoretically calculated STM profiles. (a) Double atomic step edges offer a suitable height to adsorb molecular wire. Calculated STM cross-sectional profile on the double atomic step edges. (b) Molecular wire electronically coupled to the step. The evanescent wave function from the top terrace leaks into the wire. The profile shows an alternation of nodes and antinodes of the molecular orbitals. (c) The molecular wire is electronically decoupled from the lower terrace by using four insulating spacer units, which modify the fine structure of the profile. After V. J. Langlais [63].

deposition and was transferred to the STM and cooled down to 4.7 K *prior to* imaging. Electrochemically etched tungsten tips were prepared *in situ* by electron bombardment and  $\text{Ar}^+$  sputtering before insertion in the STM. During image acquisition, the tips were formed by field emission and controlled tip-sample contacts with the

tip positioned over bare terrace to avoid contamination with molecular fragments. Owing to this tip sharpening procedure, we assume that the tip apex is comprised of metal (Cu, Ag, or Au) atoms.

## 4.1 Lander on Cu(100)

### 4.1.1 Conformations of lander on Cu(100)

Figure 4.3(a) shows an STM image of lander molecules adsorbed on Cu(100). The lander decorate atomic steps and adsorb on terraces as isolated units and aggregates of a few (typically 2–4) molecules. At low coverages (approximately 0.1 ML) the molecules adsorb exclusively at step edges, indicating sufficiently high diffusion rates on Cu(100) at room temperature to promote migration to step and kink sites. In earlier experiments with Cu-TBPP equipped with the same DTP substituents as molecular legs, no molecular diffusion on Cu(100) was observed at room temperature [72]. This indicates a lower diffusion barrier for the lander molecule on Cu(100) compared to Cu-TBPP on this surface. We attribute this difference to a better adaptability of the Cu-TBPP legs to the surface atomic corrugation. Due to steric hindrance, the lander legs do not have the possibility of a large rotation around their  $\sigma$ -bond attachment to the board in comparison with Cu-TBPP. At the low temperatures used for imaging in our experiments, molecular diffusion is completely suppressed.

The molecules appear as four bright lobes in STM images. For extracting the details of molecular conformations and bonding geometries, measured STM images and cross sections are compared with calculated ones. For the calculations, the electron scattering quantum chemical method (ESQC) routines [74] were used along with molecular mechanics optimization of the lander physisorption on the Cu(100) terraces and step edges. The ESQC routine is based on the calculation of the full scattering matrix of the tunnel junction of the STM. The description of this junction encompasses the surface, the adsorbate, the tip apex, and both bulk material supporting the tip apex and the surface. The tip apex was described by five layers of Cu atoms ordered in a pyramidal shape with (111) facets. The lander molecule was described



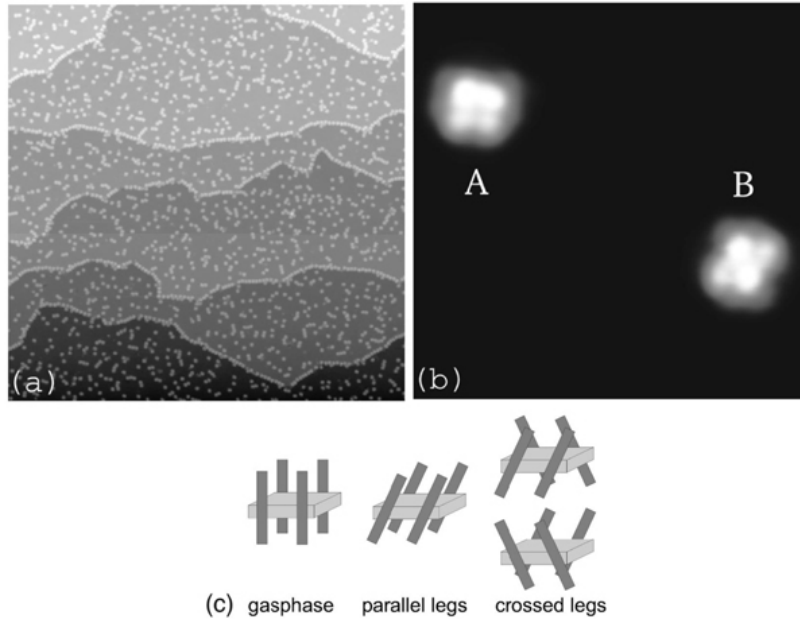


**Figure 4.3:** (a) Lander molecules adsorbed on Cu(100). The steps are completely decorated and excess molecules are adsorbed on the terraces. ( $I_t = 0.1$  nA,  $V_s = 1010$  mV, scan size =  $200 \times 200$  nm<sup>2</sup>, FILE: 0K23T001.IMG). (b) Two isolated molecules in different conformations. ( $I_t = 0.05$  nA,  $V_s = 2000$  mV, scan size =  $9 \times 9$  nm<sup>2</sup>, FILE: 0G30T025.IMG). (c) Illustration of the schematic conformations. The molecule is symbolized as a board with four legs (the DTP groups) attached. After J. Kuntze [73].

taking into account all its valence molecular orbitals. For every tip apex position, 695 molecular orbitals were used to describe the electronic properties of the STM junction containing the lander. All the electronic interactions inside this junction were calculated using a semi-empirical extended Hückel approximation with a double zeta basis set to properly reproduce the tip apex wave function in space away from the outermost tip atom. The molecular mechanics routine used to optimize the lander geometry in the tunnel junction is a standard MM2 force field routine [75] with generalized potential for surface metal atoms. According to ESQC calculations, the tunneling occurs primarily via the DTP substituents, while the central molecular wire contributes very little to the tunneling current at high junction resistance of typically 10 G $\Omega$  in our experiments.

Owing to this intramolecular contrast, three molecular conformations have been

identified on flat terraces from high-resolution STM images, two of which are presented in Figure 4.3(b). The schematic drawings in Figure 4.3(c) illustrate the main differences between the two conformations. Due to the symmetry of the  $\sigma$  bond between the DTP substituents and the central wire, the spacer legs can rotate around the bond axis. In the gas phase, the DTP groups are perpendicular to the central molecular board, as was found also for Cu-TBPP [21, 72]. For adsorbed molecules, this minimum-energy conformation is altered by molecule-substrate interactions, forcing the bond rotation angles to change. Due to steric hindrance, the legs positioned on the same side of the central molecular wire always rotate in the same direction, resulting in two qualitatively different conformations: (i) The DTP legs on both sides of the central wire rotate in the same direction. We call this conformation the parallel-legs conformation. It leads to an overall square shape of the molecule in STM images. (ii) the DTP legs on both sides rotate in different directions. This is called the crossed-legs conformation. It leads to rhombic shaped molecules as imaged by STM. The third conformation is a mirror symmetric enantiomer of the later. The molecule is not chiral in the gas phase, chirality is only induced upon adsorption.

According to molecular mechanics calculations the crossed-legs conformation is lower in energy by 2 kcal/mol (87 meV/molecule) in agreement with the experimentally observed ratio of parallel-legs molecules to the far more abundant crossed-legs molecules at low temperature (ratios of 1:50 and less are typically observed). Reducing the STM junction resistance while scanning over a single lander can result in a change from the parallel to the crossed-legs conformation and vice versa, confirming that the energy difference between these two conformations is small.

To extract the detailed molecular conformation of the lander, calculated images of the different conformations are compared with the corresponding experimental images. If only rotation of the DTP groups around the  $\sigma$  bond is allowed in the calculations, only a poor agreement between experimental and calculated images is achieved. By considerable bending of the DTP legs towards the central board, accompanied by a substantial lowering of the board from 0.7 to 0.37 nm above the surface, the agreement with experimental images and cross sections is improved considerably (Figure 4.4).

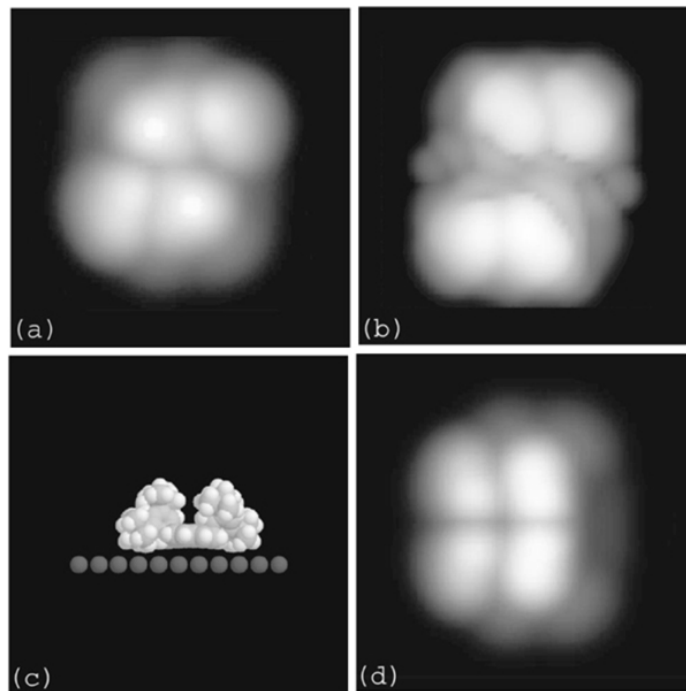


**Figure 4.4:** Simulated STM images for different conformations. The central molecular board is oriented along the image horizontal, size of all images is  $3.3 \times 3.3 \text{ nm}^2$ . (a) After optimizing the geometry for the crossed-legs conformation [cf. Figure 4.3(b), molecule ‘B’, and 4.3(c)] taking into account the experimental data. The central molecular wire is lifted  $0.37 \text{ nm}$  above the surface by the DTP legs. (b) Same conformation before optimizing, height of the central wire is  $0.7 \text{ nm}$ . (c) Ball model of the optimized conformation in (a). Note the inward bending of the DTP legs towards the molecular board. (d) Image of the parallel-legs conformation after optimization [cf. Figure 4.3(b), molecule ‘A’, and 4.3(c)]. After J. Kuntze [73].

This deformation of the leg upon adsorption is governed by the van der Waals attraction of the central board towards the surface. This attraction forces the board to approach the surface and constrains the legs to be twisted. There are two major twisting directions per leg: a rotation around the  $\sigma$  bond and a bending of this bond. A full  $90^\circ$  rotation of each leg is forbidden by the steric hindrance of the two legs on the same side of the board. As a consequence, the constraint is shared between the bending of the  $\sigma$  bond and a rotation around each bond.

The detailed intramolecular contrast also stems from the leg rotation. STM im-

ages always reveal one bright and one less bright bump on each side of the molecule, which is explained as follows: Upon rotation, the top  $\text{CH}_3$  group of one leg is located above the bottom  $\text{CH}_3$  group of the second leg on the same side of the molecular board [cf. schematic drawings in Figure 4.3(c)]. Hence, if the tip is positioned above this top  $\text{CH}_3$  group, the tunneling path towards the metal encompasses two such groups, which reduces the tunneling resistance and makes the tip retract, i.e. the leg appears higher. For the other leg the tunnel current flows via the molecular orbitals of the top  $\text{CH}_3$  group directly towards the surface, resulting in a high resistance and a shallow appearance of this leg.

The weak elevation surrounding molecules both in experimental and calculated images is in part due to molecular features (imaging of the  $\text{CH}_3$  groups at the bottom of the legs), but as well induced by the lateral extension of the tunneling tip. When the atom at the apex has already passed the molecule and the tip starts approaching the surface, the extended facets at the sides of the apex contribute to the tunnel current giving rise to these features. This is not to be confused with a double-tip artifact. In experimental images, the tip-size effects and the molecular fine structure are indistinguishable and cannot be deconvoluted.

After the extraction of the conformations of the landers adsorbed on a terrace, it is of special interest to know how the molecule adsorbs at the edge of a step, since it was designed for establishing an electronic contact between the end of the central molecular wire and edge of a step stabilized at the substrate surface [63]. In contrast to Ref. [63], we focus on single instead of double steps, since the former are the naturally occurring step type on clean  $\text{Cu}(100)$  surface. While for double steps on  $\text{Cu}(100)$  the molecule was proposed to adsorb on the lower terrace with the central board perpendicular to the step, at single steps on the same surface we find a completely different adsorption geometry. From comparison of ESQC-calculated STM images with experimental data of the lander adsorbed on step edges, we conclude that the molecule adsorbs with the central board parallel to the step. Two legs remain on the upper terrace and the other two legs adsorb on the lower terrace (Figure 4.5).

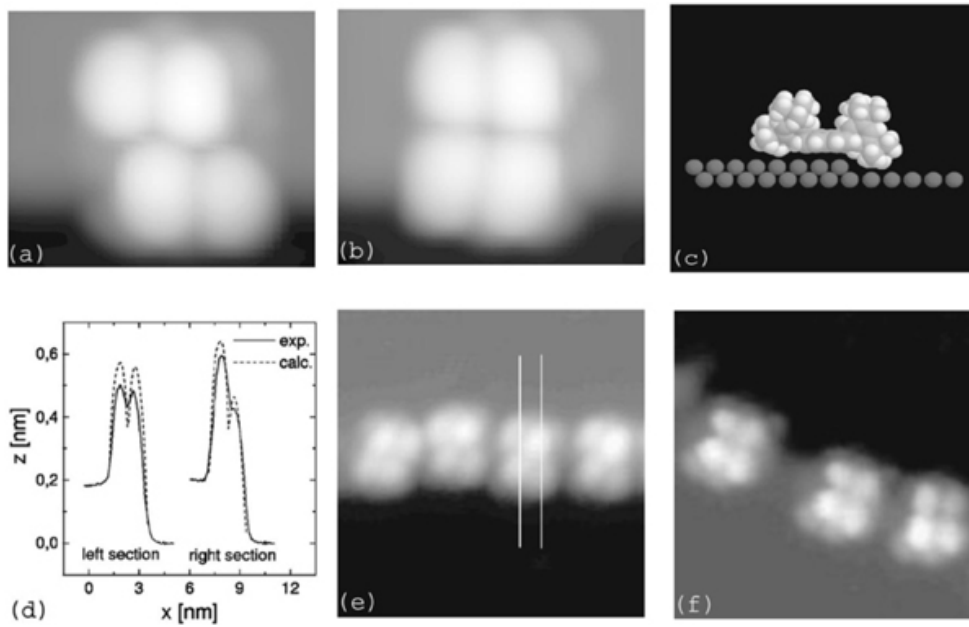


**Figure 4.5:** Molecules adsorbed at monoatomic steps. (a) Calculated image with molecule in the lowest energy conformation [crossed-legs, central molecular board oriented parallel to the step with two DTP substituents resting on the upper terrace, cf. (c)]. (b) Calculated image with the molecule in the parallel-legs conformation. Orientation and leg placement as in (a). (c) Ball-model used for calculating (a). The molecule is viewed from the front with its board parallel to the step. (d) Comparison between experimental and calculated sections across the molecule shown in (a) and (e). Sections on the right are displaced for clarity. (e) Experimental image of a few molecules in the conformation shown in (a). Due to the flexibility of the bonds, the respective bond rotation angles of the molecules may differ slightly, depending on the exact orientation with respect to the step. The lines indicate the direction of the sections in (d). ( $I_t = 0.1$  nA,  $V_s = 2000$  mV, scan size =  $8 \times 8$  nm<sup>2</sup>, FILE: 0K17T015.IMG). (f) STM images of three molecules in the conformation shown in (b). ( $I_t = 0.1$  nA,  $V_s = 1000$  mV, scan size =  $6.7 \times 6.7$  nm<sup>2</sup>, FILE: 0G26T007.IMG). After J. Kuntze [73].

As judged from a comparison of cross sectional profiles [Figure 4.5(d)], the qualitative agreement is good, but small height difference between experimental and simulated scans still remain. However, since the molecule's flexibility leads to scatter in the experimental data of approximately  $\pm 0.2$  Å, indicating a variety of slightly different adsorption geometries, a further refinement does not appear to be useful.

Qualitatively, due to the flexibility of the bonds between the legs and the wire, two conformations can also be distinguished for the adsorption geometry along the step edge, a parallel and a crossed-legs conformation. For the crossed one, molecular mechanics indicates a slightly lower van der Waals total energy of -89.5 kcal/mole (-3.883 eV/molecule) compared to -89.3 kcal/mol (-3.874 eV/molecule) for a parallel-leg conformation. Judging from the small amount of parallel-legs molecules observed experimentally along the step, this small energy difference of only 9 meV per molecule is sufficient at low temperature to trigger an almost exclusive adsorption in the crossed-legs conformation. Other adsorption geometries are not observed, in agreement with their comparatively high total energies. For example, the conformation with the central board perpendicular to the step edge and two legs resting on the upper terrace is next lowest in energy, but already differs by more than 20 kcal/mol from the parallel-board conformations.

In conclusion, in this section we have investigated conformational changes induced upon adsorption of lander molecule on Cu(100). The molecule was designed as a central molecular board lifted above the substrate by four DTP substituents and should act as a molecular wire when contacted to an atomic step. Comparison of experimental and calculated STM images allows the extraction of the detailed conformations of molecules adsorbed on terraces and at single atomic steps. It turns out that the DTP legs are rotated and significantly deformed due to the interaction of the molecules's central molecular wire with the surface. This results in a lowering of the central board to only 0.37 nm above the surface, compared 0.7 nm for the unperturbed molecule. As a consequence, at monoatomic steps, this molecule is stabilized with the wire parallel to the edge, preventing good electronic contact between the wire's end groups and the step.

### 4.1.2 Chiral structures of lander on Cu(100)

As mentioned in Section 4.1.1, lander molecule shows two mirror symmetric enantiomers in crossed-legs conformation adsorbed on Cu(100) surface. One may expect this will lead to a chiral arrangement of lander molecule adsorbed on Cu(100) surface.

Chiral surface are of great interest due to their importance in enantioselective catalysis, e.g. in pharmaceutical industry. Using chiral catalysts, the yield of products with the desired handedness can be drastically increased [76]. Apart from this industrial perspective, the study of chiral molecules is fascinating from a fundamental point of view. Since the recent determination of absolute chirality of adsorbed molecules by STM [77], many interesting phenomena involving chiral structures have been observed over the last few years. E.g., chiral supramolecular assemblies of nitronaphthalene clusters were found [78] that could be manipulated using the STM tip [79], chiral recognition at the single molecule level has been reported [79–81] and the chiral restructuring of surfaces due to adsorption of hydrocarbon molecules has been observed [70, 82].

Chirality can be bestowed onto a surface in a number of ways. One is to cut the surface along a high Miller-index direction leading to kinked surfaces that can be chiral [83], another is the formation of supramolecular assemblies of chiral molecules [84]. Both methods would lead to overall, global chirality. *Local* chirality can be observed when a non-chiral molecule creates a chiral motif upon adsorption and eventually assembles into supramolecular geometries which are chiral themselves. In this section we show such a case, where lander molecule is adsorbed on Cu(100). The molecule is found to adopt two mirror symmetric conformations which assemble into enantiomerically pure domains with chiral symmetry. Macroscopically, the surface is still racemic owing the the presence of tow mirror symmetric molecular conformations.

Between the two principal conformations — parallel-legs and crossed-legs conformations, the crossed-legs version is energetically preferred and thus far more abundant experimentally. Figure 4.3(c) shows that there are two ways to cross the legs on both sides of the molecule, namely clockwise or anticlockwise rotation of the legs on one side of the central board (when viewed from the side), each leading to a nearly rhombic image. One can define a long and short axis of the molecule (cf. Figure 4.6), connecting the dim and bright protrusions in the STM image, respectively. Close inspection of the cross-legs molecule in Figure 4.6 reveals that the short and long axis

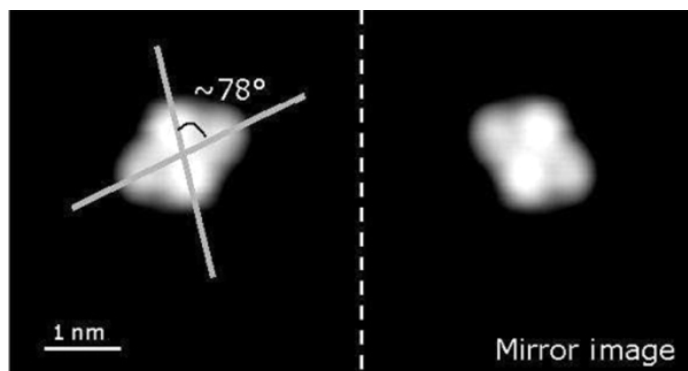


**Figure 4.6:** Close view of the crossed-leg lander molecule of Figure 4.3. The lines indicate the direction of the molecular axes. On the right side, the mathematical mirror image of the molecule is displayed. After J. Kuntze [85].

are not perpendicular to each other, as they would be in a rhombus. The molecular outline is rather a parallelogram and thus chiral, since mirror images of this conformation cannot be superimposed onto each other by translation or rotation. This chirality of the individual molecules has implications for molecular assemblies.

At increasing coverage, the molecules arrange themselves in short chains along  $[01\bar{2}]$ ,  $[02\bar{1}]$ ,  $[012]$  and  $[021]$  directions [Figure 4.7(a), (b)]. The crystallographic  $\langle 110 \rangle$  directions as determined from low-energy electron diffraction (LEED) and extended straight atomic steps produced by tip-sample contact are indicated in the figure. The molecular chains are oriented at an angle of  $18 \pm 2^\circ$  with respect to these high-symmetry directions. Care was taken to exclude image distortion by thermal drift or piezo creep.

Interestingly, only molecules of like symmetry align in the same chain. This finding is consistent with previous observation for other racemic mixtures of chiral molecules (either intrinsically 3D-chiral or 2D-chiral after adsorption) [86,87]. In most cases, chiral discrimination can be traced back to functional groups interacting via hydrogen bonding, e.g. hydroxy groups [84,88] or carboxylic groups [81]. The lander molecules, however do not exhibit such groups and can be expected to interact predominantly via Van der Waals forces. Since there are small partial charges associated with the  $\text{CH}_3$  groups on the DTP-legs, weak local dipole moments exist on the legs, but they are



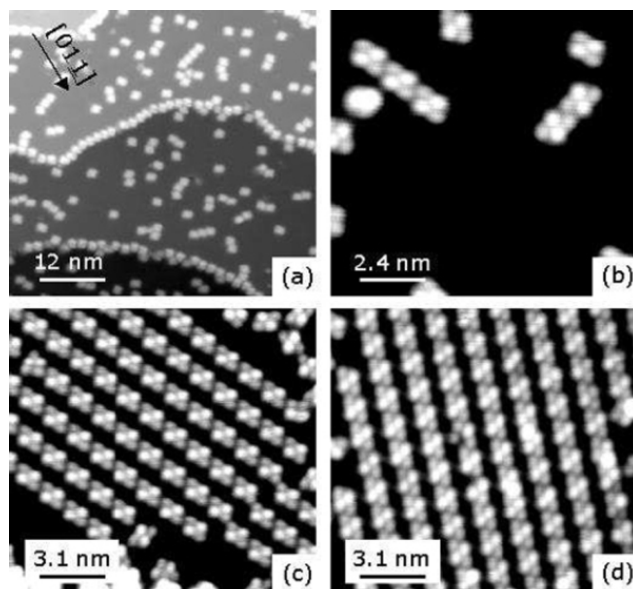


**Figure 4.7:** Assembly of (a-b) short chains and (c-d) extended supramolecular domains. The orientation of all images is identical, as indicated by the arrow in (a). Only molecules of identical symmetry are observed to align. The domains in (c-d) are mirror symmetric with respect to the  $[01\bar{1}]$  direction. Two more equivalent domain orientations which are symmetric with respect to the  $[011]$  direction, are not shown here. FILE: (a) 0K22T004.IMG (b) 0K23T007.IMG (c) 0K20T013.IMG (d) 0K20T005.IMG. After J. Kuntze [85].

oriented mainly perpendicular to the plane of the molecular board and will contribute only little to the in-plane molecular arrangement. A similar case of spontaneous resolution into conglomerates for van der Waals dominated interaction was reported for Naphto[2,3-a]pyrene [89].

The molecular chain directions do not correspond to symmetry directions of the sample, which makes the assembly itself chiral, without taking into account the chirality of the individual molecules. At higher coverages the molecules assemble into domains along the same directions as the short chains. Figure 4.7(c), (d) show two such domains which are mirror symmetric with respect to the  $[01\bar{1}]$  direction [cf. arrow in Figure 4.7(a)]. One readily verifies that also the molecular units are mirror images of each other. For the domains, the distance between molecular centers in adjacent rows is  $(1.63 \pm 0.1)$  nm and the distance between molecules in a row is  $(1.56 \pm 0.1)$  nm, with an angle of approximately  $(84 \pm 2)^\circ$  between these two di-

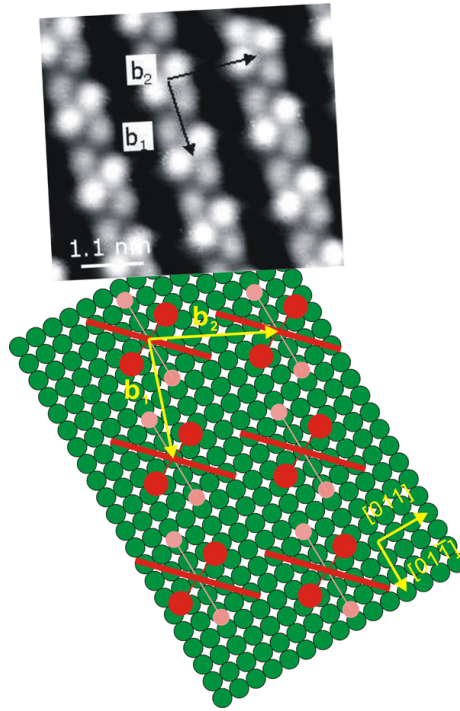


**Figure 4.8:** Close view of the structure within a domain and corresponding overlayer registry. The model is rotated to match the crystallographic orientation of the experimental image. The small and big red circles represent the dim and bright lobes of lander molecule. And the slim red rectangle represents the wire board. Solid green circles represent the copper atoms on Cu(111) substrate. ( $I_t = 0.1$  nA,  $V_s = 1000$  mV, scan size =  $5.3 \times 5.3$  nm<sup>2</sup>, FILE: 0K20T017.IMG). After J. Kuntze [85].

rections. The angle between molecular chains in mirror symmetric domains as in Figure 4.7(c), (d) is  $(36 \pm 2)^\circ$ . The other two equivalent domains symmetric with respect to the  $[011]$  direction are not shown here. We note that extended disordered regions remain between the domains, predominantly with shorter chains and few isolated molecules which have either assembled into chains nor domains. The size of ordered domains is of the order of 15 nm in diameter. We suggest that by fine-tuning the growth conditions as deposition rate and substrate temperature, the size may be increased.

Figure 4.8 shows a closeup of a molecular domain with the unit vectors of the overlayer and the corresponding model. The unit vector  $\vec{b}_1$  along the direction of molecular rows is oriented along  $[01\bar{2}]$  for the domain orientation shown, and the unit

vector across the rows  $\vec{b}_2$  is oriented along [031]. In terms of the substrate unit vectors  $\vec{a}_1 = a_0/2[01\bar{1}]$  and  $\vec{a}_2 = a_0/2[011]$ ,  $a_0 = 0.362$  nm being the Cu lattice constant, the overlayer can be given in matrix notation as  $(6 \ -2, \ 3 \ 6)$ . In this thesis, the overlayer matrix notation with preferred vectors will be used [86]. The lengths of  $\vec{b}_1$  and  $\vec{b}_2$  are 1.62 and 1.72 nm, respectively, and the angle enclosed by the vectors is  $82^\circ$ . The angle between  $\vec{b}_1$  vectors in mirror symmetric domains is  $36.8^\circ$  (each is  $18.4^\circ$  with respect to the symmetry directions  $\langle 110 \rangle$ ). This agrees well with the experimental values within the estimated uncertainties. As the molecular adsorption site cannot be determined from our STM images, the unit vectors in Figure 4.8 are arbitrarily chosen to connect top sites. The matrix notation for the mirror symmetric domain [cf. Figure 4.7(c)] is  $(6 \ 2, \ 3 \ -6)$ , for the other two domains we find  $(-2 \ 6, \ 6 \ 3)$  and  $(2 \ 6, \ -6 \ 3)$ . The overlayer unit vectors are always chosen according to the model in Figure 4.8, with  $\vec{b}_1$  pointing along the chain direction and  $\vec{b}_2$  pointing across the chains, with an angle of less than  $90^\circ$  between the unit vectors. The overlayer unit vectors are always expressed in terms of the substrate unit vectors  $\vec{a}_1, \vec{a}_2$  given above.

The question why the molecules order along the given directions is still open. Formation of the directed molecular chains is natural consequence of a fixed orientation of a single molecule with respect to the substrate and a preferred intermolecular alignment. Electrostatic interactions should favour a close packing of the molecules to increase the attractive forces. The configuration which maximizes molecular interactions will then be energetically preferred and result in a specific intermolecular arrangement. This may also explain the spontaneous resolution into homochiral phases, provided that homochiral interactions dominate. Such a scenario was indeed observed previously [80]. On different substrate, such as Cu(111), adsorbed lander molecules show a complete different arrangement, this will be discussed in Section 4.2.2.

In this section, we have observed chiral arrangements of lander molecules on Cu(100). At low coverage, the molecules assemble in enantiomerically pure molecular rows along the  $[01\bar{2}]$ ,  $[02\bar{1}]$ ,  $[012]$  and  $[021]$  directions. These rows arrange into enantiomerically pure domains at higher coverage, for which an overlayer model is presented. The overlayer geometry is also chiral by itself but due to the presence

of mirror symmetric molecules the surface is racemic on a macroscopic scale. The molecular interactions responsible for the chiral arrangements are proposed to be mainly due to van der Waals forces and steric effects, since no substantial partial charges or strong hydrogen bonds exist for these molecules.

### 4.1.3 Lander on films of NaCl on Cu(100)

Besides evaporating lander molecules directly on pristine Cu(100) surfaces, we also explored the adsorption of lander molecules on thin films of NaCl grown on Cu(100). NaCl is one of the candidates for thin insulating films useful for the assembly of future experimental molecular devices.

NaCl crystals were first melted by heating and then evaporated onto Cu(100) bare surface. Figure 4.9(a) shows a NaCl island on Cu(100). NaCl grows with fcc(100) termination on Cu(100) at a sub-monolayer coverage and covers substrate steps in a carpet-like fashion. The step height is 0.36 nm for the first NaCl-Cu step, and 0.11 nm for the second NaCl layer. The STM image of such a structure was calculated by the Toulouse group to identify the chlorine atoms as the imaged protuberance. After adsorption of lander molecules, an atomic square lattice of approx. 0.4 nm and anomalous corrugation of 0.18 nm [Figure 4.9(b)] were repeatedly observed at 1 V sample bias and 20 pA tunnel current, indicating the trapping of a molecule under the tip, acting as an amplifier of the atomic corrugation [90].

Figures 4.9(c) and 4.9(d) show the situation after room-temperature adsorption of lander molecules onto this surface. The molecules do not stick on NaCl layers and the NaCl islands remain free of molecules. However, images of anomalous corrugation as shown in Figure 4.9(b) indicate that there may be molecules on the NaCl islands.

Since tip-molecule interactions are greatly reduced at low tunnel currents (hence large tip-sample separation), the electronics and wiring of the STM were modified as to minimize our detectable tunnel current. We are now capable of tunneling at currents as low as 500 fA, whereas before it was limited to approximately 10 pA. Despite this effort, we could not acquire stable images of Lander molecules adsorbed on NaCl. In view of the rapid diffusion and/or low sticking probability of lander

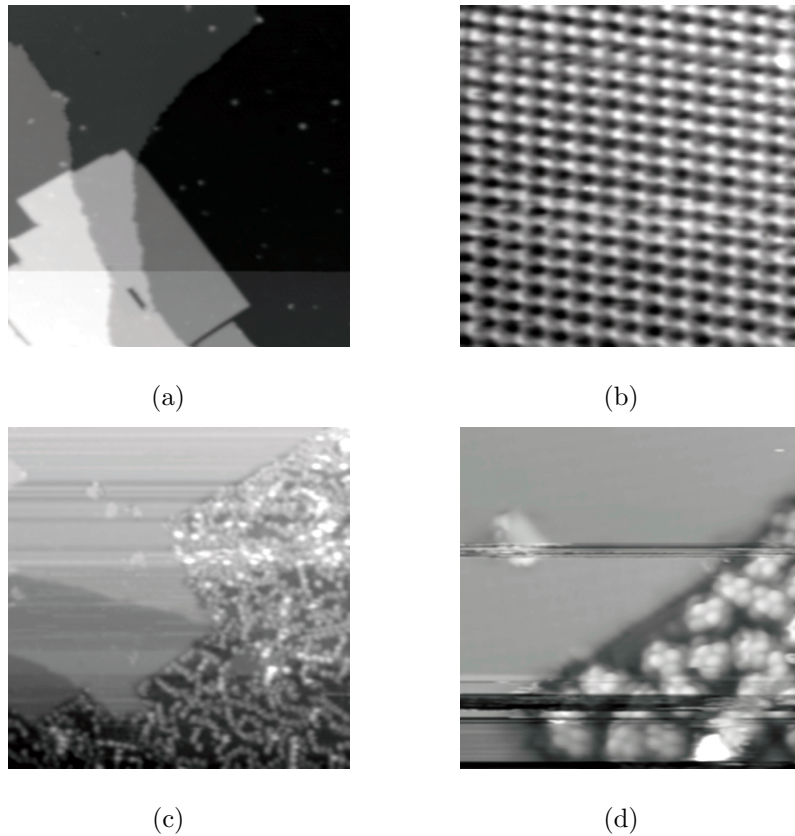


**Figure 4.9:** (a) NaCl island on Cu(100), image size  $86 \times 86 \text{ nm}^2$ . Defects are due to residual impurities in the NaCl powder (early stage of cleaning). FILE: 3D10T006.IMG. (b) Atomic resolution on a NaCl island due to molecular amplification (see text), image size  $5.7 \times 5.7 \text{ nm}^2$ . FILE: 3D11T009.IMG. (c),(d) Surface after adsorption of lander molecules, image sizes  $129 \times 129 \text{ nm}^2$  and  $14 \times 14 \text{ nm}^2$ , respectively. NaCl islands apparently remain free of molecules. FILE: 3D11T013.IMG & 3D11T018.IMG.

molecules, the NaCl surface does not seem to be a suitable substrate for lander molecular assembly.

## 4.2 Lander on Other Substrates

### 4.2.1 Lander on $\text{Cu}_3\text{Au}(100)$

In Section 4.1.1, we conclude that on Cu(100), the lander molecule adsorbs with the central board parallel to the step, preventing good electronic coupling between the

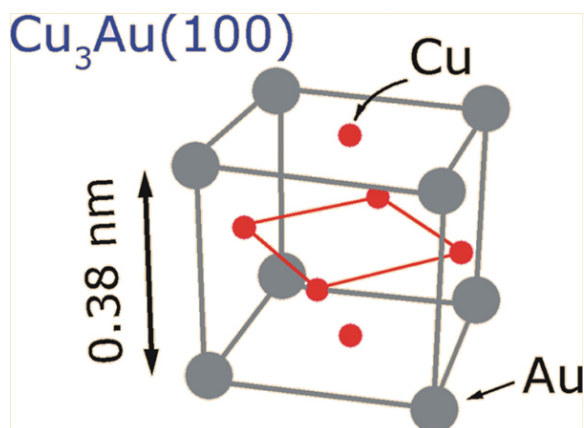


**Figure 4.10:** The crystal structure of Cu<sub>3</sub>Au. This alloy has an ordered structure made up of an alternating stacking Cu planes and of CuAu planes with a lattice constant of 3.75 Å.

wire's end groups and the step. The single step height of Cu(100) is 0.18 nm and the distance from the central board to the surface is 0.37 nm, it is too large for a good overlap between the wire's and metal's electronic wavefunction. In early work of lander adsorbed on Cu(100) it was asserted that electronic coupling is achieved on double steps of this substrate. Since the height of double atomic steps of Cu(100) ( $\sim 0.36$  nm) ideally matches the height from the central board to the flat terrace of Cu(100) ( $\sim 0.37$  nm), one may conclude that this geometrical feature is an essential property for good overlap of the electronic wavefunction of the molecular wire and of the metallic step edge. However, the extreme low density of double steps of Cu(100) substrate has limited further observation of such a coupling. Hence experimental evidence is too scarce to allow definitive conclusion.

To overcome this problem, we employed an alloy substrate Cu<sub>3</sub>Au(100). The crystal structure of Cu<sub>3</sub>Au is shown in Figure 4.10. This alloy has an ordered structure made up of an alternating stacking of Cu planes and of CuAu planes with a lattice constant of 3.75 Å. After an adequate preparation, the Cu<sub>3</sub>Au(100) surface yields single step of 0.18 nm and double steps of 0.37 nm which perfectly matches the wire height on Cu(100) and should favour the electronic coupling of lander to double step edge.

After sublimation of lander on Cu<sub>3</sub>Au(100) substrate at submonolayer coverage,

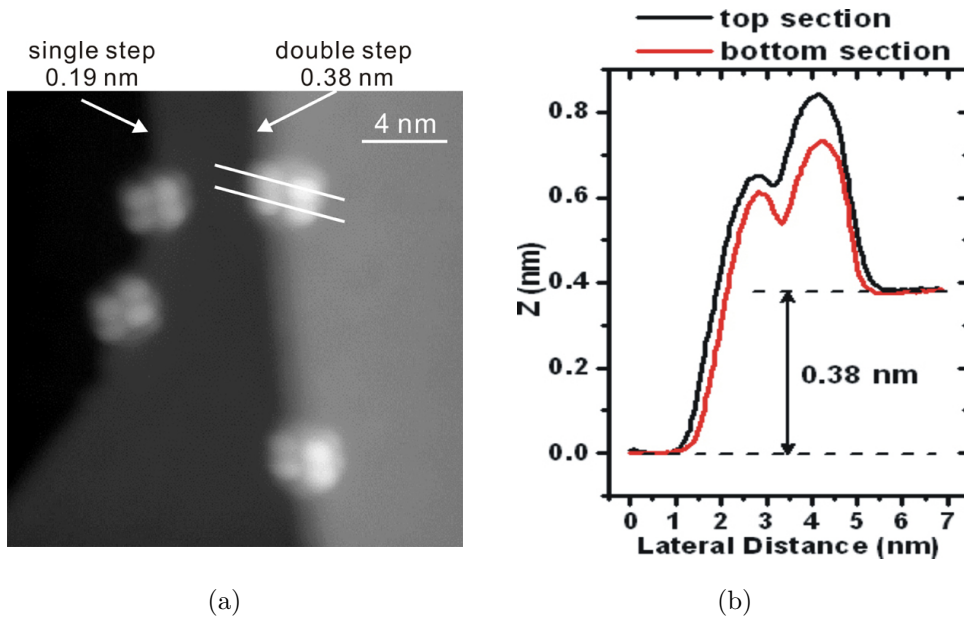


**Figure 4.11:** (a) Lander molecules adsorbed on the single step edge and double step edges of Cu<sub>3</sub>Au(100). ( $I_t = 1$  nA,  $V_s = 300$  mV, scan size =  $20 \times 20$  nm<sup>2</sup>, FILE: 1J10T005.IMG). (b) Cross-sections of landers adsorbed on the double step edges of Cu<sub>3</sub>Au(100).

high resolution STM images were routinely acquired. Figure 4.11(a) shows lander molecules adsorbed at single and double steps of Cu<sub>3</sub>Au(100) substrate. The adsorption geometry of lander at steps of both heights closely resembles the one on single step of Cu(100): two DTP legs are on the top terrace and the other two on bottom terrace for both single and double steps. The cross-section profiles [see Figure 4.11(b)] of molecules at both steps of Cu<sub>3</sub>Au(100) are similar to that of lander at single step of Cu(100). This resemblance points to the central board parallel to the steps edge of Cu<sub>3</sub>Au(100) and hence an absence of good electronic coupling between molecular wire and the step edge. Meantime it is also found that it's easier to diffuse for lander on Cu<sub>3</sub>Au(100) than on Cu(100) which suggests a weaker interaction between molecule and Cu<sub>3</sub>Au(100) substrate compared to Cu(100). So if the matching of the wire height with the step height is indeed a crucial parameter for establishing good electronic coupling, this could explain the absence of electronic coupling of lander to double step edges of Cu<sub>3</sub>Au(100).

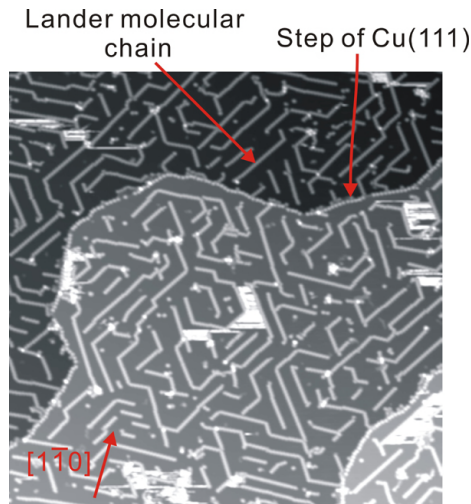


**Figure 4.12:** Lander molecules adsorbed on Cu(111). The steps are completely decorated and excess molecules form molecular chains about 10 ~ 50 nm long along  $[11\bar{2}]$ ,  $[1\bar{2}1]$  and  $[\bar{2}11]$  directions on the terraces. The orientation of  $[1\bar{1}0]$  is indicated by arrow. The white scratches are due to the fact that the tip drags the lander molecule during scanning. ( $I_t = 0.05$  nA,  $V_s = 1000$  mV, scan size =  $207 \times 233$  nm<sup>2</sup>, FILE: 3E28T008.IMG).

### 4.2.2 Lander on Cu(111)

Figure 4.12 shows an STM image of lander molecules adsorbed on Cu(111) surface at submonolayer coverage. Lander molecules arrange themselves in molecular chains about 10 ~ 50 nm long on Cu(111) surface. The chains align along three distinct directions which are  $120^\circ$  between each other. To determine the directions of the molecular chains, we also intentionally made tip-sample contact to produce straight atomic steps of the closed-packed  $\langle 1\bar{1}0 \rangle$  directions of Cu(111) which is indicated by arrow in Figure 4.12. The chains are found to be perpendicular to these high-symmetry directions. Thus the lander molecular chains aligning along  $[11\bar{2}]$ ,  $[1\bar{2}1]$  and  $[\bar{2}11]$  directions can be concluded.

Close inspection of the images reveals that some molecular chains are made of two different chains which are formed with two parallel mirror symmetrical molecules (see Figure 4.13), namely the “right-hand” molecular chain and “left-hand” molecular chain [The “right-hand” and “left-hand” molecules are defined as follows: the long axis (see Figure 4.6) should be rotated anti-clockwise to match the direction of the



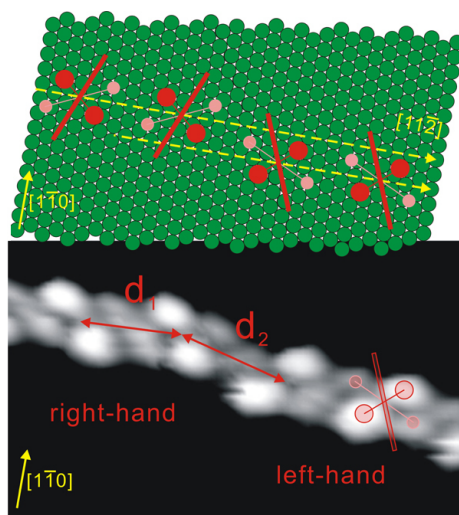


**Figure 4.13:** Close view of the structure with the connection of “right-hand” and “left-hand” molecular chains and corresponding overlayer registry. The molecule in the chain is clear as a four-lobe pattern.  $d_1$  and  $d_2$  are the distances defined in the text. The model is rotated to match the crystallographic orientation of the experimental image. The arrows indicate the crystallographic orientation and molecular chains orientation. The small and big red circles represent the dim and bright lobes of lander molecule. And the slim red rectangle represents the wire board. Solid green circles represent the copper atoms on Cu(111) substrate.

short axis via sharp angle corresponds the “left-hand” molecule, while via blunt angle corresponds the “right-hand” molecule.]. This finding is consistent with previous observation of lander on Cu(100) that only molecules of like symmetry align in the same chain.

To seek the model of the lander molecular arrangements on Cu(111), we have measured the distance ( $d_1$ ) between molecular centers in a row ( $1.67 \pm 0.2$ ) nm which is  $\sim 7\%$  larger than that on Cu(100) surface, the distance ( $d_2$ ) between the centers of “right-hand” molecular chain and “left-hand” molecular chain at the connection ( $1.82 \pm 0.2$ ) nm (cf. Figure 4.13). Figure 4.13 also shows a structural model. Lander molecules are assumed to be adsorbed on the top site of Cu(111), so that the DTP legs are adsorbed on the hollow site of Cu(111) [91]. This model gives the “right-hand” and “left-hand” molecular chains align along  $[11\bar{2}]$ ,  $[1\bar{2}1]$  and  $[\bar{2}11]$  directions.

The distance between molecular centers in a row of 1.76 nm and between the centers of two handed molecular chain at connection of 1.84 nm can also be extracted from this model. They also agree well with the experimental data within the estimated uncertainties. From the model one can conclude that the central boards of the lander molecules do not connect to each other when there is lander adsorbed on Cu(111).

In summary, on Cu(111), we have observed at low coverage two different enantiomerically pure lander molecular rows assembling by two mirror symmetry molecules connect into supramolecular chains about 10 ~ 50 nm long. The molecular chains align along  $[11\bar{2}]$ ,  $[1\bar{2}1]$  and  $[\bar{2}11]$  directions. We have proposed a model of lander adsorbed on Cu(111) surface which agrees well with the experimental data. The model shows that the central boards are not connected to each other when lander molecules are adsorbed on Cu(111) surface.

### 4.2.3 Lander on Au(788)

Vicinal surfaces are natural templates for growing nanostructured solids with low-dimensional properties [92–95]. Au(788) is vicinal with respect to Au(111) by a miscut angle of  $3.5^\circ$  towards  $[\bar{2}11]$  and presents  $\{111\}$ -like steps. Most of Au(111) vicinals undergo faceting [96], but Au(788) is a stable orientation.

Figure 4.14 shows an STM image of a Au(788) surface on a large scale. At the bottom right, the insert shows a  $dI/dV$  map zoom in a few terraces which enhances the discommensuration lines running perpendicular to the step edges. This indicates the characteristic reconstruction of alternating fcc- and hcp-packed domains within the same terrace is similar to the reconstruction of Au(111). The broad dark stripes correspond to fcc domains, the smaller ones to hcp domains [97]. The average terrace width value of Au(788) is  $(39 \pm 4)$  Å and the periodic fcc-hcp reconstruction distance is  $(72 \pm 2)$  Å. The different atoms of these two sites reflects the low energy of Au atoms on fcc sites [98].

The reconstructed Au(788) surface offers inequivalent adsorption sites (fcc domains, hcp domains and bridge sites) and preferred interaction of lander molecule with specific sites may be expected. Figure 4.15 shows the STM picture of lander

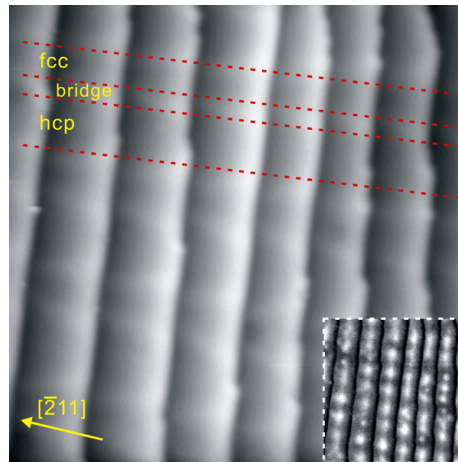


**Figure 4.14:** STM image of Au(788) showing straight monatomic steps. The insert is the  $dI/dV$  map of Au(788) which shows the detailed structure. Bright and dark areas indicate the presence of alternating fcc- and hcp-packed domains within the same terrace. ( $I_t = 0.3$  nA,  $V_s = -600$  mV, scan size =  $30 \times 30$  nm<sup>2</sup>, FILE: 3I03T022.IMG).

molecules adsorbed on Au(788) substrate at low coverage. The lander molecules are adsorbed along step edges. The steps are not uniformly decorated with lander molecules, rather the Au(788) reconstruction determines sites of preferential adsorption at steps. Step segments which intersect fcc domains are decorated with lander molecules while segments which intersect hcp domain are uncovered except a few molecules which indicated by arrows in Figure 4.15. The bridge sites are depleted of molecules. Because the experiments were performed under low temperature and thermodynamic growth condition, the distribution of lander onto the inequivalent adsorption sites of the reconstructed Au(788) surface can be directly interpreted in terms of the local molecule-substrate interaction. Lander molecule is most strongly bound to the step segments which intersect fcc domains. This suggests that the molecule-substrate interaction is larger within fcc domains than in hcp domains and the weakest on bridge sites.

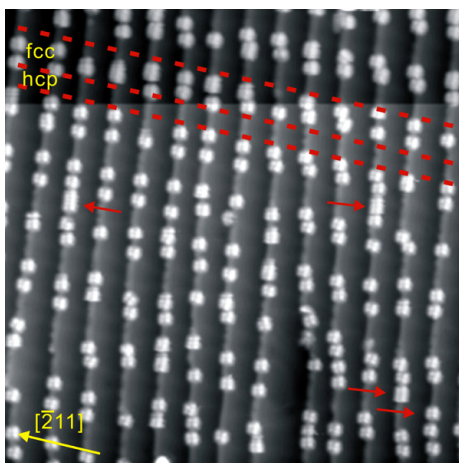


**Figure 4.15:** Lander molecules adsorbed on Au(788). Landers prefer to adsorb on the step edges which intersect with fcc domains while only a few molecules which indicated by arrows adsorb on hcp domains. ( $I_t = 0.01$  nA,  $V_s = 1600$  mV, scan size =  $60 \times 60$  nm<sup>2</sup>, FILE: 3I04T003.IMG)

### 4.3 STS of Lander on Different Metal Substrates

A very important surface tool with STM is spatially resolved spectroscopy. Current-voltage ( $I - V$ ) curves are recorded at different points on a molecule to determine the more electronically transparent region of a molecule. This helps in understanding STM images. This is also a formidable tool when lander molecule is connected at one end to a step edge and the tip apex of the STM positioned as a second ultra clean electrode at the other end of the molecular wire. In our experiments, all spectra were acquired under conditions of 5 mV (rms) modulation and 10 kHz frequency and 1 ms time constant in the lock-in. The tunneling spectra on a bare terrace of the substrates provide a solid reference to check the status of the STM tip, allowing to perform reliable spectra and to discard tip artifacts affecting the lander spectra. All the raw data of the spectra were treated as following: the acquired  $I(V)$  curve was numerically differentiated to determine the zero point and maxima of the corresponding  $dI/dV$  curve acquired from the lock-in.

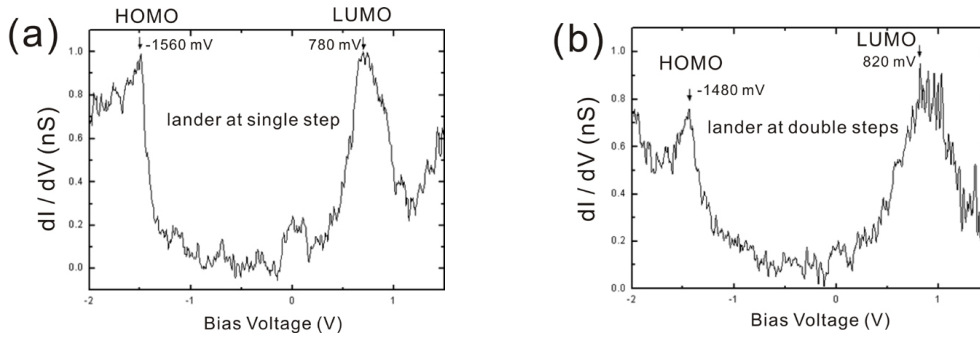


**Figure 4.16:** (a) The tunneling spectra ( $dI/dV$ ) of lander on single step of  $\text{Cu}_3\text{Au}(100)$ . (b)  $dI/dV$  spectra of lander on double steps of  $\text{Cu}_3\text{Au}(100)$ . The sample voltage was set to 1 V before cutting the feedback loop.

### 4.3.1 STS of lander on $\text{Cu}_3\text{Au}(100)$

The  $\text{Cu}_3\text{Au}(100)$  substrate is ideal for STS on the lander molecules adsorbed at single and double steps. As shown in Figure 4.16, both spectra exhibit a gaped region, estimated at  $\sim 2.3$  eV. No difference is evidenced in the spectra of lander molecules adsorbed at single and double steps.

The gap between two peaks marked in the spectra is actually extremely close to the HOMO-LUMO gap of the lander in the gas phase (2.3 eV), suggesting a nearly zero molecular orbitals mixing between the board part of lander and the  $\text{Cu}_3\text{Au}(100)$  substrate. This viewpoint may be consistent with the absence of an electronic coupling of lander with the double step edges of  $\text{Cu}_3\text{Au}(100)$ , since if the lander molecule is less deformed by the substrate it must yield a wire height close to the gas phase height of  $\sim 0.7$  nm and may therefore not be suited to electronically couple to  $\text{Cu}_3\text{Au}(100)$  double steps of  $\sim 0.37$  nm. No significant change is evidenced in the spectra for set point currents ranging from 0.1 nA to 10 nA.

We also performed spatially resolved spectroscopy over various positions of lander. In Figure 4.17, we present the typical spectra recorded over five different parts of a lander on a single step of  $\text{Cu}_3\text{Au}(100)$ : the center of lander and the four DTP-legs which appear as four bright lobes in the STM images. The spectra show little spatial dependency over the lander. Since the 2.3 eV gap is inconsistent with the high-energy gap expected for DTP-legs, all the spectra are dominated by the molec-

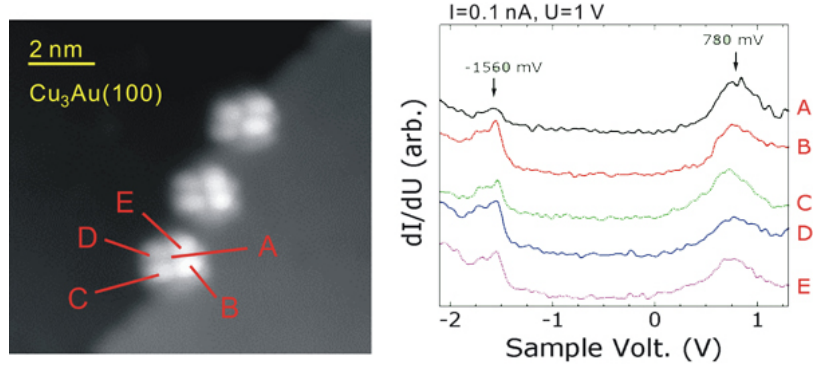


**Figure 4.17:** Spatially resolved spectra of a lander on a single step of  $\text{Cu}_3\text{Au}(100)$  (image size  $12 \times 12 \text{ nm}^2$ ). The spectra shown are shifted for clarity and were acquired at 0.1 nA with a sample voltage set to 1 V before cutting the feedback loop.

ular wire wavefunction. This means that there is a substantial leakage of the wire's wavefunction over the four DTP-legs. This is also proved by the investigation of the standing wave patterns of lander molecules [99]. However, when comparing spatially resolved spectra over various lander molecules we note that there is a random variation in the height of the left peak flanking the gap, suggesting a dependence of this peak's intensity on the lander orientation with respect to the atomic step.

### 4.3.2 Comparison of lander STS on different metal surfaces

This section will make a comparison of the STS of lander on different metal substrates. Since the spectra show little spatial dependency over lander molecule, we concentrate on the spectra on the center of lander. Figure 4.18 shows the spectra of lander on the step edge of  $\text{Ag}(111)$ ,  $\text{Cu}(111)$  and  $\text{Au}(111)$ . The spectra of lander on  $\text{Ag}(111)$  is noisier than that on  $\text{Cu}(111)$  and  $\text{Au}(111)$  is due to the fact that we use less averaging times during the experiment on  $\text{Ag}(111)$ .

Similar to that on  $\text{Cu}_3\text{Au}(100)$ , all the spectra exhibit a gaped region. Compared with  $\text{Cu}_3\text{Au}(100)$  (2.3 eV), the gaps in spectra are considerably larger on  $\text{Ag}(111)$  ( $2.9 \pm 0.1 \text{ eV}$ ),  $\text{Cu}(111)$  ( $2.7 \pm 0.1 \text{ eV}$ ) and  $\text{Au}(111)$  ( $2.8 \pm 0.1 \text{ eV}$ ).

To understand the differences between the  $dI/dV$  spectra of lander at the step of Ag, Cu, Au and  $\text{Cu}_3\text{Au}$  substrates, the work function differences between these

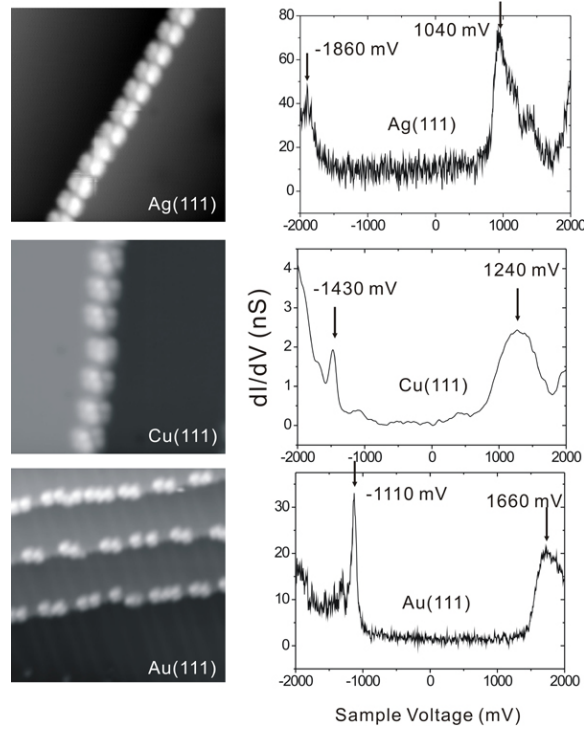


**Figure 4.18:** STS of center lander molecules adsorbed on the step edge of Ag(111) (image size  $18 \times 18 \text{ nm}^2$ ), Cu(111) (image size  $14 \times 14 \text{ nm}^2$ ) and Au(111) (image size  $38 \times 38 \text{ nm}^2$ ), respectively. The spectra shown were acquired at 0.1 nA with sample voltage set to 1 V before cutting the feedback loop.

substrates are first considered. Since lander molecules are most likely to be in the physisorbed regime, work function differences can be expected to play an important role in determining molecular properties. The work function values of  $\text{Cu}_3\text{Au}(100)$ , Ag(111), Cu(111) and Au(111) are 4.48 eV, 4.74 eV, 4.94 eV and 5.31 eV, respectively [48]. If we assume that the electron affinity of lander is not strongly changed by adsorption to these substrates, we expect the LUMO state for lander to locate at the energy above  $E_F$  which equals to the substrate's work function subtracted by the electron affinity [100,101]. From Figure 4.16 and Figure 4.18, we can extract the lander LUMO states increase from  $(0.78 \pm 0.15) \text{ V}$  for  $\text{Cu}_3\text{Au}(100)$  to  $(1.04 \pm 0.20) \text{ V}$ ,  $(1.24 \pm 0.15) \text{ V}$  and  $(1.66 \pm 0.10) \text{ V}$  for Ag(111), Cu(111) and Au(111), respectively. Thus lander LUMO states are experimentally 0.26 V, 0.46 V and 0.88 V higher for Ag(111), Cu(111) and Au(111) than for  $\text{Cu}_3\text{Au}(100)$ . These values coincide with the

work function differences between Ag(111) (0.26 eV), Cu(111) (0.46 eV), Au(111) (0.83 eV) and Cu<sub>3</sub>Au(100). This provides a rough explanation as to why the lander LUMO states are experimentally shifted to higher energy relative to  $E_F$  with bigger work function. The electron affinity of lander can be calculated to be 3.7 eV.

The lander HOMO states are experimentally located at  $(-1.56 \pm 0.15)$  V,  $(-1.86 \pm 0.05)$  V,  $(-1.43 \pm 0.05)$  V and  $(-1.11 \pm 0.05)$  V for Cu<sub>3</sub>Au(100), Ag(111), Cu(111) and Au(111), respectively. The substrates work function differences are not adequate to explain the different HOMO states in the  $dI/dV$  spectra for these substrates. The HOMO-LUMO gap observed experimentally, however, may arise from the differences in lander charging energies for these molecule/substrate systems. The HOMO-LUMO gap seen by tunneling can be found to be expressed as [102]:

$$\Delta E_{\text{gap}} = \varepsilon_{\text{LUMO}} - \varepsilon_{\text{HOMO}} + U$$

where  $\Delta E_{\text{gap}}$  is the HOMO-LUMO gap in the  $dI/dV$  spectra,  $\varepsilon_{\text{LUMO}}$  and  $\varepsilon_{\text{HOMO}}$  are the LUMO and HOMO states of molecule,  $U$  is the charging energy arising from Coulomb repulsion between electrons.

The difference  $\varepsilon_{\text{LUMO}} - \varepsilon_{\text{HOMO}}$  has been found to be 2.3 eV for lander in gas phase [103] which is extremely close to the HOMO-LUMO gap in the spectra of lander on Cu<sub>3</sub>Au(100). Assuming that the presence of the surface does not significantly change  $\varepsilon_{\text{LUMO}} - \varepsilon_{\text{HOMO}}$  [104], the value of lander adsorbate charging energy can be found by subtracting 2.3 eV from the experimentally measured HOMO-LUMO gaps. This procedure leads to almost the same  $U$  value of  $(0.5 \pm 0.1)$  eV for lander at the step of Ag(111), Cu(111) and Au(111), and of course, zero charging energy for Cu<sub>3</sub>Au(100). The difference in lander charging energies that we observe for noble (111) and Cu<sub>3</sub>Au(100) substrate is attributed to the screening behavior induced by noble (111) substrates [102] and the weak influence of Cu<sub>3</sub>Au(100) surface on lander molecule properties.

In this section, we have found an increase of the LUMO states for lander on Cu<sub>3</sub>Au(100), Ag(111), Cu(111) and Au(111). This is due to the work function differences between these substrates. We also observe a HOMO-LUMO gap increase of 0.5 eV for lander molecule on noble (111) substrates compared with Cu<sub>3</sub>Au(100).



This difference is explained as the result of increasing charging energy due to the screening behavior for lander on noble (111) substrates.

The results of the conformations and chiral structures of lander molecules adsorbed on Cu(100) were published in Ref. [73] and [85].



## Chapter 5

# Cobalt Phthalocyanine on Cu(111)

The use of individual molecules as functional electronic devices was first proposed in the 1970s by Aviram and Ratner [62]. Since then, molecular electronics, one of the major fields in nanoscience, involving the exploration of the electronic level structure, response and transport, together with the development and applications of electronic devices at molecular scale, has attracted much interest. Its major application areas include sensors, displays, smart materials, molecular motors, molecular scale transistors, logic and memory devices [105–111].

Metal(II) phthalocyanines (MPc) are square planar complexes with great technological and fundamental interest because of their own properties and their similarity to other classes of compounds. A schematic structure of a typical MPc is presented in Figure 5.1. The phthalocyanines are extensively used as pigments and dyes, and they are models for biologically important species such as porphyrins, hemoglobin, and chlorophyll. They can serve as the active elements in chemical sensors, especially for the detection of NO<sub>2</sub> [112, 113]. They have interesting semiconductivity and can be used to form well-behaved field effect transistors [114, 115]. Their catalytic properties have been studied for some time [116], especially for redox catalysis such as in fuel cell applications [117–119]. They are of great interest for use in optoelectronic devices [120] and solar cells [121].

Theoretical studies of the electronic structure of MPc including density functional treatments (DFT) [122–124], unrestricted (open-shell) Hartree–Fock

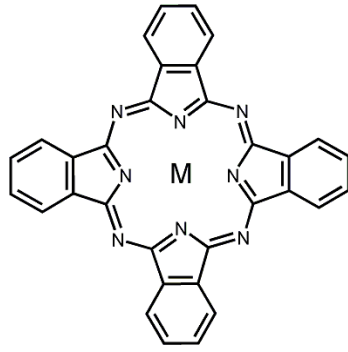


**Figure 5.1:** Molecular structure of a typical MPc.

calculations [125], multiconfiguration self-consistent field (SCF) calculations [126], and extended Hückel MO based ESQC calculations [74] have been made.

An understanding of the interaction between MPc and surfaces is a critical element required for optimizing their use in the applications listed above. This can be addressed by obtaining submolecularly resolved images of MPc adsorbed on the substrate of interest. Until now, however, only limited information about the nature of the adsorbed MPc was extracted by STM studies.

Actually phthalocyanines were among the first organic molecules to be studied by STM. STM images of individually distinguishable copper phthalocyanine (CuPc) molecules have been presented by a number of researchers. Gimzewski and co-workers studied CuPc adsorbed on polycrystalline silver [127]. Lippel *et al.* observed excellent submolecular resolution images of CuPc adsorbed on Cu(100) [11]. Moeller and associates reported single molecule of CuPc on GaAs(110) [128]. Ludwig *et al.* found highly resolved images of CuPc can be obtained on graphite and MoS<sub>2</sub> [129]. Fritz *et al.* studied hetero-epitaxial layers of CuPc on Au(111) [130], as did Petracek [131]. Kanai and co-workers studied CuPc on Si(100) and Si(111) [132]. The transition from three-dimensional to two-dimensional faceting of Ag(110) induced by CuPc was found by Böhringer and associates [71]. The electron transport through CuPc molecule on NiAl(110) was studied by Nazin *et al.* [133]. In addition, images of the free acid (H<sub>2</sub>Pc) co-adsorbed on graphite with a liquid crystalline carrier have also been published by Freund and associates [134]. There have been reports of STM study of PbPc by Pester *et al.* [135] and Hamann *et al.* [136]. Gopakumar investigated the

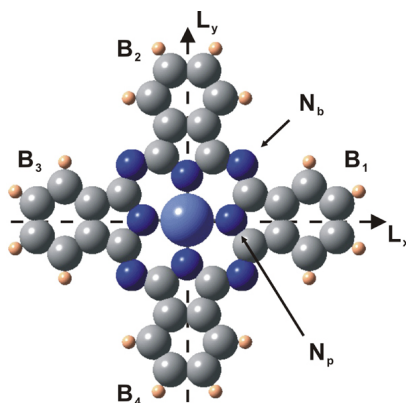


**Figure 5.2:** Structure of CoPc. Two axes orthogonal to each other are assigned  $L_x$  and  $L_y$ , and four benzene rings as  $B_1$ - $B_4$ .  $N_b$  and  $N_p$  are the bridge nitrogen atom and pyrrolic nitrogen atom, respectively. Light blue sphere: cobalt atom. Deep blue spheres: nitrogen atoms. Grey spheres: carbon atoms. Pink spheres: hydrogen atoms.

adsorption property of PdPc on graphite [137]. The adsorption and two-dimensional phases of chloro[subphthalocyaninato]boron(III) (SubPc) on Ag(111) was found by Berner and associates [138]. Self-assembly of CuPc and ZnPc on pyrolytic graphite were observed by Qiu and co-workers [139]. Stöhr *et al.* studied the co-adsorption of CuPc and  $C_{60}$  on Au(111) [140], as well as Fendrich *et al.* [141]. Hipps and co-workers distinguished CuPc and CoPc on Au(111) in STM images [142,143]. Recently, Zhao *et al.* observed Kondo effect of CoPc on Au(111) after cutting the hydrogen atoms from the molecule by STM tip [144]. Takada *et al.* reported adsorbed CoPc molecules on Au(111) and Cu(100) [145–147].

In this chapter, the investigation of CoPc molecules adsorbed on Cu(111) surface by LTSTM will be presented.

Figure 5.2 shows the geometric structure of the CoPc. The length between the central cobalt atom and the pyrrolic nitrogen atom ( $N_p$ ) is  $1.92 \text{ \AA}$  and the distance between cobalt atom and the bridge nitrogen atom ( $N_b$ ) is  $3.36 \text{ \AA}$ . The two molecular axes orthogonal to each other are assigned as  $L_x$  and  $L_y$ , and four benzene rings as  $B_1$ - $B_4$ .  $L_x$  and  $L_y$  are treated equivalently. In CoPc an excess of negative charge is found on the eight electronegative nitrogen atoms [ $N_p$  (atomic charges  $Q = -0.50$ ) and  $N_b$  ( $Q = -0.33$ )] which surround the cobalt atom. The negative charge is compensated

by the eight most central carbon atoms ( $Q = +0.32$ ). All the numbers given above are adopted from Ref. [124].

The Cu(111) surface was prepared using standard procedure in the preparation chamber. CoPc (Aldrich [148],  $\geq 97.0\%$ ) was heated at  $200^\circ\text{C}$  for 24 hours to remove the impurity with high vapor pressure and then deposited onto the Cu(111) surface which was kept at room temperature from the molecule evaporator monitored by a quartz balance in the preparation chamber (cf. Section 3.3.2). The sample was transferred into the STM chamber and cooled down to 4.7 K. Tungsten tips were used for STM observation.

## 5.1 Coverage Dependent Supramolecular Structures of CoPc

The bonding and ordering of molecules on surfaces are generally controlled by a subtle balance between the competing molecule-molecule and molecule-substrate interactions. For supramolecular self-assembly, three kinds of noncovalent interactions are usually believed to be the most important molecule-molecule interactions: dipole-dipole [149], metal-ligand [150], and hydrogen bonding interactions [88,151,152]. The metal surface is often considered as a static checkerboard that provides bonds and specific adsorption sites to the molecules [153–156].

We find a coverage-dependent evolution for CoPc supramolecular structures on Cu(111) with a range of coverages from submonolayers to more than 1 ML. We attribute this dependence to the delicate balance between local molecule-molecule interactions and molecule-substrate interactions.

### 5.1.1 Low coverage

Figure 5.3(a) shows a constant current topography of CoPc on Cu(111) at low coverage ( $\Theta \approx 0.3$  ML). Single CoPc molecules are visible and the molecular diameter is  $(16.8 \pm 2.0)$  Å in agreement with the molecular dimensions in the gas phase (around

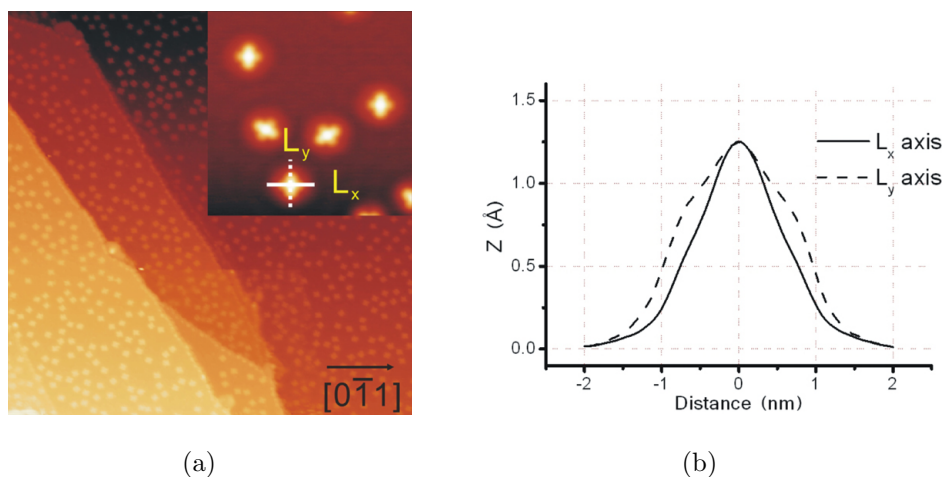


**Figure 5.3:** (a) STM image of CoPc molecules on Cu(111) surface at low coverage. Insert shows individual CoPc molecules, solid lines indicate the  $L_x$  axis, broken lines indicate the  $L_y$  axis. ( $I_t = 0.1$  nA,  $V_s = -600$  mV, scan size =  $110 \times 120$  nm<sup>2</sup>, FILE: 5K13T009.IMG). (b) Line profiles along  $L_x$  axis (solid line) and  $L_y$  axis (broken line).

15.0 Å). This confirms the expected planar adsorption of CoPc. The apparent height of CoPc molecules in the STM images is  $(1.60 \pm 0.15)$  Å.

A closer inspection of the STM images reveals an internal molecular structure with high resolution as shown in the insert of Figure 5.3(a). The CoPc molecules are easily identified. The phthalocyanine ring appears like a four-lobe pattern and in the center the cobalt atom appears as a bright (high) spot, as reported by Hipps *et al.* [142, 143]. The protrusion in the center is due to the  $3d$  orbital of cobalt. The axis of CoPc ( $L_x$ ) [as indicated by the solid lines in the insert of Figure 5.3(a)] orients parallel to the closed-packed  $\langle 1\bar{1}0 \rangle$  directions of Cu(111) surface. This preferential orientation of molecular axis obviously reveals that molecule-substrate interactions determine the adsorption geometry of CoPc on Cu(111) at low coverage.

Note that although  $L_x$  and  $L_y$  are equivalent in gas phase, they appear different in the STM image. From the line profiles along  $L_x$  and  $L_y$  axes [Fig 5.3(b)],  $L_y$  is higher and longer than  $L_x$  in STM image. We attribute this geometric difference to the registry of CoPc on Cu(111) surface. Figure 5.4 presents a possible real space structural model of single CoPc adsorbed on Cu(111). In this model, all nitrogen atoms are located on the top of copper atoms.  $L_x$  and  $L_y$  axes are not equivalent

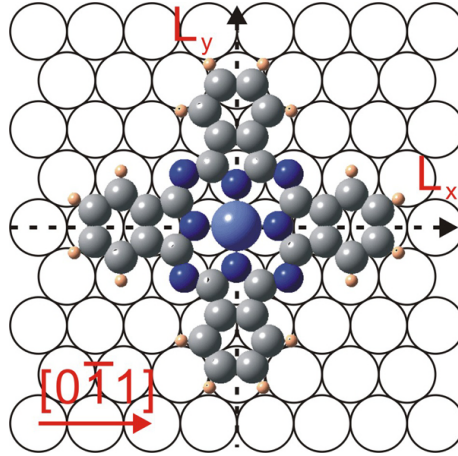


**Figure 5.4:** Possible real space structural model for single CoPc adsorbed on Cu(111). Open circles indicate the copper atoms on Cu(111) surface.

with respect to the Cu(111) substrate since the benzene rings in the  $L_x$  and  $L_y$  axes are located on the bridge site and the three-fold hollow site on Cu(111), respectively.

Another visible feature in Figure 5.3(a) is that no dimers, chains, islands or ordered domains are found at this coverage. This feature is different with CuPc on Ag(110) in which CuPc molecules aggregating into dimer and trimer and short chains at coverage of 0.3 ML was found [71]. This suggests that molecule-substrate interactions dominate the adsorption of CoPc on Cu(111) while attractive molecule-molecule forces basically seem to be absent at low coverage. And the interaction between CoPc and copper substrate is stronger than that between CuPc and silver substrate because silver surface is more inert.

### 5.1.2 High coverage

Upon further CoPc deposition to a coverage of 0.6 ML, the first ordered structure of CoPc (chain phase) appears. In this phase, CoPc molecules are connected into chains orienting nearly along  $\langle 1\bar{1}0 \rangle$  directions. A second ordered phase of CoPc (trimer phase) appears once the CoPc coverage approaches  $\approx 0.8$  ML. In trimer phase, three CoPc molecules first organize into trimer that further assemble into hexagonal structures. When the coverage increases to 1 ML, a saturated phase (square phase)



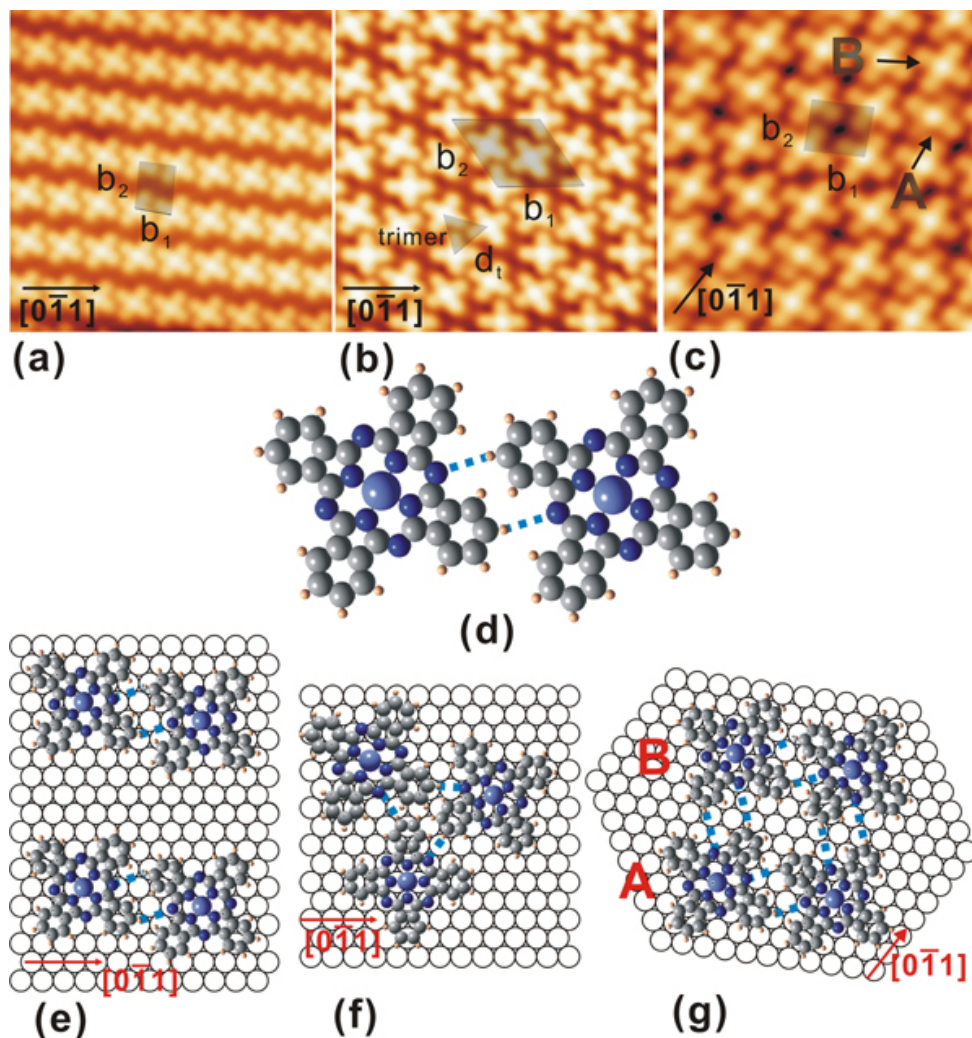


**Figure 5.5:** (a)–(c) STM images of three kinds of supramolecular structures of CoPc molecules adsorbed on Cu(111) at high coverage, namely chain, trimer, and square phase, respectively. The arrows indicate the  $[1\bar{1}0]$  direction of Cu(111). Shaded areas are the unit cells for each supramolecular structures.  $(\mathbf{b}_1, \mathbf{b}_2)$  is the set of primitive vectors.  $d_t$  is the intermolecular distance in the trimer. [Scan condition:  $I_t = 0.1$  nA,  $V_s = -600$  mV, Scan size: (a)  $13 \times 15$  nm<sup>2</sup>, 5J10T028.IMG, (b)  $11 \times 12$  nm<sup>2</sup>, 5J10T039.IMG, (c)  $8 \times 9$  nm<sup>2</sup>, 6C05T015.IMG] (d) Schematic of the formation of hydrogen bonding (dashed blue line) between two neighboring CoPc molecules. (e)–(g) Proposed packing structural models of the adsorbed CoPc supramolecular structures on Cu(111). Copper atoms are indicated as open circles. Molecules “A” and “B” show different contrast between axes in STM images.

Structures	Chain phase	Trimer phase	Square phase
$b_1$ (Å)	$14.5 \pm 0.5$	$28.8 \pm 0.3$	$15.0 \pm 0.5$
$b_2$ (Å)	$20.9 \pm 1.2$	$28.8 \pm 0.3$	$14.5 \pm 0.5$
$\theta$	$(100 \pm 2)^\circ$	$(120 \pm 2)^\circ$	$(90 \pm 2)^\circ$

**Table 5.1:** Primitive vector parameters of the adsorbed CoPc supramolecular structures on Cu(111).  $b_1$  and  $b_2$  are the primitive vectors lengths,  $\theta$  is the angle between the primitive vectors.

appears. The CoPc molecules aggregate into square mesh on the Cu(111) surface.

Molecularly resolved STM images of these three different supramolecular structures are shown in Figure 5.5(a)–(c).

The large-scale supramolecular assembly is due to the balance of molecule-molecule and molecule-substrate interactions. We attribute the molecule-molecule interaction to hydrogen bonding. According to the effective atomic charges calculation of CoPc molecule, an excess of negative charge is found on the eight electronegative nitrogen atoms ( $N_p$  and  $N_b$ ) which surround the cobalt atom [124]. If the coverage is high enough to force  $N_b$  atom and the hydrogen atom of neighboring molecule very close, the formation of hydrogen bond can be achieved [Figure 5.5(d)].

In order to investigate the adsorption geometry for the observed structures, it is instructive to consider possible model of the adsorbate structure. However, it was not possible to simultaneously image the atomic resolution of the Cu(111) substrate together with the molecular resolution of the CoPc molecules which would allow us to determine directly the exact adsorption registry. Nevertheless, the experimental data available together with symmetry arguments allow us to propose a feasible model. To seek the structural model of these ordered structures, several parameters are measured in the STM images. They are shown in Table 5.1.  $\mathbf{b}_1$  and  $\mathbf{b}_2$  in Figure 5.5(a) are the primitive vectors of chain phase, and they are  $(14.5 \pm 0.5)$  Å and  $(20.9 \pm 1.2)$  Å, respectively. In Figure 5.5(b), the distance( $d_t$ ) between two molecules in the trimer is  $(14.5 \pm 0.2)$  Å. Four trimers form a unit cell for this supramolecular structure,  $\mathbf{b}_1$  and  $\mathbf{b}_2$  are the primitive vectors in trimer phase. They are both  $(28.8 \pm 0.3)$  Å.

Structures	Chain phase	Trimer phase	Square phase
Matrix	$\begin{pmatrix} 1 & 6 \\ -1 & -5 \end{pmatrix}$	$\begin{pmatrix} 11 & 0 \\ 0 & 11 \end{pmatrix}$	$\begin{pmatrix} 3.5 & -3.5 \\ -5.5 & 5.5 \end{pmatrix}$
Packing Density	0.31 molecules/nm <sup>2</sup>	0.36 molecules/nm <sup>2</sup>	0.47 molecules/nm <sup>2</sup>

**Table 5.2:** Structural parameters of the proposed models for adsorbed CoPc supramolecular structures with respect to Cu(111)

Figure 5.5(c) gives the primitive vectors  $\mathbf{b}_1$  and  $\mathbf{b}_2$  of the square phase. They are  $(15.0 \pm 0.5 \text{ \AA})$  and  $(14.0 \pm 0.5 \text{ \AA})$ , respectively.

Based upon the STM data, the molecular packing model for the chain phase was proposed in Figure 5.5(e). CoPc molecules form hydrogen bonds running along the  $[\bar{1}\bar{5}6]$  direction of Cu(111). From this proposed model, the matrix notation of  $(1 \ 6, -1 \ -5)$  for the chain phase can be made. In Figure 5.5(f) a molecular packing model for the trimer phase was proposed. Three hydrogen bonds dominate the formation of the trimer. Three molecules in one trimer are twisted  $0^\circ$ ,  $30^\circ$  and  $-30^\circ$  with respect to  $[0\bar{1}1]$  direction, respectively. From this proposed model, we obtain the matrix notation of  $(11 \ 0, 0 \ 11)$  for the trimer phase. Figure 5.5(g) gives a molecular packing model for the square phase. In one unit cell, four CoPc molecules form a square with eight hydrogen bonds. The matrix notation of the square phase is  $(3.5 \ -3.5, -5.5 \ 5.5)$ . Simple rotations of  $\pm 120^\circ$  of the above phases give the remaining six possible configurations. All these configurations are observed in experiments. The structural parameters of the proposed models for these ordered phases are summarized in Table 5.2.

The STM images of individual CoPc molecule in the supramolecular structures show different contrast. In the chain phase, all the molecules show same contrast on both axis. In the trimer phase, the molecule with  $L_x$  axis parallel to  $[0\bar{1}1]$  direction show unequal contrast between  $L_x$  and  $L_y$  axis, while the other two show the same contrast. In the square phase, the molecule marked as “A” shows a dim axis and a bright axis while the molecule “B” shows same axes. This difference can be explained by the adsorption sites with respect to Cu(111) surface. According to the packing

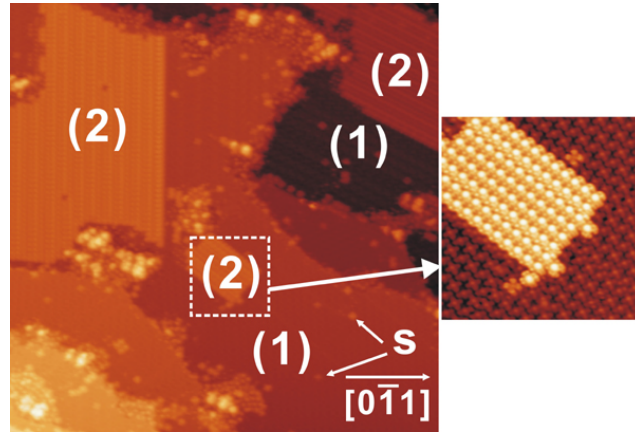


**Figure 5.6:** STM image of CoPc molecules adsorbed on Cu(111) surface at  $\Theta > 1$  ML. Single CoPc molecule, the first and second layer of CoPc molecules are indicated as (s), (1) and (2), respectively. A zoom in the dashed rectangle is shown in the insert. ( $I_t = 0.1$  nA,  $V_s = +1000$  mV, scan size =  $106 \times 122$  nm<sup>2</sup>, FILE: 5J25T067.IMG)

structural model, the molecule showing same contrast is adsorbed on the unsymmetrical site, and the molecule showing different contrast is located on the symmetrical site (bridge site).

### 5.1.3 Coverage $> 1$ ML

Figure 5.6 shows a STM image of CoPc films on Cu(111) substrate at coverage  $\Theta > 1$  ML. The regions marked with (1), (2) and (s) correspond to the first, second layers of CoPc molecules on the substrate and isolated CoPc molecule on first layer, respectively. The monatomic steps of the underlying Cu surface are clearly visible. From the image we can find that CoPc molecules in the second layer aggregate into islands. The edges of the island run along the direction perpendicular to  $[0\bar{1}1]$ . This can be understood that the interaction between the substrate and the second layer molecules is decoupled by the first monolayer, thus the molecule-molecule interaction dominates the adsorption geometry of second layer and the influence of the substrate is negligible.

In this section, we have found the coverage-dependent phase evolution of CoPc adsorbed on Cu(111). At low coverage ( $\Theta \leq 0.3$  ML), dominating of molecule-substrate

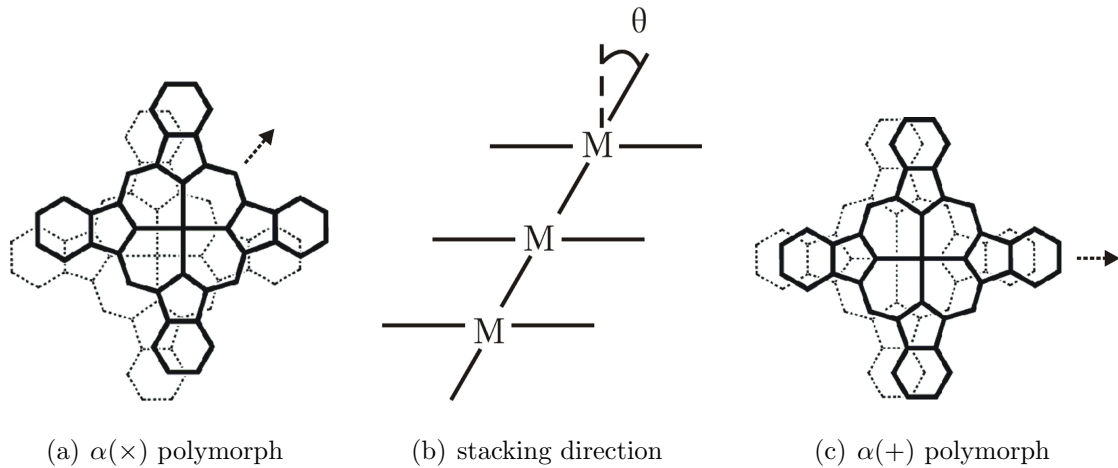


**Figure 5.7:** (a) Molecular stacking of the  $\alpha(\times)$  polymorph of MPc films. (b) Stacking direction of the  $\alpha$  polymorph. (c) Molecular stacking of the  $\alpha(+)$  polymorph.

interaction leads to a sparse adsorption geometry, no dimer, chain, island or other ordered domains can be found. When coverage increases high enough ( $\Theta \geq 0.6$  ML) so that adjacent molecules are very close, the combination of molecule-substrate interaction and molecule-molecule interaction (hydrogen bonding) determines the adsorption geometry. We have found chain and trimer phases. Square phase will appear if the coverage is saturated to 1 ML. When the coverage exceeds 1 ML, in the second layer, the molecule-molecule interaction dominates the adsorption geometry because of the decoupling of molecule-substrate interaction by the first CoPc monolayer, thus the second layer molecules aggregate into islands at this coverage.

## 5.2 Stacking Pattern of CoPc

There are two well-known polymorphs in MPc crystals. One is called  $\alpha$ -type which has been believed, since the report by Ashida *et al.* [157], that undoped molecules are stacked along the  $L_x + L_y$  direction (see Figure 5.2). The stacking pattern is shown in Figure 5.7(a) which the neighboring rings are slipped and the angle ( $\theta$ ) formed between the molecular symmetry axis and the stacking direction [Figure 5.7(b)] ranges in MPc's from  $\sim 26^\circ$  to  $\sim 45^\circ$ , depending on their polymorphic form. On the basis of transmission electron diffraction studies, Hoshimo *et al.* [158] have recently proposed

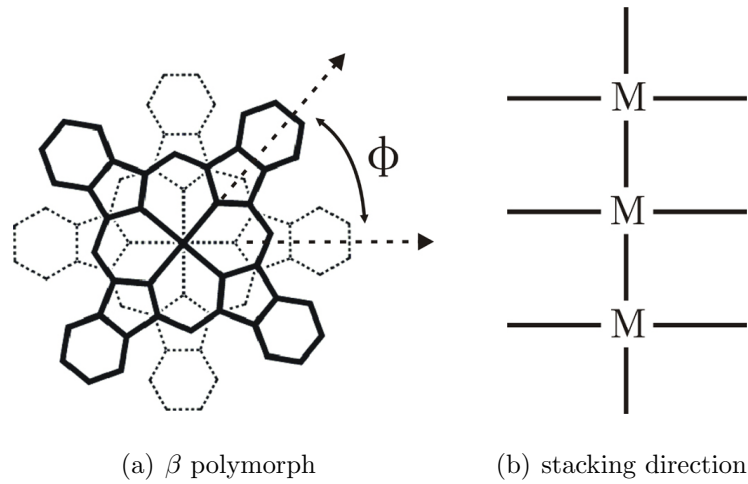


**Figure 5.8:** (a) Molecular stacking of the  $\beta$  polymorph of MPc films. (b) Stacking direction of the  $\beta$  polymorph.

that molecules are stacked along the direction of  $L_x$ , as shown in Figure 5.7(c). They called this new polymorph  $\alpha(+)$ , while that in Figure 5.7(a) is called  $\alpha(\times)$ . The doped compounds are stacked instead in the form of metal-over-metal columnar stacks [Figure 5.8(a)], which is called  $\beta$ -type. As shown in Figure 5.8(b), successive rings in the stacks assume a conformation with a rotation angle between two  $L_x$  axes  $\phi \sim 40^\circ$  [159].

Submolecularly resolved STM images of double layers of CoPc molecules on Cu(111) give us direct information about the stacking property of CoPc molecules. Figure 5.9 shows an STM image recorded at sample voltage of  $-1.0$  V, in which both the first and second layers are observed. From Figure 5.9(a), we can see that first layer molecules under the second layer have the same orientation with the second layer molecules. Figure 5.9(b) is a cross section of the broken line A-B in Figure 5.9(a). The central Co atoms in the second layer, as indicated by arrows, are observed to be brighter than surroundings. The spacing between the arrows is equal  $(13.8 \pm 0.2)$  Å, indicating that the CoPc molecules in the second adsorb in the same pattern as first layer. Figure 5.9(c) is a cross section of the broken line C-D along  $L_x$  axis of the molecule in the second layer in Figure 5.9(a). The benzene ring labeled in the figure as  $B_1$  (see Figure 5.2) is found to be higher than that labeled  $B_3$ . Although the topography gives the information of LDOS of the sample and can not be directly in-

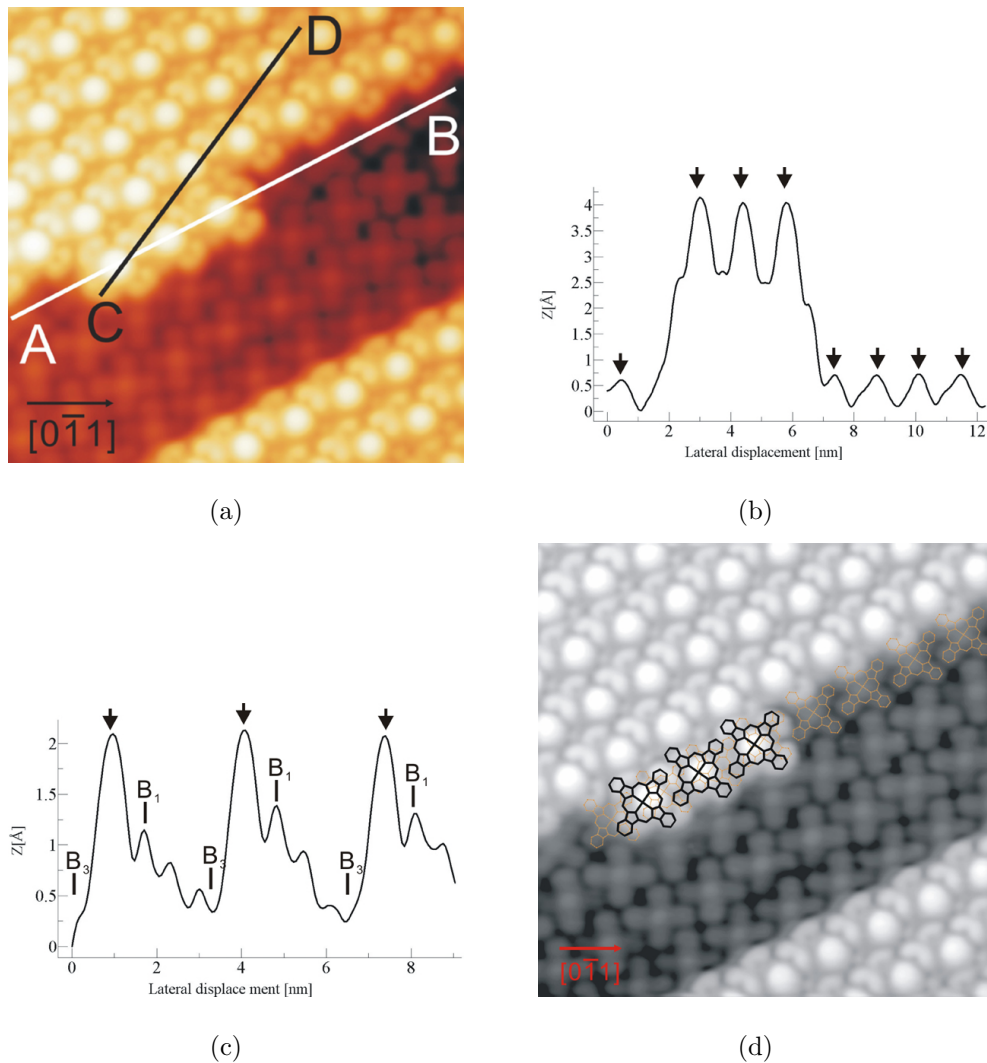


**Figure 5.9:** (a) STM image of the first and second layers of CoPc molecules on Cu(111) surface. ( $I_t = 0.1$  nA,  $V_s = -500$  mV, scan size =  $10.6 \times 12.2$  nm<sup>2</sup>, FILE: 5J27T013.IMG) (b) Line profile along the line A – B in (a). Arrows indicate the positions of Co atoms. (c) Line profile along the line C – D in (a).  $B_1$  and  $B_3$  indicate benzene rings. Arrows indicate the positions of Co atoms. (d) Stacking of the second layer of CoPc molecules.

terpreted into the real vertical height of the molecule, however, this apparent height difference is independent of the sample bias voltage and since the electronic structures of  $B_1$  and  $B_3$  are equal to each other, this apparent height difference can be regarded as the real height difference between  $B_1$  and  $B_3$ . The molecules are likely to be inclined with respect to the substrate surface. The average tilt angle from the surface plane is  $(3.0 \pm 0.4)^\circ$ . With high resolution of the STM images, we can identify

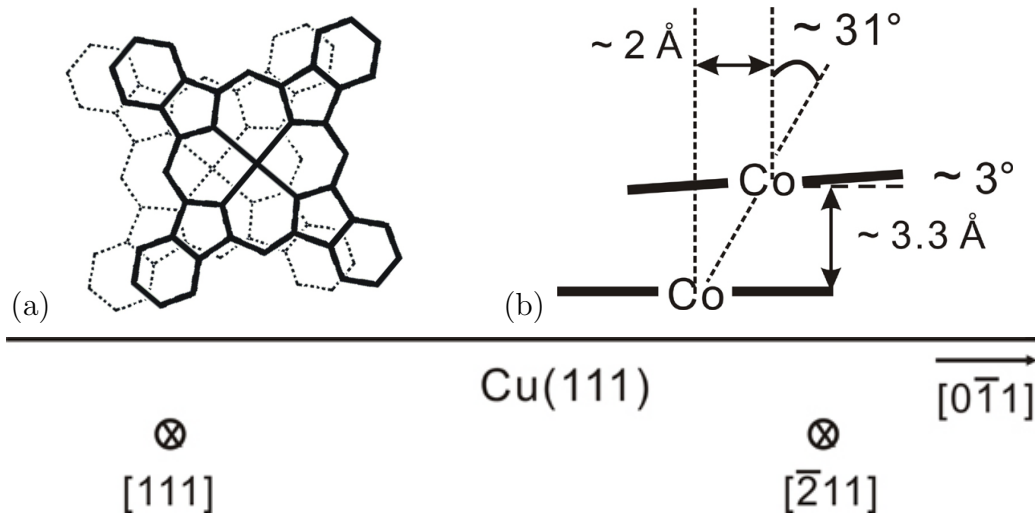


**Figure 5.10:** Possible model for CoPc molecular stacking on Cu(111) surface. (a) Projection in the  $[111]$  direction. (b) Projection in the  $[\bar{2}11]$  direction.

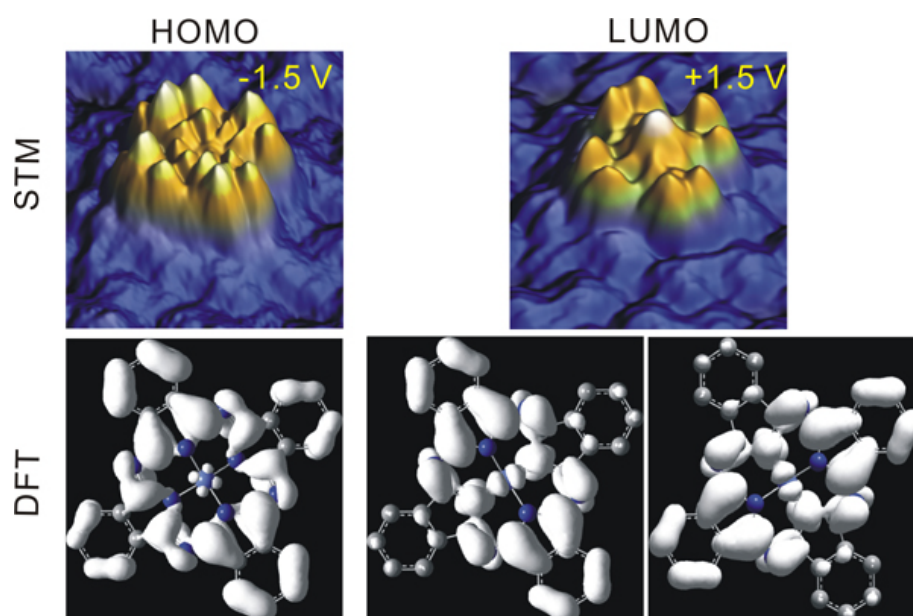
the stacking type of CoPc molecules on Cu(111). Figure 5.9(d) shows the molecular structure model mapping on Figure 5.9(a). It is clear from this mapping that the CoPc molecules are stacked with  $\alpha(\times)$  type. The lateral distance between the central Co atoms of the first and second layers is  $\sim 2 \text{ \AA}$ , and the apparent vertical height between the first and second layer is  $\sim 3.3 \text{ \AA}$ . From these results, we can get the stacking angle  $\theta$  is  $\sim 31^\circ$ .

Figure 5.10 shows a possible model for molecular stacking of CoPc bilayer films on Cu(111) based on the discussion above. The view of Figure 5.10(a) is projected in the  $[111]$  direction. The molecules are stacked with  $\alpha(\times)$  type. Figure 5.10(b) is projected in the  $[\bar{2}11]$  direction. CoPc molecules of the second layer are tilted along the  $[0\bar{1}1]$  direction of Cu(111).

### 5.3 Adsorption-site Dependent STM Images

Individual CoPc molecules in the second layer have fine structures [cf. Figure 5.9(a)]. The benzene rings are divided into two parts, and porphyrin rings are clearly recognized. In contrast to the low resolution of single CoPc molecule directly adsorbed on Cu(111), the spatial resolution can be much enhanced by imaging an isolated CoPc





**Figure 5.11:** Top: STM images of isolated CoPc on the first layer acquired at  $V_s = -1.5$  V and  $V_s = +1.5$  V. ( $I_t = 0.1$  nA, scan size =  $4.7 \times 5.4$  nm<sup>2</sup>, FILE: 5J28T011.IMG & 5J28T012.IMG). Bottom: Calculated HOMO (left) and degenerate LUMOs (right) of free CoPc molecule using Gaussian03 with DFT (B3LYP/6-31G\*).

molecule on the first layer of CoPc molecules. The top row of Figure 5.11 shows typical STM images of an isolated CoPc molecule on the first layer acquired at sample bias voltages of -1.5 V and +1.5 V. The benzene rings and porphyrin rings are clearly visible. The central Co atom shows as a depression at negative bias, while as a protrusion at positive bias. These two STM images very closely resemble the native HOMO and LUMO of the free molecule in gas phase, which are calculated using Gaussian03 [160] with DFT (B3LYP/6-31G\*) by the group of Prof. R. Herges in University Kiel and shown in the bottom row of Figure 5.11.

When a molecule is adsorbed onto a metal surface, its molecular orbitals are not only influenced and broadened by a direct coupling to the electronic states of the substrate, but there is also an electronic coupling of different molecular states through the surface [161, 162]. This effect usually results in a strong distortion of the molecular states, thus there is hardly any resemblance to the native orbitals of free molecule in gas phase. However, adsorbed on CoPc molecular monolayer, the isolated

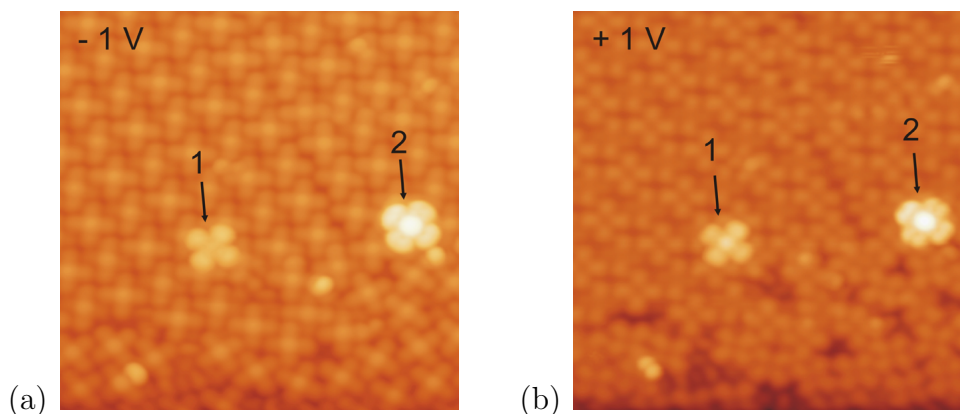


**Figure 5.12:** STM images of two identical CoPc molecules on the first layer. Molecule 1 shows HOMO-LUMO feature at  $V_s = -1$  V and  $V_s = +1$  V, while molecule 2 doesn't. ( $I_t = 0.1$  nA, scan size =  $13.8 \times 15.9$  nm<sup>2</sup>, FILE: 6C09T021.IMG & 6C09T022.img)

CoPc molecule has to interact with the metal surface through CoPc layer. The direct correspondence between the experimental STM images and the molecular orbitals of the free molecule clearly demonstrates that the electronic decoupling provided by the CoPc layer is sufficient to preserve the inherent electronic properties of the free molecule. This situation is similar to pentacene on NaCl films [27].

Apart from the isolated molecules which show MO-like STM images, there are also some isolated molecules do not change significantly in STM images with different bias. Figure 5.12 shows two identical molecules which appear different images under negative and positive sample bias voltages. The left molecule (molecule 1) shows HOMO-like topography at negative bias [Figure 5.12(a)] and LUMO-like topography at positive bias, while the right molecule (molecule 2) does not change [Figure 5.12(b)].

By mapping the positions of these two molecules to the monolayer underneath, we find that the center of molecule 1 is on the middle of the square lattice formed by four molecules beneath and we call this position “on hollow site”. While the center of molecule 2 is almost on the top of the center of the molecule beneath and we call this position “on top site”. This adsorption geometry is schematically shown in Figure 5.13. One could guess that the images of second layer molecules depend on their adsorption sites with respect to the CoPc molecules beneath.

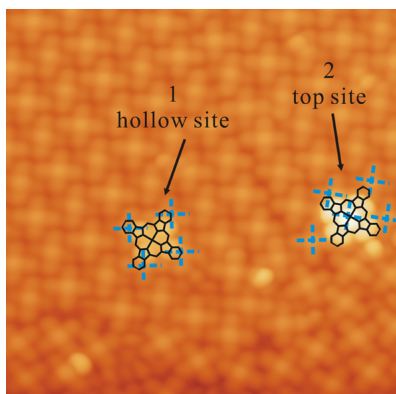


**Figure 5.13:** Different adsorption sites of molecule 1 (on hollow site) and molecule 2 (on top site). The black molecular structures indicate the isolated CoPc molecules and the blue crosses indicate the molecules beneath.

This effect may be due to the axial interactions of the CoPc molecules. When the second layer molecule is on the top site, there are interactions between the second-layer CoPc molecule and CoPc beneath, thus it is less electronically decoupled from the substrate than that on the hollow site, because those molecules adsorbed on hollow sites are lifted by four benzene rings beneath. That is the reason why the MOs of CoPc in gas phase can be highly resolved by STM in the molecules adsorbed on hollow sites, while those molecules on top sites do not.

We intentionally manipulated the molecule on the hollow site to the top site using STM tip ( $I_t = 1$  nA,  $V_s = 0.5$  V). The results are shown in Figure 5.14. Before manipulation, the two molecules in the left column of Figure 5.14 are both on hollow sites, thus show MO-features at negative and positive bias. After manipulating the right molecule from hollow site to top site as shown in the right column of Figure 5.14, this molecule loses its HOMO and LUMO-features while the other one still shows MO-features at different bias. Another phenomena to note is that at positive sample bias, the center of the molecule at top site appears brighter than that at hollow site. During manipulation, we found that it is much easier to manipulate CoPc molecule from hollow site to top site than *vice versa*. This implies the top site is energetically more stable than hollow site. All these phenomenons strongly support the fact that there are strong interactions in CoPc dimer of the two layers. Due to the interactions,

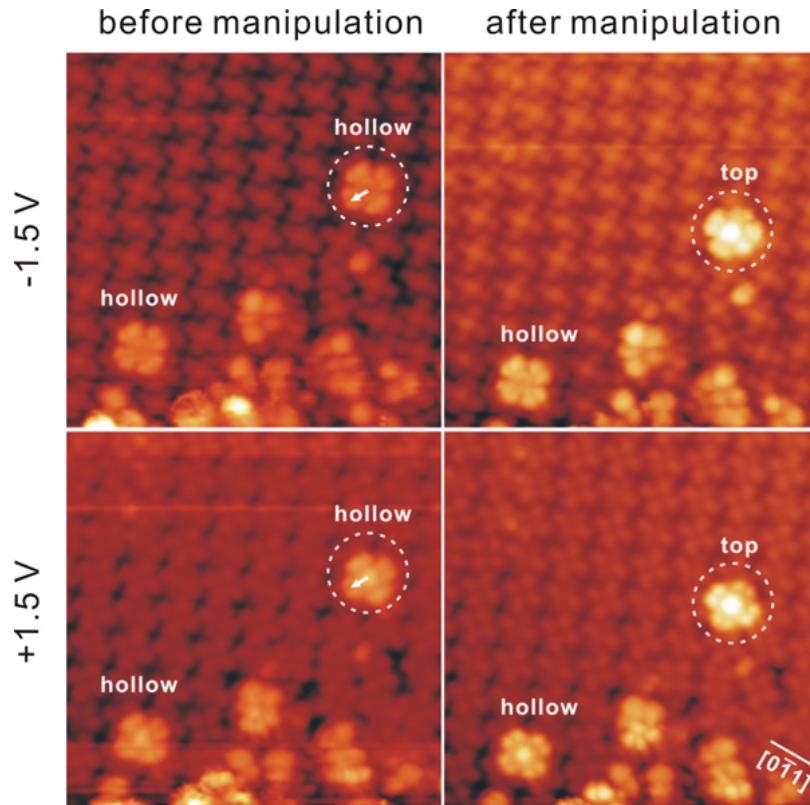


**Figure 5.14:** Manipulation of CoPc molecules on the first layer. Left: Before manipulation, both molecules are on hollow sites and show HOMO-LUMO feature at  $V_s = -1.5$  V and  $V_s = +1.5$  V. Right: After manipulating the right molecule from hollow site to top site, this molecule does not show HOMO-LUMO feature at  $V_s = -1.5$  V and  $V_s = +1.5$  V, while the other remaining on hollow site still shows. ( $I_t = 0.1$  nA, scan size =  $12.5 \times 14.4$  nm<sup>2</sup>, FILE: 6F21T007.IMG – 6F21T010.IMG)

all CoPc molecules in the islands of the second layer adsorb onto the top sites of the first monolayer.

One may guess the interactions may be due to the Co-Co bonding, since for MPc dimers, Ru=Ru [163, 164], Os=Os [165], Mo-Mo [166], Rh-Rh [167, 168], Ir-Ir [169], Re≡Re [170] and In-In [171] bondings have been reported. However, detailed analysis of the STM images reveals that the on-top STM images is not exactly “on-top” position, there is a lateral distance between the cobalt atoms in the second-layer and first-layer CoPc molecules about  $(2 \pm 0.5)$  Å. This distance is long enough to prevent a Co-Co bonding forming. Until now, we have no explanation for the interactions and need further theoretical calculation.

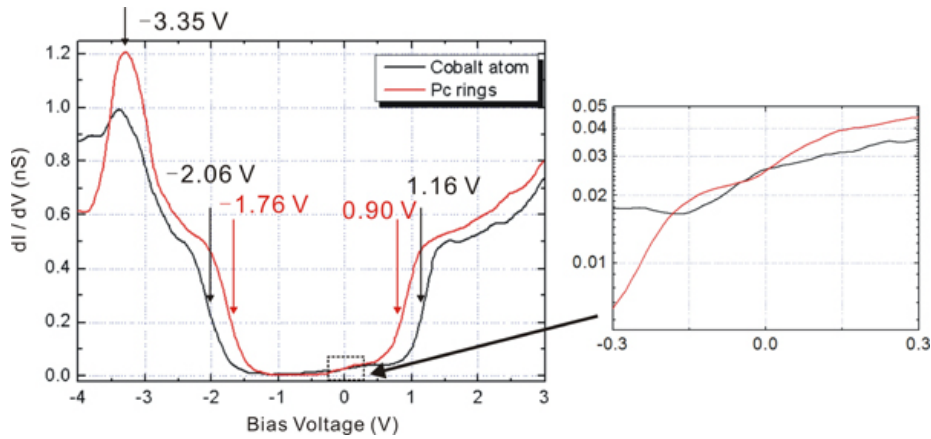


**Figure 5.15:**  $dI/dV$  spectra of CoPc on Cu(111). Black line: acquired on cobalt atom. Red line: acquired on Pc rings. Arrows indicate the positions of peaks and steps in the spectra. Insert is the zoom in the spectra of energy near  $E_F$ . (The y axis of the insert is in log scale.)

In conclusion, by investigating the adsorption of CoPc molecules on Cu(111) substrate with STM, we found remarkable change of images. The image of CoPc molecule directly adsorbed on Cu(111) surface has lowest resolution which only shows a four-lobe pattern. The image of second layer molecule on top site of first layer shows more resolution. And the second layer molecule on hollow site amidst four first layer molecules has highest resolution which can represent the HOMO, LUMO-features at negative and positive bias. These could be explained as to the electronic coupling between the molecule and substrate since the electronic coupling strength is the strongest when the molecule is directly adsorbed on surface, the weakest when it is located on hollow site because it is almost completely decoupled from the substrate by the four benzene rings beneath, and stronger when it is on top site because of the interactions in the dimer of two CoPc molecules.

## 5.4 STS of CoPc on Cu(111)

Electronic properties of the CoPc molecule on Cu(111) are probed with STS. All spectra were acquired under  $f_{mod} = 10$  kHz,  $V_{rms} = 10$  mV, and time constant =

3 ms conditions of lock-in. The raw data of the spectra were treated as the STS of lander molecules (cf. chapter 4). The results of the measurements are presented in Figure 5.15(a), where  $dI/dV$  spectra taken at cobalt atom is given in black curve and  $dI/dV$  spectra taken at phthalocyanine macrocycle is given in red curve. Both positive-bias and negative-bias, corresponding to unoccupied and occupied states of the sample, are presented. The  $dI/dV$  spectra show a peak and a wide gap. In the center of the CoPc molecule, the peak is located at  $(3.35 \pm 0.10)$  eV below  $E_F$  with a gap between  $(-2.06 \pm 0.30)$  V and  $(+1.16 \pm 0.30)$  V. At the periphery of the molecule, the spectra show a peak with lower intensity at  $(3.35 \pm 0.15)$  eV below  $E_F$  and a narrower gap between  $(-1.76 \pm 0.30)$  V and  $(+0.90 \pm 0.30)$  V. The spectra obtained for the clean Cu(111) surface do not show these features.

The  $dI/dV$  spectra can be interpreted in terms of orbital mediated tunneling [100,172]. Figure 5.16 illustrates the energies of the upper occupied and lower vacant MOs for the ground states of CoPc in gas phase [124] using DFT method. The orbitals are labeled according to the irreducible representation of  $D_{4h}$ . The Co-3d populations of some MOs are reported in parentheses.

The strongest peak in the spectra is the peak at -3.35 V. This is the basis for interpreting our  $dI/dV$  results in terms of MOs of CoPc. Since the intensity of this peak in the spectra on Pcs is larger than that on cobalt atom, the orbital should be predominated by Pc rings rather than the metal. And because the step at negative bias should be assigned around HOMO, the energy difference between HOMO and this orbital must be less than 2.5 V. Thus the peak at 3.35 eV below  $E_F$  should be related to  $a_{2u}$  which is located predominantly on the Pc rings. For clarity, we can convert the orbital energy values of CoPc in vacuum level to the energy level relative to  $E_F$  by adding 3.12 eV [ $-3.35 - (-6.47)$ ]. The results are shown in Table 5.3.

The step at -1.8 V in the spectra on Pc rings may be assigned to the HOMO ( $a_{1u}$ , -1.88 eV), and the step at -2.06 V in the spectra on cobalt atom must be due to the HOMO+1 ( $a_{1g}$ , -2.01 eV) because this orbital is dominated by Co-3d<sub>z<sup>2</sup></sub> (88%). The  $b_{2g}$  (-2.64 eV) is in the background of the spectra. The LUMO ( $2e_g$ ) is difficult to assign because it is at 0.17 eV, and no peaks and steps are distinguishable in the

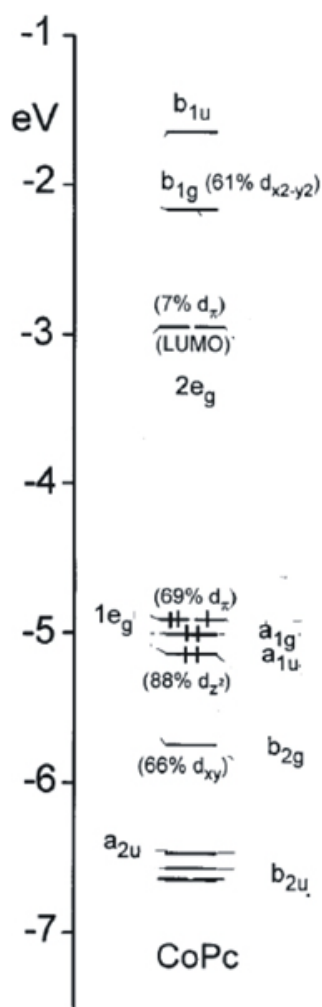


**Figure 5.16:** Orbital energy levels for the outer orbitals in CoPc. After M. S. Liao Ref. [124].

orbital energy levels	vacuum level (eV) <sup>a</sup>	relative to $E_F$ (eV)
$b_{1u}$	-1.64	1.48
$b_{1g}$	-2.17	0.95
$2e_g$ (LUMO)	-2.95	0.17
$1e_g$	-4.91	-1.79
$a_{1u}$ (HOMO)	-5.00	-1.88
$a_{1g}$	-5.13	-2.01
$b_{2g}$	-5.76	-2.64
$a_{2u}$	-6.47	-3.35
$b_{2u}$	-6.56	-3.44

**Table 5.3:** Orbital energy values of CoPc in vacuum level and sample bias scale.

<sup>a</sup>Data from Ref. [124]

spectra. However, close inspection reveals there is a slight increase near Fermi-level at positive bias in the spectra (cf. Figure 5.15). We attribute this slight increase to the LUMO, and we have no explanation as to why the  $2e_g$  would be so small. The next steps in  $dI/dV$  are at 0.9 V for the spectra on Pc rings and 1.1 V for the spectra on cobalt atom. These steps can be assigned to the  $b_{1g}$  (0.95 eV). Taking the work function of Cu(111) to be 4.94 eV [48], the electron affinity of CoPc is then  $(4.04 \pm 0.30$  eV) in good agreement with values obtained for other phthalocyanines [101, 173, 174].

An assumption for this assignment is that the CoPc molecule is undisturbed by the substrate when adsorbed on Cu(111) because we relate the  $dI/dV$  features to the MOs of CoPc in gas phase. However, this is not rigidly fulfilled since there are strong molecule-substrate interactions when CoPc adsorbed on Cu(111) which is evident because the molecules can hardly be moved by the tip when imaging even at  $1\mu$  A. To get full understanding of the STS of CoPc adsorbed on Cu(111), a further theoretical calculation accounting for the molecule-substrate interaction is needed. This may explain why the step in the spectra of CoPc on Pc rings is at lower positive bias than that on cobalt atom although they are assigned to the same  $b_{1g}$  orbital.



# Chapter 6

## Conclusion

In this thesis the adsorption of organic molecules on metal substrates is studied by a home-made STM at low temperature (4.7 K) in UHV. Some of the most relevant achievements accomplished are summarized as follows:

In the first part, based on submolecularly resolved STM images, it is possible to determine different conformations of lander molecules adsorbed on Cu(100) surface. The experimental findings are in excellent agreement with theoretical prediction by ESQC. A detailed investigation demonstrates that lander adsorbs at the step edge of Cu(100) with its conducting board parallel to the step, preventing good electronic contact between molecule and the step. The same geometry has been found for Cu<sub>3</sub>Au(100) surface even if it yields steps whose height perfectly matches the molecular wire height on terrace. Through the analysis of STM images it is possible to propose models for explaining the chiral structure of lander on Cu(100) and the molecular chains of lander on Cu(111).

Moreover, the study of STS reveals an increase of LUMO states for lander on Cu<sub>3</sub>Au(100), Ag(111), Cu(111) and Au(111) which is due to the fact of work function differences between these substrates. The wider HOMO-LUMO gap in the spectra of lander on noble (111) surfaces compared with Cu<sub>3</sub>Au(100) is explained as the result of increasing charging energy due to the screening behavior for lander on noble (111) substrates.

CoPc adsorbed on Cu(111) are thoroughly investigated in the second part. The

analysis of STM images reveals the adsorption phase change within a range of coverages. This change is the result of delicate balance between local molecule-molecule interaction and molecule-substrate interaction. A detailed examination of submolecular-resolution STM images of double layers of CoPc allows to determine the  $\alpha(\times)$ -type stacking of CoPc. A reasoning based on first principle calculations, semiempirical and molecular dynamics simulations, provides the frame for understanding the origin of adsorption-site-dependent STM images of individual CoPc molecule on CoPc layers. The STS results of CoPc on Cu(111) are assigned to the MOs of CoPc.

# Bibliography

- [1] G. Moore, *Electronics* **38**, 113 (1965).
- [2] G. Bourianoff, *Computer* **36**, 44 (2003).
- [3] M. Lundstrom, *Science* **299**, 210 (2003).
- [4] R. Feynman, *Eng. Sci.* **23**, 22 (1960).
- [5] A. Nitzan and M. A. Ratner, *Science* **300**, 1384 (2003).
- [6] G. Binnig and H. Rohrer, *Helvetica Physica Acta* **55**, 726 (1982).
- [7] G. Binnig, H. Rohrer, C. Gerber, and E. Weibel, *Appl. Phys. Lett.* **40**, 178 (1982).
- [8] R. J. Hamers, R. M. Tromp, and J. E. Demuth, *Phys. Rev. Lett.* **56**, 1972 (1986).
- [9] B. C. Stipe, M. A. Rezaei, and W. Ho, *Science* **280**, 1732 (1998).
- [10] H. Ohtani, R. J. Wilson, S. Chiang, and C. M. Mate, *Phys. Rev. Lett.* **60**, 2398 (1988).
- [11] P. H. Lippel, R. J. Wilson, M. D. Miller, C. Wöll, and S. Chiang, *Phys. Rev. Lett.* **62**, 171 (1989).
- [12] J. A. Stroscio and D. M. Eigler, *Science* **254**, 1319 (1991).
- [13] C. Joachim, J. K. Gimzewski, R. R. Schlittler, and C. Chavy, *Phys. Rev. Lett.* **74**, 2102 (1995).

- 
- [14] S. Datta, W. Tian, S. Hong, R. Reifenger, J. I. Henderson, and C. P. Kubiak, *Phys. Rev. Lett.* **79**, 2530 (1997).
- [15] J. K. Gimzewski and C. Joachim, *Science* **283**, 1683 (1999).
- [16] W. Ho, *J. Chem. Phys.* **117**, 11033 (2002).
- [17] P. Sautet and M.-L. Bocquet, *Phys. Rev. B* **53**, 4910 (1996).
- [18] D. N. Futaba, J. P. Landry, A. Loui, and S. Chiang, *Phys. Rev. B* **65**, 45106 (2002).
- [19] A. J. Fisher and P. E. Blöchl, *Phys. Rev. Lett.* **70**, 3263 (1993).
- [20] F. Biscarini, C. Bustamante, and V. M. Kenkre, *Phys. Rev. B* **51**, 11089 (1995).
- [21] T. A. Jung, R. R. Schlittler, and J. K. Gimzewski, *Nature (London)* **386**, 696 (1997).
- [22] M. Schunack, F. Rosei, Y. Naitoh, P. Jiang, A. Gourdon, E. Laegsgaard, I. Stensgaard, C. Joachim, and F. Besenbacher, *J. Chem. Phys.* **117**, 6259 (2002).
- [23] K. Walzer and M. Hietschold, *Surf. Sci.* **471**, 1 (2001).
- [24] X. H. Qiu, G. V. Nazin, and W. Ho, *Science* **299**, 542 (2003).
- [25] X. H. Qiu, G. V. Nazin, and W. Ho, *Phys. Rev. Lett.* **92**, 206102 (2004).
- [26] Z. C. Dong, X. L. Guo, A. S. Trifonov, P. S. Dorozhkin, K. Miki, K. Kimura, S. Yokoyama, and S. Mashiko, *Phys. Rev. Lett.* **92**, 86801 (2004).
- [27] J. Repp, G. Meyer, S. M. Stojkovic, A. Gourdon, and C. Joachim, *Phys. Rev. Lett.* **94**, 26803 (2005).
- [28] R. Wiesendanger, *Scanning Probe Microscopy and Spectroscopy: Methods and Application* (Cambridge University Press, Cambridge, UK, 1994).
- [29] J. Tersoff and D. R. Hamann, *Phys. Rev. Lett.* **50**, 1998 (1983).

- 
- [30] J. Tersoff and D. R. Hamann, Phys. Rev. B **31**, 805 (1985).
- [31] J. Bardeen, Phys. Rev. Lett. **6**, 557 (1961).
- [32] J. A. Appelbaum and W. F. Brinkman, Phys. Rev. **186**, 464 (1969).
- [33] T. E. Feuchtwang, P. H. Cutler, and N. M. Miskovsky, Phys. Lett. **99A**, 167 (1983).
- [34] A. Selloni, P. Carnevali, E. Tosatti, and C. D. Chen, Phys. Rev. B **31**, 2602 (1985).
- [35] V. A. Ukraintsev, Phys. Rev. B **53**, 11176 (1996).
- [36] G. Binnig and D. P. E. Smith, Rev. Sci. Instrum. **57**, 1688 (1986).
- [37] A. Bryant, D. P. E. Smith, and C. F. Quate, Appl. Phys. Lett. **48**, 832 (1986).
- [38] P. K. Hansma and J. Tersoff, J. Appl. Phys. **61**, R1 (1987).
- [39] W. Shockley, Phys. Rev. **56**, 317 (1939).
- [40] S. D. Kevan and R. H. Gaylord, Phys. Rev. B **36**, 5809 (1987).
- [41] E. W. Plummer and J. B. Hannon, Progr. Surf. Sci **46**, 149 (1994).
- [42] R. Haight, Surf. Sci. Rep. **21**, 275 (1995).
- [43] N. Memmel, Surf. Sci. Rep. **32**, 91 (1998).
- [44] C. Kittel, *Elementary Statistical Physics* (Courier Dover Publications, Mineola, New York, 2004).
- [45] J. Kliewer, Phd thesis, RWTH Aachen, D-52056 Aachen, Germany, 2000.
- [46] J. Kliewer, R. Berndt, E. V. Chulkov, V. M. Silkin, P. M. Echenique, and S. Crampin, Science **288**, 1399 (2000).
- [47] J. Li, Ph.D. thesis, UNIVERSITE DE LAUSANNE FACULTÉ DES SCIENCES, Lausanne, Switzerland, 1997.

- [48] D. R. Lide, *CRC Handbook of Chemistry and Physics : A Ready-reference Book of Chemical and Physical Data, 87<sup>th</sup> edition, 2006-2007* (Taylor & Francis Group, Boca Raton, FL, 2006).
- [49] A. M. Russell and D. A. Torchia, *Rev. Sci. Instrum.* **33**, 442 (1962).
- [50] M. L. Meade, *Lock-in amplifiers: principles and applications* (Peter Peregrinus Ltd., London, UK, 1983).
- [51] The first Virtual Internet Experiment / The Lock-In Amplifier : Exploring Noise Reduction and Phase Sensitive Detection, <http://www.lockin.de/>.
- [52] J. Li, W.-D. Schneider, and R. Berndt, *Phys. Rev. B* **56**, 7656 (1997).
- [53] R. Lazzaroni, A. Calderone, G. Lambin, J. P. Rabe, and L. J. Bredas, *Synth. Met.* **41-43**, 525 (1991).
- [54] N. D. Lang, *Phys. Rev. B* **34**, 5947 (1986).
- [55] S. Lindsay, O. F. Sankey, Y. Li, C. Herbst, and A. Rupprecht, *J. Phys. Chem.* **94**, 4655 (1990).
- [56] K. W. Hipps and U. Mazur, *J. Phys. Chem* **97**, 7803 (1993).
- [57] D. A. Bonnell, *Scanning Tunneling Microscopy and Spectroscopy: Theory, Techniques and Applications* (VCH Publishers Inc., New York, 1993).
- [58] N. Lang, *Phys. Rev. Lett.* **58**, 45 (1987).
- [59] DSP-Scan Release 6.0 Handbook, East Coast Scientific Ltd, 1996.
- [60] The software modifications both of the PC code as well as the DSP assembler code were provided by Th. Jürgens.
- [61] C. Joachim, J. K. Gimzewski, and A. Aviram, *Nature (London)* **408**, 541 (2000).
- [62] A. Aviram and M. A. Ratner, *Chem. Phys. Lett.* **29**, 277 (1974).

- [63] V. J. Langlais, R. R. Schlittler, H. Tang, A. Gourdon, C. Joachim, and J. K. Gimzewski, *Phys. Rev. Lett.* **83**, 2809 (1999).
- [64] M. A. Reed, C. Zhou, C. J. Muller, T. P. Burgin, and J. M. Tour, *Science* **278**, 252 (1997).
- [65] D. Porath, A. Bezryadin, S. de Vries, and C. Dekker, *Nature (London)* **403**, 635 (2000).
- [66] F. Moresco, G. Meyer, K. H. Rieder, H. Tang, A. Gourdon, and C. Joachim, *Phys. Rev. Lett.* **86**, 672 (2001).
- [67] J. Chen, M. A. Reed, A. M. Rawlett, and J. M. Tour, *Science* **286**, 1550 (1999).
- [68] C. Joachim, J. K. Gimzewski, and H. Tang, *Phys. Rev. B* **58**, 16407 (1998).
- [69] S. J. Tans, A. R. M. Verschueren, and C. Dekker, *Nature (London)* **393**, 49 (1998).
- [70] M. Schunack, L. Peterson, A. Kühnle, E. Lægsgaard, I. Steensgaard, I. Johannsen, and F. Besenbacher, *Phys. Rev. Lett.* **86**, 456 (2001).
- [71] M. Böhringer, R. Berndt, and W.-D. Schneider, *Phys. Rev. B* **55**, 1384 (1997).
- [72] T. A. Jung, R. R. Schlittler, J. K. Gimzewski, H. Tang, and C. Joachim, *Science* **271**, 181 (1996).
- [73] J. Kuntze, R. Berndt, P. Jiang, H. Tang, A. Gourdon, and C. Joachim, *Phys. Rev. B* **65**, 233405 (2002).
- [74] O. Sautet, C. Joachim, M. L. Bocquet, and M. Salmeron, *Ann. Chim. (Paris)* **17**, 217 (1992).
- [75] N. L. Allinger, *J. Am. Chem. Soc.* **99**, 8127 (1977).
- [76] Y. Izumi, *Adv. Catal.* **32**, 215 (1983).

- [77] G. P. Lopinski, D. J. Moffatt, D. D. M. Wayner, and R. A. Wolkow, *Nature (London)* **392**, 909 (1998).
- [78] M. Böhringer, K. Morgenstern, W.-D. Schneider, R. Berndt, F. Mauri, A. D. Vita, and R. Car, *Phys. Rev. Lett.* **83**, 324 (1999).
- [79] M. Böhringer, K. Morgenstern, W.-D. Schneider, and R. Berndt, *Angew. Chem. Int. Ed.* **38**, 821 (1999).
- [80] M. Böhringer, W.-D. Schneider, and R. Berndt, *Angew. Chem. Int. Ed.* **39**, 792 (2000).
- [81] A. Kühnle, T. R. Linderoth, B. Hammer, and F. Besenbacher, *Nature (London)* **415**, 891 (2002).
- [82] M. Schunack, E. Lægsgaard, I. Steensgaard, I. Johannsen, and F. Besenbacher, *Angew. Chem. Int. Ed.* **40**, 2623 (2001).
- [83] D. S. Sholl, A. Asthagiri, and T. D. Power, *J. Phys. Chem. B* **105**, 4771 (2001).
- [84] M. O. Lorenzo, C. J. Baddeley, C. Muryn, and R. Raval, *Nature (London)* **404**, 376 (2000).
- [85] J. Kuntze, X. Ge, and R. Berndt, *Nanotechnology* **15**, S337 (2004).
- [86] S. M. Barlow and R. Raval, *Surf. Sci. Rep.* **50**, 201 (2003).
- [87] S. D. Feyter and C. D. Schryver, *Chem. Soc. Rev.* **32**, 139 (2003).
- [88] J. V. Barth, J. Weckesser, C. Cai, P. Günter, L. Bürgi, O. Jeandupeux, and K. Kern, *Angew. Chem. Int. Ed.* **39**, 1230 (2000).
- [89] C. B. France and B. A. Parkinson, *J. Am. Chem. Soc.* **125**, 12712 (2003).
- [90] J. R. Hahn and W. Ho, *Phys. Rev. Lett.* **87**, 196102 (2001).
- [91] R. Otero, F. Hümmelink, F. Sato, S. B. Legoas, P. Thostrup, E. Lægsgaard, I. Stensgaard, D. S. Galvão, and F. Besenbacher, *Nature Mater.* **3**, 779 (2004).



- 
- [92] F. J. Himpsel, J. E. Ortega, G. J. Mankey, and R. F. Willis, *Adv. Phys.* **47**, 511 (1998).
- [93] R. Nötzel and K. H. Ploog, *Adv. Mater.* **5**, 22 (1993).
- [94] R. Nötzel, Z. Niu, M. Ramsteimer, H. P. Schönherr, A. Trampert, L. Däweritz, and K. H. Ploog, *Nature (London)* **392**, 56 (1998).
- [95] P. Segovia, D. Purdie, M. Hagsberger, and Y. Baer, *Nature (London)* **402**, 504 (1999).
- [96] V. Repain, J. M. Berroir, B. Croset, S. Rousset, Y. Garreau, V. H. Etgens, and J. Lecoœur, *Phys. Rev. Lett.* **84**, 5367 (2000).
- [97] J. V. Barth, H. Brune, G. Ertl, and R. J. Behm, *Phys. Rev. B* **42**, 9307 (1990).
- [98] W. Chen, V. Madhavan, T. Jamneala, and M. F. Crommie, *Phys. Rev. Lett.* **80**, 1469 (1998).
- [99] L. Gross, F. Moresco, L. Savio, A. Gourdon, C. Joachim, and K.-H. Rieder, *Phys. Rev. Lett.* **93**, 56103 (2004).
- [100] K. W. Hipps, D. E. Barlow, and U. Mazur, *J. Phys. Chem. B* **104**, 2444 (2000).
- [101] D. E. Barlow and K. W. Hipps, *J. Phys. Chem. B* **104**, 5993 (2000).
- [102] X.-H. Lu, M. Grobis, K. H. Khoo, S. G. Louie, and M. F. Crommie, *Phys. Rev. B* **70**, 115418 (2004).
- [103] C. Joachim, Technical report (unpublished).
- [104] X.-H. Lu, M. Grobis, K. H. Khoo, S. G. Louie, and M. F. Crommie, *Phys. Rev. Lett.* **90**, 096802 (2003).
- [105] J. M. Tour, M. Kozaki, and J. M. Seminario, *J. Am. Chem. Soc.* **120**, 8486 (1998).

- [106] C. P. Collier, E. W. Wong, M. Belohradský, F. M. Raymo, J. F. Stoddart, P. J. Kuekes, R. S. Williams, and J. R. Heath, *Science* **285**, 391 (1999).
- [107] J. M. Tour, *Acc. Chem. Res.* **33**, 791 (2000).
- [108] J. Chen, W. Wang, M. A. Reed, A. M. Rawlett, D. W. Price, and J. M. Tour, *Appl. Phys. Lett.* **77**, 1224 (2000).
- [109] M. A. Reed, J. Chen, A. M. Rawlett, D. W. Price, and J. M. Tour, *Appl. Phys. Lett.* **78**, 3735 (2001).
- [110] F. Jäckel, M. D. Watson, K. Müllen, and J. P. Rabe, *Phys. Rev. Lett* **92**, 188303 (2004).
- [111] X. F. Guo, J. P. Small, J. E. Klare, Y. L. Wang, M. S. Purewal, I. W. Tam, B. H. Hong, R. Caldwell, L. M. Huang, S. O'Brien, J. M. Yan, R. Breslow, S. J. Wind, J. Hone, P. Kim, and C. Nuckolls, *Science* **311**, 356 (2006).
- [112] R. A. Collins and K. A. Mohammed, *J. Phys. D* **21**, 154 (1988).
- [113] C. Hamann, M. Hietschold, A. Mrwa, M. Mueller, M. Starke, and R. Kilper, *Top. Mol. Organ. Eng.* **7**, 129 (1991).
- [114] R. Madru, G. Guillaud, M. Sadoun, M. Maitrot, J. J. Andre, J. Simon, and R. Even, *Chem. Phys. Lett.* **145**, 343 (1988).
- [115] M. Maitrot, G. Guillaud, B. Boudjema, J. J. Andre, H. Strzelecka, J. Simon, and R. Even, *Chem. Phys. Lett.* **133**, 59 (1987).
- [116] H. Kropf and F. Steinbach, *Katalyse an Phthalocyaninen* (Georg Thieme Verlag, Stuttgart, 1973).
- [117] S.-I. Mho, B. Ortiz, S.-M. Park, D. Ingersoll, and N. Doddapaneni, *J. Electrochem. Soc.* **142**, 1436 (1995).
- [118] J. H. Zagal, *Coord. Chem. Rev.* **119**, 89 (1992).

- [119] A. L. Thomas, *Phthalocyanine Research and Applications* (CRC Press, Boca Raton, FL, 1990).
- [120] B. W. Flynn, A. E. Owen, and J. Mayor, *J. Phys. C* **10**, 4051 (1977).
- [121] A. K. Ghosh, D. L. Morel, T. Feng, R. F. Shaw, and J. C. A. Rowe, *J. Appl. Phys.* **45**, 230 (1974).
- [122] A. Rosa and E. J. Baerends, *Inorg. Chem.* **31**, 4717 (1992).
- [123] A. Rosa and E. J. Baerends, *Inorg. Chem.* **33**, 584 (1994).
- [124] M.-S. Liao and S. Scheiner, *J. Chem. Phys.* **114**, 9780 (2001).
- [125] P. A. Reynolds and B. N. Figgis, *Inorg. Chem.* **30**, 2294 (1991).
- [126] S. Carniato, G. Dufour, F. Rochet, H. Roulet, P. Chaquin, and C. Giessner-Prettre, *J. Electron Spectrosc. Relat. Phenom.* **67**, 189 (1994).
- [127] J. K. Gimzewski, E. Stoll, and R. R. Schlittler, *Surf. Sci* **181**, 267 (1987).
- [128] R. Moeller, R. Coenen, A. Esrlinger, and B. Kaslouski, *J. Vac. Sci. Technol. A* **8**, 659 (1990).
- [129] C. Ludwig, R. Strohmaier, J. Petersen, B. Gompf, and W. Eisenmenger, *J. Vac. Sci. Technol. B* **12**, 1963 (1994).
- [130] T. Fritz, M. Hara, W. Knoll, and H. Sasabe, *Mol. Cryst. Liq. Cryst. Sci. Technol. Sect. A* **252**, 561 (1994).
- [131] V. Petracek, *Int. J. Electron.* **78**, 267 (1995).
- [132] M. Kanai, T. Kawai, K. Motai, X. D. Wang, T. Hashizume, and T. Sakura, *Surf. Sci* **329**, L619 (1995).
- [133] G. V. Nazin, X. H. Qiu, and W. Ho, *Science* **302**, 77 (2003).
- [134] J. Freund, O. Probst, S. Grafstroem, S. Dey, J. Kowalski, R. Neumann, M. Woetge, and zu G. Putlitz, *J. Vac. Sci. Technol. B* **12**, 1914 (1994).

- [135] O. Pester, A. Mrwa, and M. Hietschold, *Phys. Status Solidi A* **131**, 19 (1992).
- [136] C. Hamann, R. Laiho, and A. Mrwa, *Phys. Status Solidi A* **116**, 729 (1989).
- [137] T. G. Gopakumar, M. Lackinger, M. Hackert, F. Muller, and M. Hietschold, *J. Phys. Chem. B* **108**, 7839 (2004).
- [138] S. Berner, M. de Wild, L. Ramoino, S. Ivan, A. Baratoff, H.-J. Güntherodt, H. Suzuki, D. Schlettwein, and T. A. Jung, *Phys. Rev. B* **68**, 115410 (2003).
- [139] X. Qiu, C. Wang, S. Yin, Q. Zeng, B. Xu, and C. Bai, *J. Phys. Chem. B* **104**, 3570 (2000).
- [140] M. Stöhr, T. Wagner, M. Gabriel, B. Weyers, and R. Möller, *Phys. Rev. B* **65**, 033404 (2001).
- [141] M. Fendrich, T. Wagner, M. Stöhr, and R. Möller, *Phys. Rev. B* **73**, 115433 (2006).
- [142] K. W. Hipps, X. Lu, X. D. Wang, and U. Mazur, *J. Phys. Chem.* **100**, 11207 (1996).
- [143] X. Lu, K. W. Hipps, X. D. Wang, and U. Mazur, *J. Am. Chem. Soc* **118**, 7197 (1996).
- [144] A. Zhao, Q. Li, L. Chen, H. Xiang, W. Wang, S. Pan, B. Wang, X. Xiao, J. Yang, J. G. Hou, and Q. Zhu, *Science* **309**, 1542 (2005).
- [145] M. Takada and H. Tada, *Chem. Phys. Lett.* **392**, 265 (2004).
- [146] M. Takada and H. Tada, *Ultramicroscopy* **105**, 22 (2005).
- [147] M. Takada and H. Tada, *Jpn. J. Appl. Phys.* **44**, 5332 (2005).
- [148] [www.aldrich.com](http://www.aldrich.com).
- [149] T. Yokoyama, S. Yokoyama, T. Kamikado, Y. Okuno, and S. Mashiko, *Nature (London)* **413**, 619 (2001).

- [150] A. Dmitriev, H. Spillmann, N. Lin, J. V. Barth, and K. Kern, *Angew. Chem. Int. Ed.* **42**, 2670 (2003).
- [151] D. L. Keeling, N. S. Oxtoby, C. Wilson, M. J. Humphry, N. R. Champness, and P. H. Beton, *Nano Lett.* **3**, 9 (2003).
- [152] J. A. Theobald, N. S. Oxtoby, M. A. Phillips, N. R. Champness, and P. H. Beton, *Nature* **424**, 1029 (2003).
- [153] A. K. Boal, F. Ilhan, J. E. DeRouchey, T. Thurn-Albrecht, T. P. Russell, and V. M. Rotello, *Nature (London)* **404**, 746 (2000).
- [154] O. Marchenko and J. Cousty, *Phys. Rev. Lett.* **84**, 5363 (2000).
- [155] M. Furukawa, H. Tanaka, K. Sugiura, Y. Sakata, and T. Kawai, *Surf. Sci.* **445**, L58 (2000).
- [156] M. S. E. Lægsgaard, I. Stensgaard, and F. Besenbacher, *J. Chem. Phys.* **117**, 8493 (2002).
- [157] M. Ashida, N. Uyeda, and E. Suito, *Bull. Chem. Soc. Jpn.* **39**, 2616 (1966).
- [158] A. Hoshimo, Y. Takenaka, and H. Miyaji, *Acta Cryst. B* **59**, 393 (2003).
- [159] B. N. Diel, T. Inabe, J. W. Lyding, K. F. Schoch, J. C. R. Kannewurf, and T. J. Marks, *J. Am. Chem. Soc.* **105**, 1551 (1983).
- [160] M. J. Frisch and *et al.*, *GAUSSIAN03, Revision B.05* (Gaussian, Inc., Pittsburgh, PA, 2003).
- [161] C. Chavy, C. Joachim, and A. Altibelli, *Chem. Phys. Lett.* **214**, 569 (1993).
- [162] J. Lagoute, K. Kanisawa, and S. Fölsch, *Phys. Rev. B* **70**, 245415 (2004).
- [163] H. Bertagnolli, A. Weber, W. Hörner, T. S. Ertel, U. Reinöhl, M. Hanack, M. Hees, and R. Polley, *Inorg. Chem.* **36**, 6397 (1997).

- [164] A. Weber, T. S. Ertel, U. Reinöhl, H. Bertagnolli, M. Leuze, M. Hees, and M. Hanack, *Eur. J. Inorg. Chem.* **2000**, 2289 (2000).
- [165] R. Caminiti, M. P. Donzello, C. Ercolani, and C. Sadun, *Inorg. Chem.* **37**, 4210 (1998).
- [166] M. Gorsch and H. Homborg, *Z. Anorg. Allg. Chem.* **624**, 634 (1998).
- [167] H. Hückstädt, C. Bruhn, and H. Homborg, *J. Porphyrins Phthalocyanines* **1**, 367 (1997).
- [168] M. J. Chen and J. W. Rathke, *Organometallics* **13**, 4875 (1994).
- [169] H. Hückstädt and H. Homborg, *Z. Anorg. Allg. Chem.* **623**, 369 (1997).
- [170] M. Göldner, H. Hückstädt, K. S. Murray, B. Moubaraki, and H. Homborg, *Z. Anorg. Allg. Chem.* **624**, 288 (1998).
- [171] Y. Chen, M. Barthel, M. Seiler, L. R. Subramanian, H. Bertagnolli, and M. Hanack, *Angew. Chem.* **114**, 3373 (2002).
- [172] U. Mazur and K. W. Hipps, *J. Chem. Phys.* **99**, 6684 (1995).
- [173] U. Mazur and K. W. Hipps, *J. Phys. Chem. B* **103**, 9721 (1999).
- [174] M. Rocco, K.-H. Frank, P. Yannoulis, and E.-E. Koch, *J. Chem. Phys.* **93**, 6859 (1990).

# Acknowledgments

It is with deepest gratitude and appreciation that I complete the requirements for the degree of doctor of science in physics at University Kiel. I am especially grateful to my advisor Prof. Richard Berndt for giving me the opportunity of working in his group, for providing me the resources necessary to learn and grow as a scientist, and for his serious, honest and critical attitude being a model to my academic life.

I would like to express my gratitude to Dr. Jens Kuntze for guiding and training me into STM. Thank for your help when I was just arriving in Kiel without knowing anything, this really meant a lot to me. I am lucky enough to learn many experimental and instrumental details from Dr. Laurent Limot (now at IPCMS, France).

I wish to thank Dr. Carlos Manzano (now at IMRE, Singapore). We shared good time and bad time on STM measuring, leakage detecting, chamber polishing and so on. I am fortunate in knowing and working with you.

Thanks to Dr. Bridget Murphy, Dr. Thomas Jürgens, Michael Becker, and Dr. Nicolas Neél for checking my dissertation manuscript. Thanks to Dr. Yongfeng Wang for the discussion of CoPc.

I am very glad to have worked with all the colleagues of our groups: Dr. Jörg Kröger, Dr. Thomas van Hofe, Wang Hongna, Patrick Schmidt, Henning Jensen, Jianwei Zhang, Manfred Stiller, Martin Ziegler, Seven Marten Czerwonka, Jörg Neubauer, Heinz-Georg Börst, Dr. Jürgen Rathlev, Frau Ursula Goetzke. Thanks for all of you in helping me in my research and life in Kiel.

To Juan, my wife, for your support, patience and courage along all the years together with me.

And finally, respects and thanks to my parents, without your encourage and

education during my whole life, everything would be impossible.



# Curriculum Vitae

Name: Xin Ge  
Date of birth: February 26, 1977  
Place of birth: Yangzhou, Jiangsu Province, P. R. China  
Nationality: Chinese  
Marital status: married, no child

## Education:

09/2002 - present Institut für Experimentelle und Angewandte Physik der  
Universität Kiel  
Research assistant in the group of Prof. Dr. Richard  
Berndt.  
PhD thesis: “Scanning Tunneling Microscopy of One-  
dimensional Molecular Self-assembly on Metal Sur-  
faces”.

09/1999 - 06/2002 Faculty of Electronic Engineering, Tsinghua University,  
Beijing, P. R. China  
Master of Engineering degree in Physical Electronics.  
Thesis title: “Secondary Ion Mass Spectroscopy Depth  
Profiling of  $\text{Si}_x\text{Ge}_{1-x}$  and Silicon-On-Insulator (SOI)”.

09/1995 - 07/1999 Faculty of Electronic Engineering, Tsinghua University,  
Beijing, P. R. China  
Bachelor of Engineering degree in Physical Electronics  
and Optoelectronics.

Thesis title: "Secondary Ion Mass Spectroscopy Investigation on SiGe".

09/1992 - 07/1995 Yangzhou Senior High School, Yangzhou, P. R. China

09/1989 - 07/1992 Yangzhou First Junior High School, Yangzhou, P. R. China

09/1983 - 07/1989 Dongguan Centra Primary School, Yangzhou, P. R. China

**List of Publications:**

J. Kuntze, X. Ge, and R. Berndt, *Chiral structures of lander molecules on Cu(100)*, Nanotechnology **15**, S337 (2004)